Electrospark Deposited Interlayer and its Influence on Dissimilar Resistance Welding of DP600 to AA5052

by

Caiyin Li

A thesis

presented to the University of Waterloo

in fulfilment of the

thesis requirement for the degree of

Master of Applied Science

in

Mechanical and Mechatronics Engineering

Waterloo, Ontario, Canada, 2021

Author's Declaration

This thesis consists of materials all of which I authored or co-authored: See Statement of Contributions included in the thesis.

This is a true copy of the thesis, including any required final revisions, as accepted by my examiners.

I understand that my thesis may be made electronically available to the public.

Statement of contributions

This thesis was solely written by the candidate. Professors N. Zhou and A. P. Gerlich contributed to editing the entire thesis. Additional contributions were made by other members of the Centre for Advanced Material Joining group from University of Waterloo and Centre for Automotive Materials especially Pablo Enrique. The specific contributions are listed below.

Chapter 4 of this thesis is based on the results from a published manuscript: “Electrospark deposition interlayers for dissimilar resistance welding of steel to aluminum”. The experimental design, analysis, and writing were conducted by leading author Pablo Enrique and the candidate. The paper was also co-authored by N. Zhou, A. P. Gerlich and Mr. C. Digiovanni who contributed through technical discussions of the results and assisted with editing the manuscript.

Chapter 5 of this thesis is based on the results from a published manuscript: “Influence of Interlayer Characteristics on Dissimilar Resistance Welding of Aluminum to Steel”. The experimental design, analysis, and writing were conducted by the candidate. The paper was also co-authored by Pablo Enrique, Ningyue Mao, Nigel Scotchmer, Adrian Gerlich, and Norman Zhou, who contributed through technical discussions of the results and assisted with editing the manuscript.

Abstract

Challenges associated with the resistance spot welding of aluminum and steel must be addressed to enable wider use of low-density aluminum alloys in commercial vehicles. These challenges include the significant difference in melting point and thermal conductivity between aluminum alloys and steels – which results in a brazed joint rather than the formation of a weld nugget – and the formation of thick brittle iron aluminide intermetallic when molten aluminum is in contact with steel. This study demonstrates the use of electrospark deposited interlayers to limit the contact between molten aluminum and steel during resistance spot welding. Magnesium, aluminum, and nickel-based interlayers are studied to determine material characteristics suitable for the resistance spot welding of galvanized dual phase steel (DP600) to AA5052. Tensile lap-shear strength increases of up to 84% over the non-interlayer configuration are obtained using an optimized interlayer and resistance spot welding process, achieving 6 mm diameter joints capable of withstanding 8 kN of shear loading. This has the potential to facilitate the adoption of aluminum in the automotive industry as light weighting becomes a more critical issue.

Acknowledgements

I like to give my special thanks to my supervisors Prof. Norman Zhou and Prof. Adrian Gerlich for their time, guidance, and support throughout my master's study. Their guidance helps me not only academically, but also helps me to see the world from a new perspective.

I also wish to thank sponsors and collaborators including Nigel Scotchmer from Huy's Industries, for his support, knowledge, and generosity in providing the necessary material and to complete this thesis.

In addition, I wish to acknowledge the assistance of my fellow CAMJ members, especially Pablo Enrique. The time we spend inside and outside the lab has made this experience memorable.

Finally, I wish to thank my family for their support, without which I would not be able to complete this degree.

Table of Contents

List of Figures ix

List of Tables xi

List of Equations xii

List of Abbreviations xiii

List of Symbols xiv

Chapter 1 Introduction 1

- 1.1 Research Motivation 1
- 1.2 Research Objective 1
- 1.3 Thesis Outline 2

Chapter 2 Literature Review 3

- 2.1 Electrospark Deposition (ESD) 3
  - 2.1.1 Background Information of ESD 3
  - 2.1.2 ESD Equipment and Processing Principal 5
  - 2.1.3 Important Factors to be Considered during ESD 7
- 2.2 Resistance Spot Welding (RSW) 10
  - 2.2.1 Background Information about RSW 10
  - 2.2.2 RSW Equipment and Processing Principal 11
  - 2.2.3 Important Parameters of RSW 15
- 2.3 Dissimilar Welding of Al to Steel 17
  - 2.3.1 Al Alloys and Steel 17
  - 2.3.2 Metallurgical Reactions During Welding Process 18
  - 2.3.3 Significant Factors Related to Mechanical Properties 21
  - 2.3.4 Different Approaches to Improve the Joint Properties (Welding Quality) 25
- 2.4 Interlayer Application in Dissimilar RSW (of Al to Steel) 30
  - 2.4.1 Background Information about Interlayer 30
  - 2.4.2 Interlayer Application Examples 31
  - 2.4.3 Interlayer Selection 35

Chapter 3 Materials and Experimental Methods 37

- 3.1 Material Selection 37
- 3.2 Experimental Equipment 38
  - 3.2.1. ESD machine 38
  - 3.2.2. RSW machine 39

3.3 Metallographic Characterization 40
  3.3.1. Sample Preparation 40
  3.3.2. Optical Imaging 41
  3.3.3. Electron Imaging and Elemental Analysis 41
3.4 Mechanical Testing 42
  3.4.1. Tensile Lap Shear Test 42
  3.4.2. Destructive Peel Test 43
  3.4.3. Microhardness 44
3.5 Experimental Methods and RSW Simulation 45
Chapter 4 ESD Interlayer 51
4.1 Interlayer Material Selection 51
4.2 Effect of ESD Operating Parameters on Different Properties of ESD Coating 53
  4.2.1 Interlayer Deposition Rate 54
  4.2.2 Interlayer Quality and Operating Parameter Selection 57
4.3 Pre-examination of IMC formation during ESD Process 60
4.4 Summary 62
Chapter 5 Effect of Different Interlayer Materials on the Performance of Dissimilar RSW of Al to Steel 63
5.1 Experiments with Al Interlayer 63
  5.1.1 Mechanical Testing 63
  5.1.2 Microstructural Analysis 64
5.2 Experiments with Ni Interlayer 71
  5.2.1 Mechanical Testing 71
  5.2.2 Microstructural Analysis 72
5.3 Experiments with Mg Interlayer 73
  5.3.1 Mechanical Testing 73
  5.3.2 Microstructural Analysis 74
  5.3.3 Welding Current Effect 76
5.4 Shielding Gas 78
5.5 Interlayer Thickness 81
5.6 Summary 82
Chapter 6 Conclusions and Recommendations 84
6.1. Conclusions 84

6.2. Recommendations 85
Reference 87
Appendix. MatLab Simulation of RSW Process Using Different Interlayer Materials 96

List of Figures

Figure 1 Important Components of ESD Equipment........6
Figure 2 Process Ilustration of ESD........6
Figure 3 Relationship between Deposition Surface Roughness and Other Important Parameters........9
Figure 4 a) base pulses and b) triangular pulses of ESD Process........10
Figure 5 Schematics of a AC RSW Equipment........12
Figure 6 Cross-sectional View of a Typical Electrode........12
Figure 7 Important Components of a DC RSW Machine........13
Figure 8 Process Illustration of RSW........14
Figure 9 Microstructural Zone of RSW Assembly........15
Figure 10 Different Significant Stages of RSW Process........17
Figure 11 SLC Project Design Graph........18
Figure 12 Phase Diagram between Fe and Al........19
Figure 13 Intermetallics Formation during RSW of Al to Fe........20
Figure 14 Significant Properties of RSW Assembly........21
Figure 15 Failure Location of a) BM and b) IMC........22
Figure 16 Effect of Expulsion on Weld Nugget Size........24
Figure 17 Hardness Profile through Welds........25
Figure 18 Microstructural Structure in Fusion Zone........25
Figure 19 Elemental Distribution of Weld of Al to Steel........28
Figure 20 Microstructure of Weld of Al to Steel........29
Figure 21 Phase Diagram of Al and Zn........30
Figure 22 Illustration of insert AlMg Film........32
Figure 23 Fusion Zone Formation During RSW........32
Figure 24 a) image (SEM) at interface near centre of nugget; b) EPMA line analysis along line in a)........32
Figure 25 Preparation and Insertion Method of Graphene Interlayer........33
Figure 26 Mechanical Performance of Samples Welded with and without Graphene Interlayer under Different Parameters........34
Figure 27 Microstructure Observed along the Interface of Sample Welded a)without interlayer; and b)with interlayer........34
Figure 28 Schematics of ESD Equipment........39
Figure 29 Illustration of RSW Equipment used in Thesis........40
Figure 30 Optical Microscope........41
Figure 31 Scanning Electron Microscopy........42
Figure 32 Tensile Testing Machine........43
Figure 33 Peel Testing Station........44
Figure 34 Microhardness Tester........44
Figure 35 Graphical Demonstration of Weld Assembly........46
Figure 36 Simulated Temperature Profile for Different Interlayer Materials........49
Figure 37 Simulated 2D Temperature Heat Map of Different Interlayer Materials........50
Figure 38 Welded Faying Interface of AA5052 to DP600 with interlayer of a)AA4043; b)IN725........52
Figure 39 Samples welded with IN725 at a)faying interface and elemental illustration of b)Al, c)Fe, and d)Ni........52
Figure 40 Deposition Rate of AA4043 Interlayer........54

Figure 41 Deposition Rate of AZ81A 55
Figure 42 Deposition Rate of IN625 56
Figure 43 Deposition Rate of Ni99 57
Figure 44 AA4043 deposition at 310 µF, 140 V, 150 Hz 58
Figure 45 AZ81A deposition at a)200 µF, 80 V, 150 Hz, and b)250 µF, 80 V, 150 Hz 59
Figure 46 IN625 Deposition Quality at a)100 µF, 100V, 150 Hz; and b) 140 µF, 120V, 150 Hz 60
Figure 47 Interface between AA4043 interlayer and DP600 before welding 61
Figure 48 Interface observation before RSW between DP600 and a)AZ81A, and b)IN625 62
Figure 49 Comparison between the mechanical strength of samples welded with AA4043 interlayer and without interlayer 64
Figure 50 SEM images of a) AA5052 welded to AA4043 coated GI DP600 at 15 kA b) ESD of AA4043 on GI DP600 before RSW and c) AA5052 welded to GI DP600 without an interlayer at 15 kA. Results of the EDX linescan as indicated in each image are shown adjacent to the image. 66
Figure 51 IMC formation near the center of weld for samples welded a)with AA4043 and b) without AA4043 67
Figure 52 Samples welded without interlayer 68
Figure 53 Elemental scanning at the edge of sample welded without interlayer 69
Figure 54 Dong et al observation in gas porosity 69
Figure 55 Comparison between the mechanical strength of samples welded with no interlayer no Zn coating, with AA4043 interlayer, and without interlayer 71
Figure 56 Comparison between the mechanical strength of samples welded with IN625 interlayer and without interlayer 72
Figure 57 Fracture Location for Samples Welded with IN625 73
Figure 58 Comparison between the mechanical strength of samples welded with AZ81A interlayer and without interlayer 74
Figure 59 a) Weld created with an AZ81A interlayer and b) linescan corresponding to the dotted arrow included in a). 75
Figure 60 Failure location for AZ81A interlayer samples after spot welding and tensile lap shear testing 76
Figure 61 Microstructure of AZ81A coated sample at (a) 13 kA, (b) 14 kA, and (c) annotated at 10x magnification at 14 kA 77
Figure 62 Peel test nugget sizes for samples welded with AZ81A interlayer at a) 13 kA, b) 14 kA 77
Figure 63 Mix of HAZ failure and pull-out failure in sample with AZ81A welded at 17 kA 78
Figure 64 a) Schematic illustration of ESD done in sealed environment, b)assembly of sealed ESD process environment 79
Figure 65 Comparison of mechanical performance for samples welded with interlayer made a) with shielding gas; b) without shielding gas 80
Figure 66 Microstructure of AZ81A coated sample at (a) 13 kA, (b) 14 kA without shielding gas 81
Figure 67 Comparison of tensile shear strength for samples welded with AZ81A interlayer under different deposition time 82

List of Tables

Table 1 Chemical Composition of Base Metals[52,53] 37
Table 2 Mechanical Properties of Base Metals 37
Table 3 Thermal and Electrical Properties of Base Metals[54,55] 37
Table 4 Chemical Composition of Interlayer Materials [56] 38
Table 5 Thermal and Electrical Properties of Interlayer Materials 38
Table 6 Thermal and Chemical Properties of Copper Electrodes 40
Table 7 RSW Operating Parameters 45
Table 8 Hardness Values of Materials used in Experiments 48

List of Equations

Equation 1: ESD Spark Energy 7
Equation 2: Shear Modulus 36
Equation 3: Bulk Modulus 36
Equation 1: Change in Temperature 46
Equation 2: Heat generation 46
Equation 3: Bulk resistance 47
Equation 4: Contact resistance 47
Equation 5: Dirichlet boundary condition 47
Equation 6: Neumann boundary conditions 48
Equation 7: Capacitor energy 57

List of Abbreviations

AC	Alternating Current
BM	Base Metal
DC	Direct Current
DP	Dual Phase
EDX	Energy dispersive x-ray spectroscopy
ESD	Electrospark Deposition
FSSW	Friction Stir Spot Welding
FZ	Fusion Zone
GI	Galvanized
HAZ	Heat Affected Zone
HEA	High Entropy Alloy
HVOF	High Velocity Oxygen Fuel
IGBT	Insulated Gate Bipolar Transistor
MIG	Metal Inert Gas
OM	Optical Microscope
PVA	Polyvinyl Alcohol
RSW	Resistance Spot Welding
SEM	Scanning Electron Microscope
SLC	SuperLIGHT – CAR
TIG	Tungsten Inert Gas

List of Symbols

α	thermal diffusivity
g	volumetric rate of heat generation
k	thermal conductivity
I	current running through the assembly
R	resistance
V	volume of assembly
ρ	electrical resistivity
Δx	distance along the current path
A	cross-sectional area
H	Brinell hardness
F	applied force
ξ	pressure factor
η	contact spots factor
G	shear modulus
B	bulk modulus
$C11, C12, C44$	elastic constants for cubic system

Chapter 1 Introduction

1.1 Research Motivation

A gradual transition is being made in conventional automotive manufacturing, as the production of light-weight vehicles has become a common goal. Reducing the body weight not only lowers the bulk material costs per mass, but also improves energy efficiency, enhances performance, and reduces CO_2 emissions. In this case, many light-weight materials such as aluminum, magnesium, and metal-matrix composite castings are being proposed to substitute for ferrous components in powertrain and chassis applications[1] Among these materials, aluminum has been most widely applied in current vehicle design due to its high stiffness-to-weight ratio, great corrosion resistance, and low cost to weight ratio. Resistance spot welding of light-weight aluminum alloys to high strength steels is the most desirable technique for joining these two alloys, however, this is hampered by the formation of Al_5Fe_2 and $Al_{13}Fe_4$ intermetallic compounds (IMC). This is inevitable when these metals are melted together under any condition and leads to brittleness which makes the dissimilar weld joint much less reliable than their steel-steel counterparts[2]. Managing the formation and thickness of IMC layers has become the key to optimizing welding quality, avoiding cracking, and improving strength.

1.2 Research Objective

This thesis will focus on investigating the optimized ESD parameters for different interlayer materials, and then apply them as a method to improve the quality of RSW joints combining AA5052 and DP600 sheet material.

1.3 Thesis Outline

This thesis has been organized into seven chapters, which are detailed in the following paragraphs.

Chapter 1 introduces the motivation, objective, and layout of the thesis.

Chapter 2 provides a summary of published literature on the field of ESD, RSW, dissimilar welding of Al alloy to steel, and the interlayer application. It also demonstrates gaps in the literature that the thesis work is intended to fill.

Chapter 3 describes the material selection, experimental equipment, metallographic characterization, mechanical testing, experimental methods, and process simulation used in this thesis.

Chapter 4 explains the interlayer material selection made in the experiments and illustrates the effect of ESD operating parameters and presence of inert gas on deposited interlayer properties, and finally makes selection on the ESD operating parameters.

Chapter 5 shows how the application of Al, Ni, and Mg interlayer changes the mechanical performance and microstructure of the weld assembly. It also includes the discussion on the possibility of eliminating shielding gas usage in improving the mechanical strength of weld samples.

Chapter 6 summarizes the main findings in this work and also proposes some recommendations for future study.

Chapter 2 Literature Review

2.1 Electrospark Deposition (ESD)

ESD is the primary technique used in this study to deposit interlayer coatings, understanding its processing principal, important components and how those could be affected by the operating parameters can provide a strong support in future interlayer selection and the improvement of interlayer quality.

2.1.1 Background Information of ESD

In the early 19th century, electroplating was first discovered by Luigi Brugnatelliwho discovered that when submerging metallic objects into a solution of dissolved gold, with a charge applied, there is a layer of gold covering the objects[3]. However, his findings did not raise much attention at that time, over a few decades later this technique started to be applied in creating jewelry, and the massive commercial application of chromium plate was not developed until the early 20th century by George J. Sargent. By the mid-1920s, chrome plating has gradually become one of the most popular surface treatment process in industries and military to provide wear and corrosion protection as well as improve appearance and durability. However, except for the significance in coating deposition, it also possesses unavoidable contributions to hazardous, carcinogenic waste generation and pollution control costs, which promotes the discovery of its alternatives[4]. The High Velocity Oxygen Fuel (HVOF) process is one of the alternatives developed in 1980s, it injects powder to high velocity gas stream produced by ignition of fluid fuel and oxygen, then directs the gas stream towards substrate and forms coating with the partially melted powder, the dense coating will have few porosity and high bond strength, resulting in good corrosion resistance[5]. Even though HVOF significantly reduces hazardous substances emission, its application can still be restrained due to its complex dependence upon numerous processing variables and its geometry constraints. Some other alternatives including magnetron sputtering, physical vapor deposition, chemical vapor deposition, and other variants have also been proposed. However, the bond formed between the coating material and substrate for those above-mentioned technologies is either a chemical or a mechanical bond, which are not reliable enough. In late 20th century and early 21st century, a novel coating technology has been developed to produce the most robust and damage-resistant coatings, whose coating quality is very compromising with very few coating failure and also creates a true metallurgical bond between the material and substrate, this process is named ESD.

ESD is a consumable electrode, microwelding process, and is often known as spark hardening, electrospark toughening, electrospark alloying, pulsed fusion surfacing and pulsed electrode surfacing[6]. It deposits material in molten "sparks" as electrical current is passed between the electrode and the substrate's surface and is able to form consistent and thin layer coatings under desirable operating parameters[7]. Limited special surface preparation requirement and offers good compatibility with various material types including metals, alloys, or cermet, which make ESD a popular technique in automotive and aerospace industry for the purpose of surface modification for hardness, wear resistance, corrosion resistance. Besides the purpose of producing coatings, ESD is also beneficial for the application of repair of worn, corroded, or defective components especially for those repairing materials with poor heat affected zone properties (e,g, liquation cracking, high hardness, low toughness), which makes them hard to repair under traditional fusion welding processes such as arc, laser and resistance welding. This process is also very environmentally friendly because to it barely generates emission of hazardous fume, wastes or effluents. In the following section, the ESD equipment and the processing principal of ESD process will be explained in detail.

2.1.2 ESD Equipment and Processing Principal

ESD equipment consists of a capacitor-based power supply and a rotating wire consumable electrode, as shown in Figure 1, to produce short duration high current pulses and welds the material to a substrate often without causing a significant heat affected zone (HAZ)[8]. The electrical energy generated by pulse power supply is stored in the capacitor and when the electrode is moved away from the surface, the energy then gets released in the form of high-frequency plasma arc which ionizes the air and forms a channel between the tip of the electrode (anode) and the substrate workpiece (cathode) as shown in Figure 2[9]. This release of energy also elevates the temperature and pressure of the substrate surface, which melts the material of electrode and penetrates the work-piece surface thus forming the metallurgical bond. Even though the temperature of plasma arc can reach as high as 8000 to 25000 ºC, the short duration of the process can keep the substrate near ambient temperature and thus imparts little or no modification to the base metal's microstructure, and avoids formation of distortion and residual stress due to the low thermal energy applied.

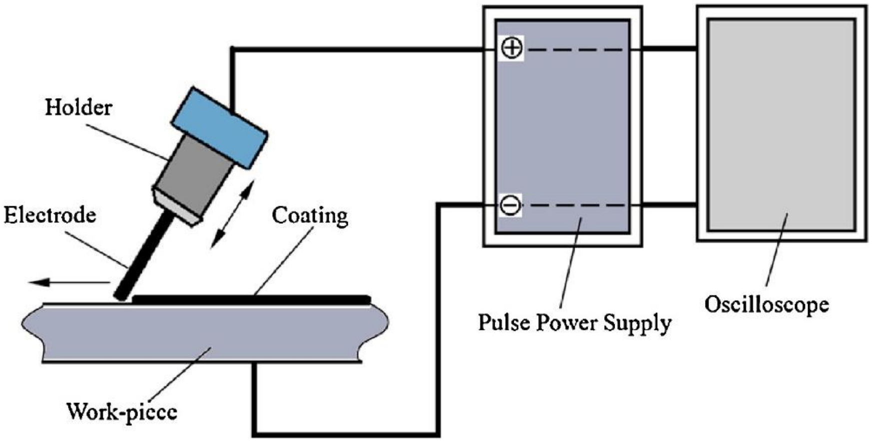

Figure 1 Important Components of ESD Equipment[8]

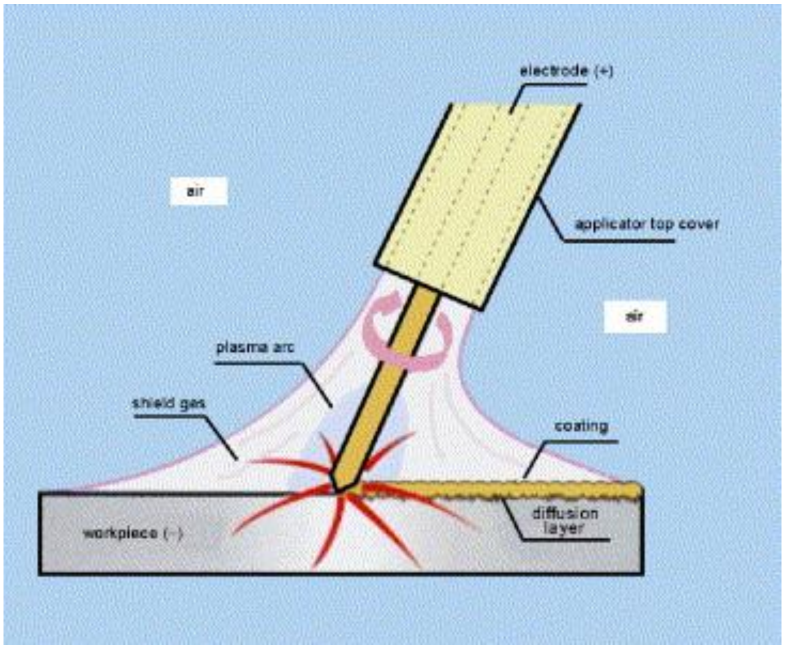

Figure 2 Process Ilustration of ESD[10]

In the following section, some important factors to be considered during ESD process will be discussed in detail. The low net heat input and high cooling rate often results in the formation of nanostructured or amorphous structured deposition, which gives great wear and corrosion resistance.

2.1.3 Important Factors to be Considered during ESD

To ensure high quality deposition, there are some important factors to be considered through the whole ESD process, including electrode movement, spark energy level, selection of materials, and roughness of deposition. Even though ESD can be viewed as a “micro-welding” process, considering it shares many common effects of welding parameters as more traditional arc-welding processes, it also has many unique properties. For example, during the ESD process, the electrode must be constantly in contact with the substrate with a light applied pressure. This continual contact is combined with different electrode motions, including vibratory, oscillatory, and rotary motion. If this motion cannot be sustained, then due to the rapid quenching nature of the ESD process, the electrode will stick to the substrate surface[11].

Another significant factor is the level of spark energy, which primarily governs the quality and deposition rate of the ESD process. The spark energy value is mainly controlled by parameters like capacitance, charging voltage, inductance, and resistivity of the circuit which is ultimately defined by **Equation 1**:

Equation 1: ESD Spark Energy

$$Ep = \int_{0}^{tp} V(t) \cdot I(t) dt$$

in which V represents the discharge voltage, I represents the discharge current, and t_p is the pulse duration[12]. Both capacitance and charging voltage have directly proportional relationship with the spark energy, with a increase in capacitance, the discharge duration under a given potential will also increase; and the larger the charging voltage is, the more amount of current will flow into the capacitor. Unlike those parameters, resistivity of the circuit, on the other hand, has an inverse influence on spark energy because it limits the current flow. This resistivity mainly comes from the power cable, and normally is decided at the stage of equipment manufacturing.

The other major factor is the selection of materials, and similar to arc welding, a wide range of materials such as hard alloys, carbides, borides, intermetallic and cermets can be used in ESD process. In contrast, a superior feature of ESD is that the higher solidification speed of deposits on the substrate facilitate bonding of materials that are not compatible during arc welding. However, ESD process also has application limitations for some materials, for example graphite, which can be used as ESD electrode, but due to the fact that ESD process operates under atmospheric pressure, and graphite cannot be melted in this condition, thus no materials could be transferred[13].

Even though the increase in spark energy can result in higher deposition rate, Wang et al.[14] have illustrated that the surface roughness and the possibility of defect appearance will also increase as shown in Figure 3, Ribalko et al.[15] further proved that this is due to the small scale and localized accumulation of deposits.

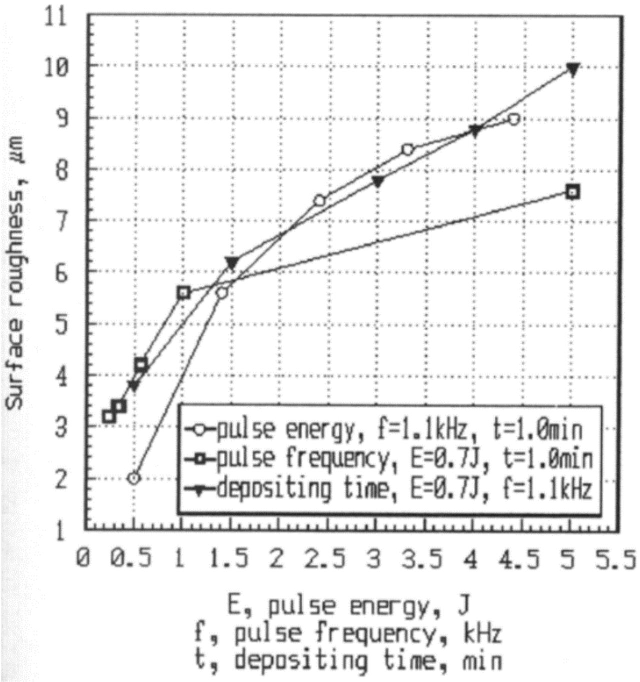

Figure 3 Relationship between Deposition Surface Roughness and Other Important Parameters

One method to solve the roughness issue was proposed by Fassler et al., in which the base deposition pulses and the triangular grinding pulses as shown in Figure 4, such that the base pulse is used to power the process and start the deposition of electrodes onto substrate. innovative triangular grinding pulses were used to grind the materials and thus reducing the roughness[16].

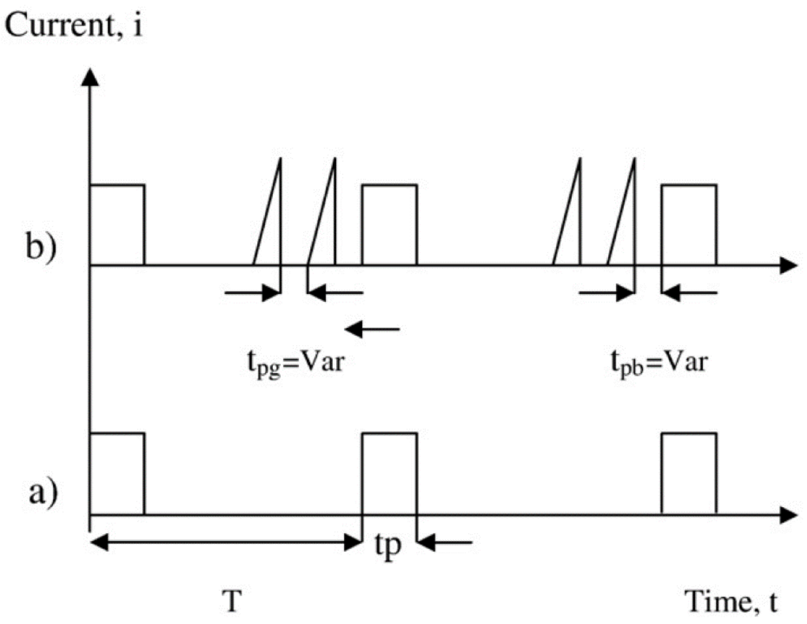

Figure 4 a) base pulses and b) triangular pulses of ESD Process

2.2 Resistance Spot Welding (RSW)

RSW is the primary technology used in this study to weld samples, understanding its processing principal, important components and how those could be affected by the operating parameters can provide a strong support in future weld quality optimization.

2.2.1 Background Information about RSW

The history of welding technologies could be traced back all the way to 1000 B.C., starting along with the discovery and shaping of metals, where the first welded pieces were gold ornaments[17]. The development of welding technology did not progress much until the Industrial Revolution in the 1700’s to 1800’s, and its widespread application was accelerated by the military need in World War I and II. Prior to the discovery of RSW, arc welding was first developed, and in 1885, Elihu Thompson accidentally fused two copper wires together and eventually came up with the idea of electric resistance welding[18].

RSW, also known as spot welding, is a welding process that uses the heat generated from the resistance to an electric current along with pressure applied by copper alloy electrodes with desirable geometry to weld two or more metal sheets together. Not long after the development of RSW, it has been widely used in many different industries, such as automotive, aerospace, medical equipment, and electronics[19]. Unfortunately, RSW is not an ideal welding method for all material types, it still has limitations in application, for which materials in the form of sheet metal and wire mesh are more easily to be welded by RSW than thicker (>6 mm) metals because heat will disperse into the surrounding instead of focusing onto the contact weld spot[20]. Also, RSW may cause distortion and produce defects including internal cracking and surface cracks in material, thus reduce the fatigue strength and deteriorate the corrosion resistance of the joint. In the following section, the RSW equipment and the processing principal of ESD process will be explained in detail.

2.2.2 RSW Equipment and Processing Principal

In the modern-day manufacturing industry, RSW machines are widely used. There are mainly two types of RSW equipment based on different power supply, which are conventional AC RSW machine and an inverter-based DC RSW machine. Some important components of an AC RSW machine are shown in Figure 5, which shows an air cylinder used to adjust the applied electrode force, and copper alloy electrodes that are often used due to its high thermal conductivity, high hardness, and good durability[21]. Controllable cooling water also flows through the special designed geometry of electrode as shown in Figure 6 to ensure good dispute of excessive heat[22]. A digital control system is often used to centrally control the welding parameters, and a foot pedal is used to ergonomically initiate the welding process. The performance of welding is closely related to electrical source, which could be single phase, three phase or inverter-based. In an AC RSW machine with a single phase source, zero power is achieved in each cycle of the alternating voltage wave form, which means there are energy losses happening and thus deteriorate the welding quality[23]. Based on these factors, inverter technology has been widely applied in the welding industry, which is the core technology of a DC RSW machine.

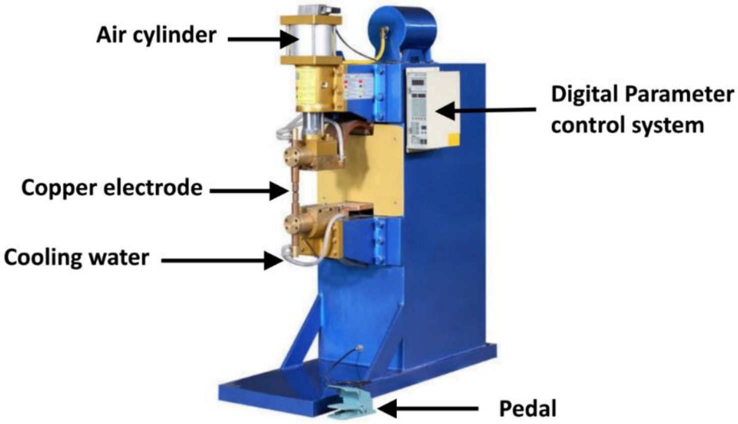

Figure 5 Schematics of a AC RSW Equipment

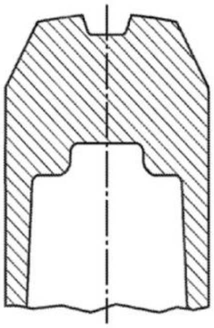

Figure 6 Cross-sectional View of a Typical Electrode

Inverter-based DC RSW systems will weld the metal sheet use the same mechanism, however, there are a few extra essential components needed as shown in Figure 7. In a DC RSW machine, three phase voltage is rectified to DC through the illustrated rectifier. The rectified DC wave is more precisely controlled, and will result in better welding performance. An Insulated

Gate Bipolar Transistor (IGBT) is used to convert utility power to high voltage energy, which gets stored in the capacitor bank, and then switched into a second transformer as required to produce the necessary welding current. The transformer has a high turns ratio, which means the welding process will be improved when used with an IGBT, because less primary current will be needed[24]. Furthermore, with the transition from AC single phase to DC three phase, the AC inter-cycle cooling effect will be eliminated and results in even better energy performance due to reduced secondary energy requirement and less welding time. However, since a capacitor bank can store a large amount of energy, it is possible that rupture of the IGBT could occur during operation if the circuit is not properly controlled, which possesses risks of damaging the equipment and causing operator injuries. In this study, the investigation has been focused on the effect of interlayer in RSW quality, thus the most common AC RSW machine is selected.

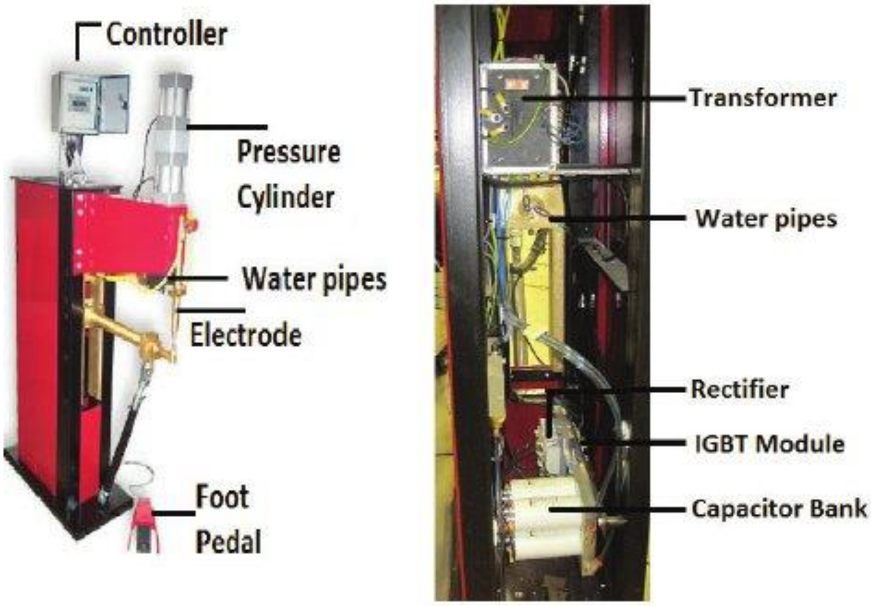

Figure 7 Important Components of a DC RSW Machine

As mentioned above, an AC electric current is supplied through copper electrodes connected to the secondary coil of a welding transformer as shown in Figure 8[25]. As the current passes through the electrodes and metal sheet, different resistance sources will act as a heat sink to form the weld during the process. The resistance is categorized into bulk resistance and contact resistance, the bulk resistance of copper electrode is normally the minimum due to copper's high electrical conductivity, which prevents the sticking of electrodes onto metal sheet as well as excessive consumption of electrodes. The contact resistance between electrodes and metal sheets is also insignificant due to the same reason, while the bulk resistance of the metal sheets is dependent on the sheet material properties and thickness. The most significant resistance type is the contact resistance between two metal sheets, this is also the main energy source for the formation of welds.

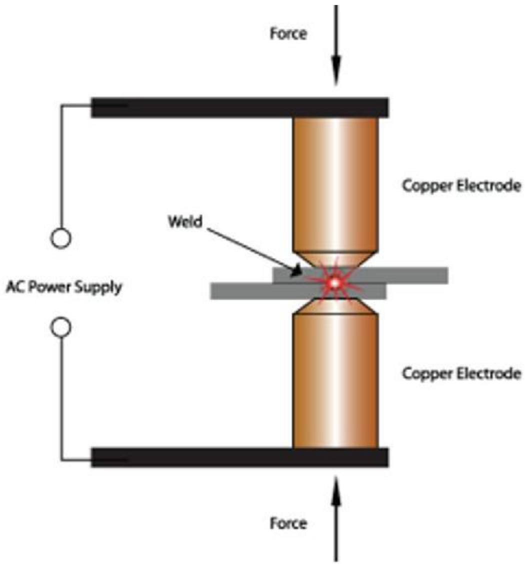

Figure 8 Process Illustration of RSW

After the formation of weld, the weld can be microstructurally divided into three major zones as shown in Figure 9, which are: Fusion Zone (FZ), Heat Affected Zone (HAZ), and Base

Metal (BM)[26]. FZ refers to the weld nugget area where complete melting occurs, and the BM is where no property changes occur through the welding process, while the HAZ refers to the non-melted region where properties change due to the exposure to high temperature[27]. Since the HAZ often possesses different properties than the base material, the formation of HAZ can cause change in strength, susceptibility to cracking, reduced corrosion resistance or lower toughness, which makes this area a typical failure location.

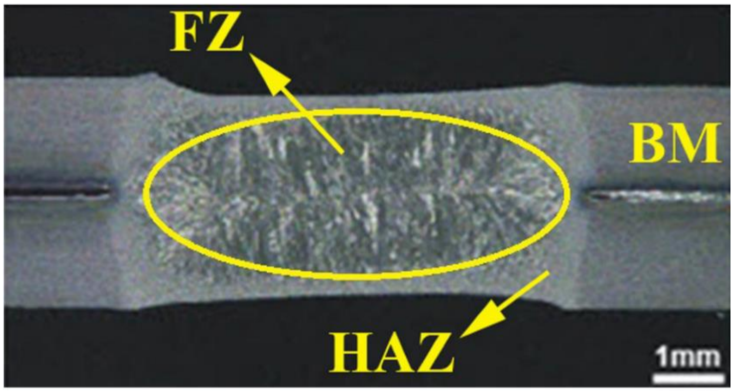

Figure 9 Microstructural Zones of a RSW joint

2.2.3 Important Parameters of RSW

To ensure good quality RSW joints, many parameters needed to be considered, and they often act either independently or cooperatively through the whole RSW process. A typical welding process is illustrated in Figure 10, step 1-2 represents the pre-squeeze stage, in which the electrodes clamp the metal sheets and direct contact is established[28]. In this stage, the closing speed of electrodes needs to be controlled to avoid excessive electrode wear. Step 2-3 is the squeeze stage, designated force is applied to make more solid contact by possibly deforming the metal sheets, and this force will be maintained until the end of the hold stage. This applied pressure has an inversely proportional relationship with the contact resistance and heat generation because closer contact made by higher pressure will enlarge the actual metal-to-metal contact area. Stage 3-4 represents the actual weld stage, in which current is passed through the assembly and heat is generated to produce the weld. In this stage, the important parameter is welding current and weld time. Welding current is the one with the largest impact on the heat generation, the mechanical properties could be improved with the increase in welding current, however, when the current is too high, too much heat generated will also cause expulsion and other defects formation. Stage 4-5 is the hold stage, in which there is no more current running through, but the force is still applied to allow solidification of the molten nugget. In this stage, the cooling water running through the electrodes and the unreacted bulk material will act as energy sink to absorb redundant heat, enough holding time and sufficient solidification can provide structural strength. However, if the holding time extends for too long, it also adds possibility of forming porosities and void shrinkages. The last stage is the release stage, this will happen once proper hold time has been established and the whole welding cycle is then complete.

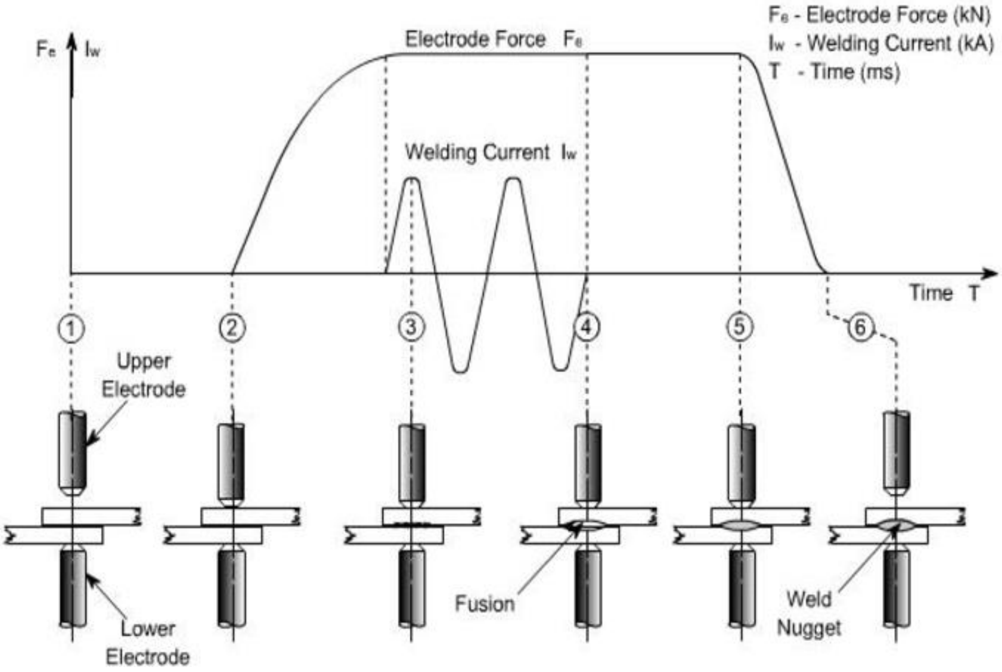

Figure 10 Different Significant Stages of RSW Process

2.3 Dissimilar Welding of Al to Steel

2.3.1 Al Alloys and Steel

In the automotive industry, friction stir spot welding (FSSW) has gained some utilization to produce joints in aluminum body structures due the low heat input used, defect-free joint quality, and lower thermal distortion, however it requires a long processing time and costly investment to implement FSSW machines in a massive manufacturing environment[29]. In contrast, ever since the development of RSW, it has become the dominant welding process because of its cost-effective advantage which can meet the essential criteria of every automotive manufacturing with high reproducibility and automation[30]. Besides the welding process, material selection is also important in the design of vehicles. Conventionally, steels are widely used, since their primary constituent is Fe, which offers low price, recyclability, excellent shock absorption properties, and good strength performance[31] . However, light weight is an increasing priority for modern vehicles. In 2005, a project named as SuperLIGHT – CAR (SLC) was initiated in Europe with the objective to reduce the body weight by at least 30%. The final concept of the design in this SLC project is shown in Figure 11[32]. The material proposed to be used the most is aluminum, which accounts for 53% of the total weight. Aluminum does not only have low weight, but also good formability, high strength to weight ratio, and good corrosion resistance, which makes them a great option for the manufacturing of chassis, doors, and hoods. There are a lot of connection points needed to be established between aluminum and steel in this car body design, and except for the light-weight vehicle production, many other situations would prefer the solid bonding between Fe and Al alloys such as household applications and chemical industry with high thermal conductivity and high temperature corrosion resistance requirements[33].

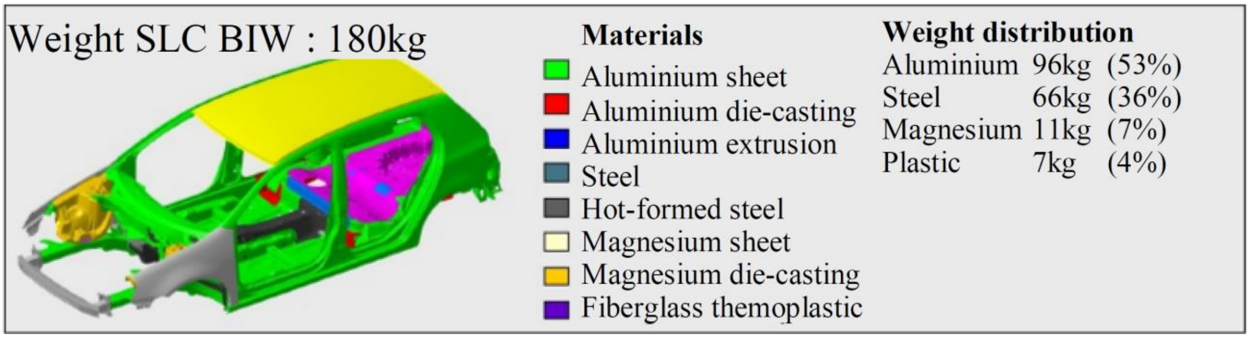

Figure 11 SLC Project Design Graph

2.3.2 Metallurgical Reactions During Welding Process

It has been proven in the previous section that the successful joining of Al alloys to steel is very beneficial, however, during the welding process, the formation of intermetallic compound (IMC) are inevitable as shown in Figure 12, even though they are necessary for the strong atomic-scale metallurgical bonding along the interface, the brittle nature accompanied with internal stress drastically reduces joint reliability[34].

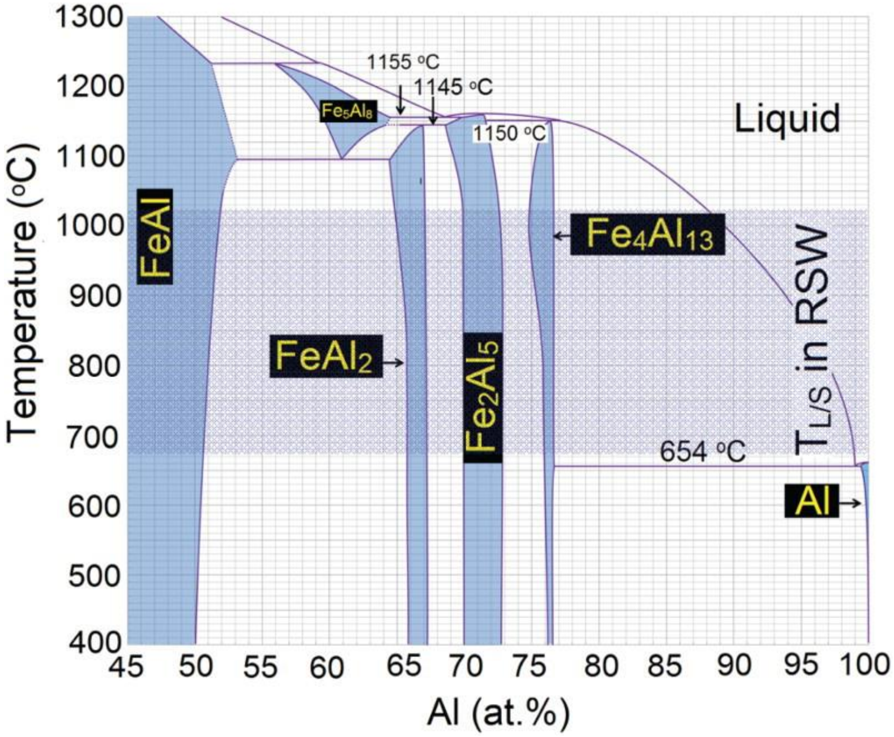

Figure 12 Phase Diagram between Fe and Al

As the current passes through the metal sheets and heat is generated, the Al sheet has higher thermal conductivity and this increases the thermal gradient between the steel and Al. In this case, due to the low melting point of Al, the liquid nugget will be formed in the Al sheet and an independent nugget might also be formed in the steel sheet depending on the amount of accumulated heat in steel. The brazing mechanism will then facilitate the metallurgical bonding along this liquid/solid interface. Once the liquid/solid interface is established, wetting of solid steel by liquid Al initially hindered by the Al oxide layer will start with the help of generated heat and applied force. At this moment, joint interface will aim to reach an equilibrium stage, this change in composition is carried out by the dissolution of the base metal. However, due to the nearly zero mutual solubility of Fe in Al, this process eventually leads to the formation of

IMC. It is noted that the Al-rich intermetallic Al_5Fe_2 and $Al_{13}Fe_4$ which have low symmetry crystal structure are more detrimental than their iron-rich counterparts such as Fe_3Al, and due to the higher diffusivity of Al in Fe than vice versa, the atom-atom metallurgically bonded Al-rich IMCs also outnumber iron-rich ones as shown in Figure 13[35,36]. Heumann and Dittrich also proved through X-ray diffraction (XRD) that Al_5Fe_2 with a high hardness and low fracture toughness is the dominant reaction product at the weld interface due to its parabolic growth trend within the temperature range of 715-944 ºC caused by its open and anisotropic crystallographic arrangement[33,37,38]. Therefore, controlling the thickness of IMC becomes largely dependent on the diffusion-controlled growth rate of Al_5Fe_2, which can be affected by welding heat input, composition of Al alloys and steel, coating composition of steel, and interlayer application.

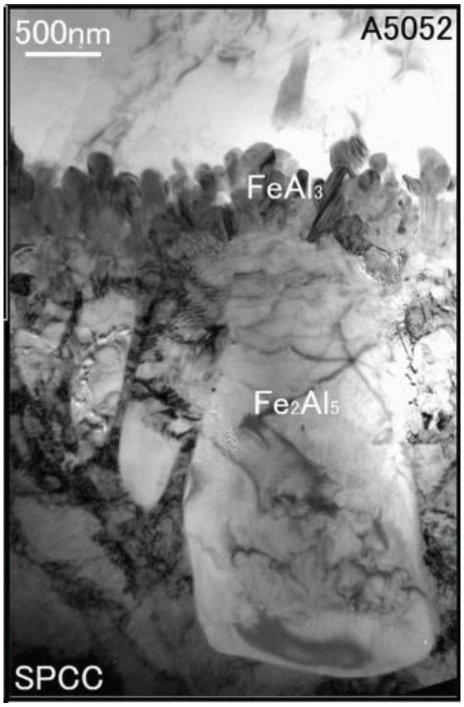

Figure 13 Intermetallics Formation during RSW of Al to Fe

2.3.3 Significant Factors Related to Mechanical Properties

Once the weld has formed as described in previous section, the mechanical properties are often the primary index to evaluate weld quality. There are a few factors that are closely related to mechanical strength, including bonding zone length, defects at joint interface, thickness of IMC layer, and electrode indention in Al sheet as illustrated in Figure 14[34].

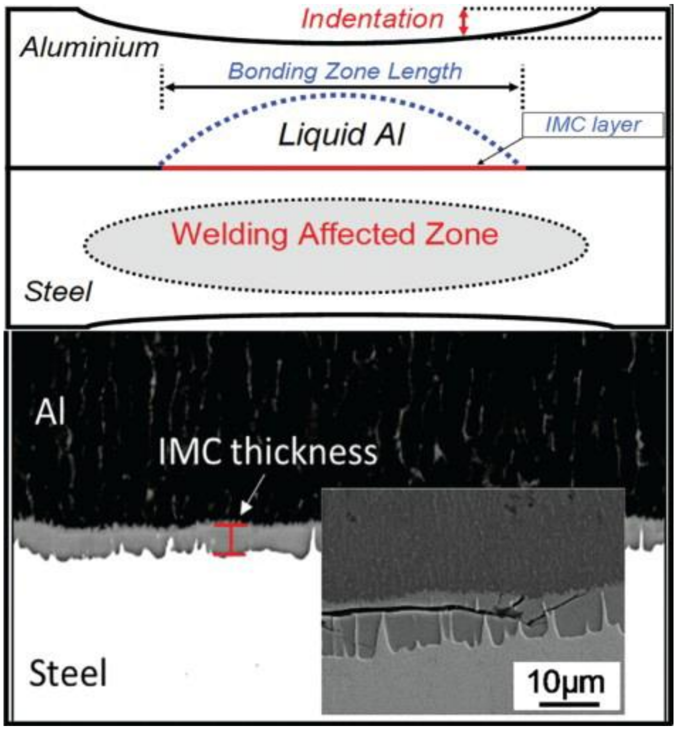

Figure 14 Significant Properties of RSW Assembly

Bonding zone length refers to the length of the liquid aluminium nugget specifically and is directly related to the heat distribution at the faying surface. The applied load will have its effect through this region, which means the load taken by the sample is largely dependent on this property.

Defects at the joint interface will also negatively affect the mechanical performance, including porosity and void located in Al nugget along the faying surface. Their formation mainly contributes to the Al solidification shrinkage, melt expulsion and steel vaporization. According to the wetting mechanism mentioned in previous section, if the break-up of Al oxide layer is nonuniform, defect as discontinuous IMC layer will thus form.

Thickness of the IMC is another important feature, for which it represents the kinetics of liquid/solid interface reaction and a weak spot in the weld joint, and so the thickness of IMC can significantly determine the failure mode of the sample. There are three main failure types, differed by their different fracture paths as shown in Figure 15[39]. While the IMC thickness is larger than critical value (between 1 – 10 µm), crack propagation through the irregular Al_5Fe_2/steel interface becomes less energy preferably, thus the high hardness and low fracture toughness IMC layer dominates the path of resulting in interfacial failure mode. On the other hand, while the IMC thickness is below the critical value, and defects are present at the interface, the partial interfacial failure mode will be favored along the interface between IMC layer and Al metal sheet and further go into the Al side. However, if the bonding zone length is ideally long and the IMC layer is thin and uniform, large fracture energy will be consumed, in this case failure will happen in the form of nugget withdrawal from Al side[34]. Among all failure modes, the pullout failure mode is the most favorable, except for the case in which nugget removal happens due to excessive thinning of the Al sheet.

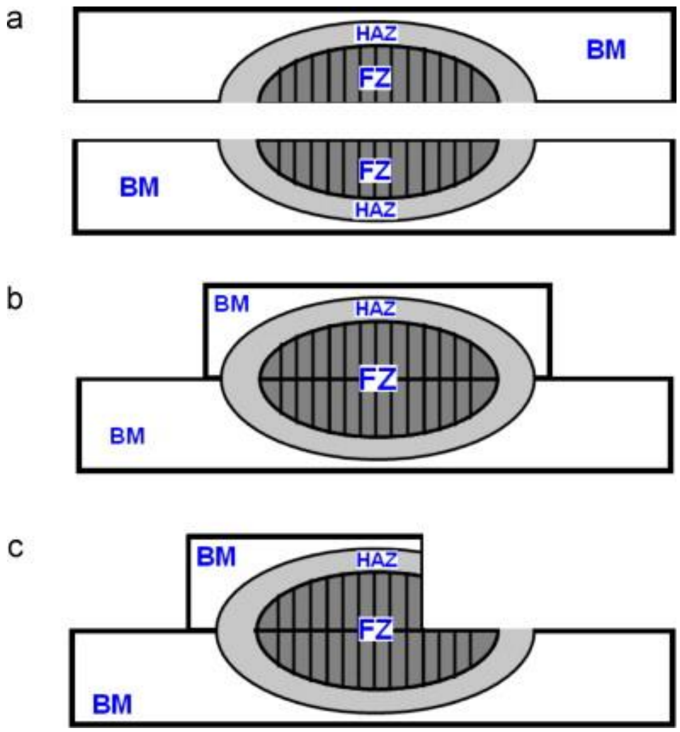

Figure 15 Different failure modes during tensile-shear test: a)interfacial b)pull-out c)partial interfacial

The last factor is the electrode indention in Al sheet, which refers to the magnitude of vertical deformation happening after welding, this property is a function of heat input, electrode force and electrode geometry. Electrode indention is also greatly associated with expulsion happening during welding, expulsion will influence the mechanical performance as shown in Figure 16, weld with smaller nugget size (shorter bonding zone length) but no expulsion could have better performance than some of those with larger nugget size accompanied with expulsion[40]. Moreover, in the resistance spot welding for low carbon steels, excessive indention can also contribute to the alternating of failure location as shown in Figure 17, failure originally located far away from weld nugget, after experiencing expulsion, due to the increased stress state, the failure location shifts to the boundary of FZ/HAZ located at the edge of nugget. The failure location path length is reduced, and thus the peak load is reduced, moreover the failure location has been changed from base metal to fusion zone, as shown in Figure 18, the hardness in fusion zone is much higher than that in base metal due to its martensitic microstructure, which could result in a higher load bearing capacity. However, the high hardness degrades the weld ductility and thus reduce the energy absorption ability.

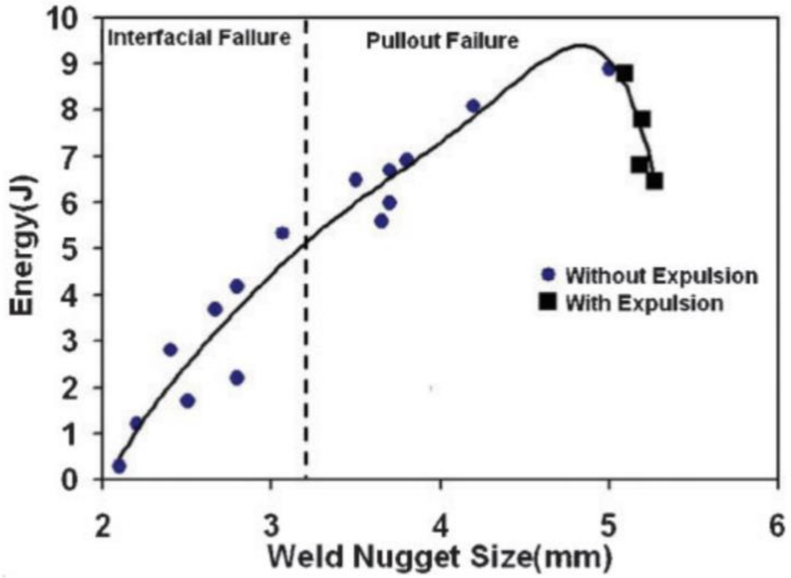

Figure 16 Effect of Expulsion on Weld Nugget Size

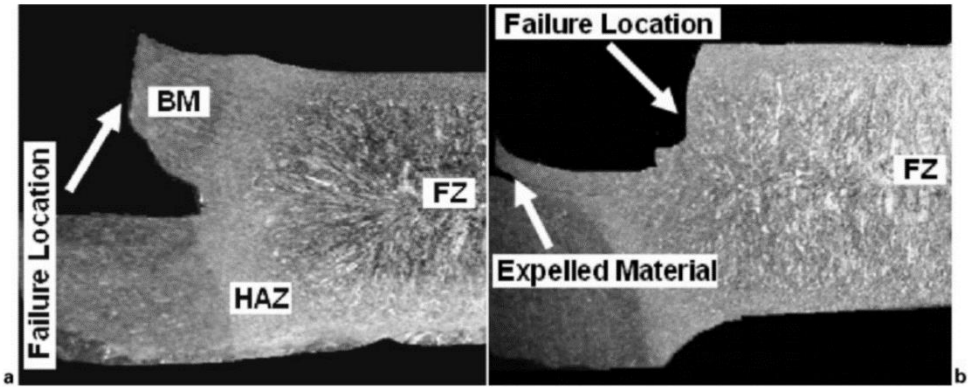

Figure 17 Failure location of spot welds a) without expulsion and b) with expulsion

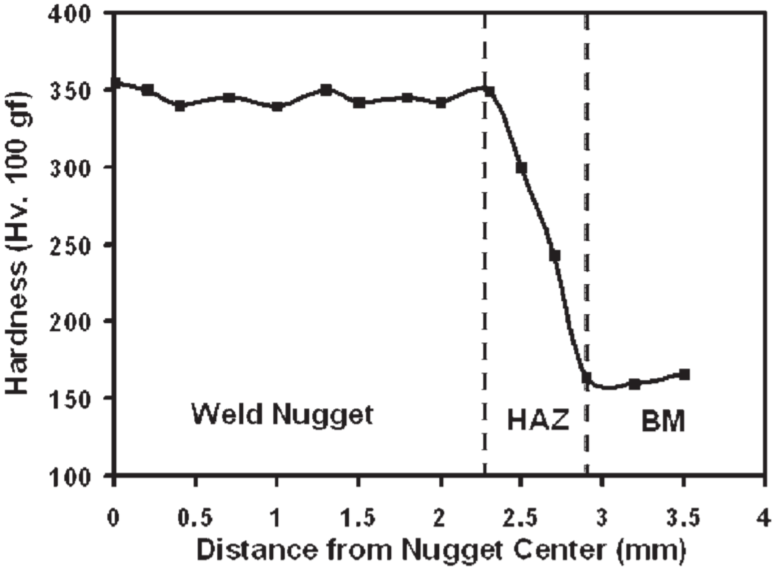

Figure 18 Hardness Profile through Welds

2.3.4 Different Approaches to Improve the Joint Properties (Welding Quality)

Researchers have never stopped the progress in improving the weld quality, and a few accessible methods were proposed and approved, including the control of weld heat input, application of cover plate, addition of silicon, application of zinc coating, and application of interlayers.

When controlling the heat input, the key is to control the welding current, welding time and electrode force applied. Different levels of heat input will have a significant impact on several factors, including interface temperature, thickness of IMC layer, indentation depth, interface defects, and HAZ softening phenomena. The effect of interface temperature, IMC layer thickness, indentation depth on mechanical strength, and interface defects has already been discussed in previous section, no further details will be provided here. HAZ softening phenomena is happening in Al sheet and is due to grain coarsening, loss of strain/precipitation hardening effects. The optimization of welding heat input is a complicated process, since excessive heat input will promote formation of defects, and insufficient heat input will lead to insufficient melted contact areas and inadequate consolidation.

As mentioned above, enlarging the bond zone length could effectively improve the mechanical performance, and due to the high thermal conductivity of Al, simply increasing the welding current could highly increasing the interface temperature thus the bonding zone length. However, this increase in thermal input will cause severe problems like electrode degradation and indentation into the Al sheet. To avoid these, researchers have proposed a new method of putting high electrical resistance-low thermal conductivity material cover plate onto Al, a typical material used for cover plate is steel due to its low cost. When inserting steel plate into the dissimilar weld assembly, generated heat is conducted towards the Al/steel interface resulting in increased interface temperature, finite element analysis results show that an increase of 200–300°C can be achieved and hence enlarged bonding zone length[41,42,43,44]. With the application of cover plate, even though it will not affect much with the IMC growth, still much lower energy is needed to elevate the interface temperature, thus reducing the possibility of forming defects, the only limitation is that this method will largely depend on the thermal and electrical properties of the cover plate.

Unlike the two methods mentioned above which improves the mechanical strength from a thermal input perspective, this following method is working from a chemical addition side and is referred to the addition of silicon to Al, often in the form of insertion of Al–Si eutectic as filler material. When adding Si to Al, the liquid phase becomes the mixture of Si and Al, thus the reactant produced at the interface changes to Al alloy/Al_8Fe_2Si/$Al_{13}Fe_4$/Al_5Fe_2/steel[33]. Dong et al.

used Al–12% Si filler wires in GTAW of aluminum alloy to galvanized steel and found out that the tensile strength could increase from 63MPa with the application of Zn–15% Al filler wire, to as high as 135 MPa with Al–12% Si filler wires [45]. Figure 19 shows the elemental distribution of the weld made with these wires, from Figure 19c and Figure 19g, it is known that Si distributes in interfacial layer and the weld zone, from Figure 19b and Figure 19f it can be seen that Fe diffuses into those areas as well, with the increase in the Si content the diffusion of Fe can be effectively suppressed, thus the thickness of IMC layer can be decreased as shown in a and e and resulted in better tensile strength. In addition, the Si distribution in weld zone is along the grain boundary, then from Figure 19c, Figure 19g, and Figure 20 weld made with higher Si content results in finer grain size, thus further improve the mechanical performance. Moreover, some researchers also proposed that besides the mechanism mentioned above, the diffusion of Si could occupy the structural vacancies on the c-axis of the Al_5Fe_2 phase resulting in reduced atomic mobility and hence hindered IMC growth rate[46]. Similar methodology was also tested with Al-Cu, Al-Si-Cu, and Zn-Al filler materials, however, none of them showed better performance than Al-Si, either due to the thicker interfacial layer or the coarser dendrite microstructure formed in weld.

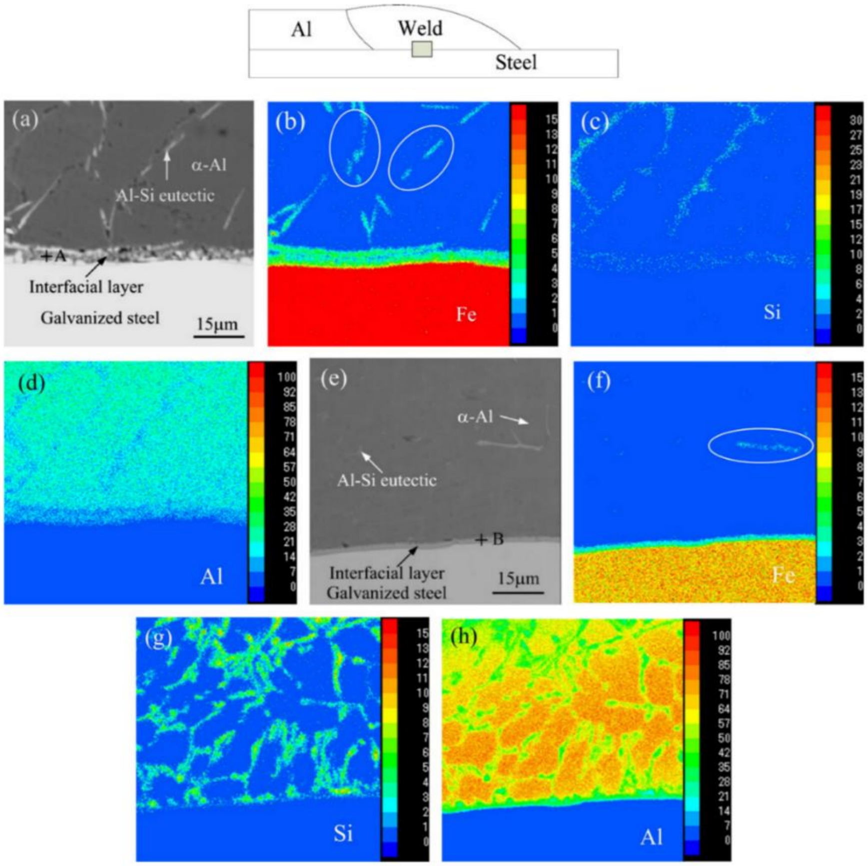

Figure 19 Elemental Distribution of Weld of Al to Steel

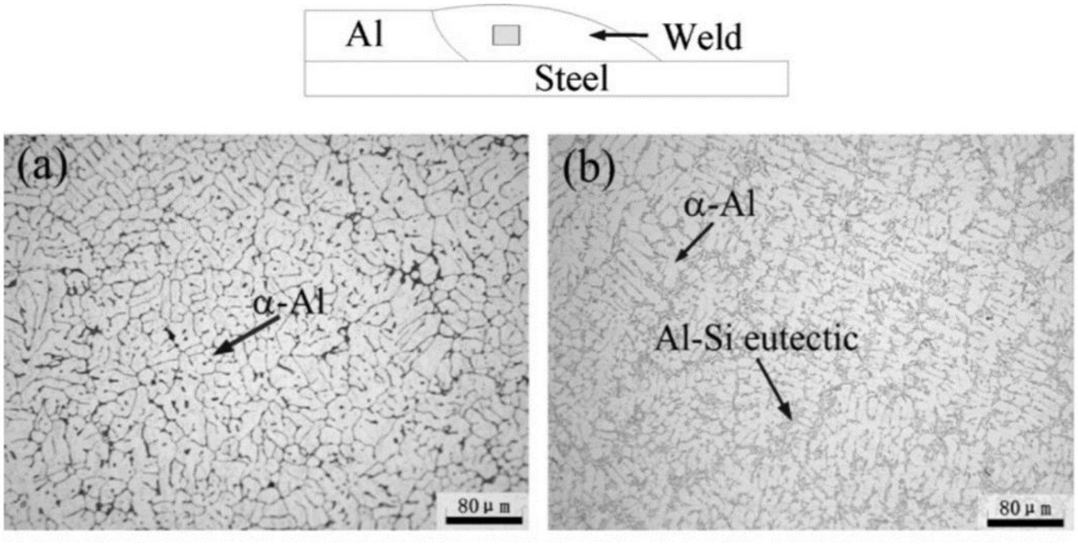

Figure 20 Microstructure of Weld of Al to Steel

Aside from insertion of Si filler material, the addition of Zn coating onto the steel does not only prevent corrosion but can also help to improve the weld quality. The oxide layer on top of aluminum alloy can possibly produce un-wetted and un-bonded regions in the weld zone, thus reducing the mechanical performance, often in order to fully remove this oxide layer a high amount of heat input is required; however, this will cause the thicker IMC layer formation, also decrease the mechanical performance. With the presence of Zn coating, the fluxing behavior at the faying surface can be enhanced due to the following mechanism. When heat is generated during welding, the Zn coating can be dissolved in liquid Al under relatively low temperature as refer to Figure 21, this way the steel surface is free of contaminants, such as oxides, thus effectively eliminate the un-wetted regions and ensure uniform reaction layer and IMC growth along the interface[47]. Furthermore, except for the elimination of oxide layer, better fluxing behavior could be ensured by pushing oxide-containing solution to nugget periphery, and in this situation, the applied electrode force and the electrode geometry will play an important role.

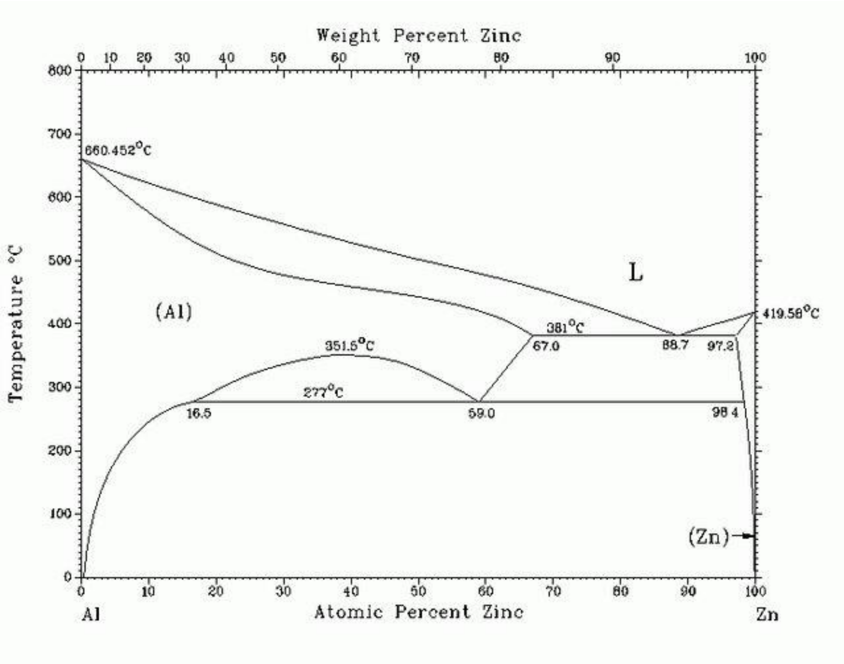

Figure 21 Phase Diagram of Al and Zn

It should be noted that the insertion of Al-Si filler wires is a type of interlayer application method, there also existing many other different types and modes of interlayers, which can be used to improve the mechanical performance. More details on the interlayer application in dissimilar RSW will be discussed in the next section.

2.4 Interlayer Application in Dissimilar RSW (of Al to Steel)

2.4.1 Background Information about Interlayer

Interlayer refers to the intermediate layer placed between base metals and act as buffers that bridge the wide differences in properties and in mutual solid solubility of the contacting components. It can also ideally attain solid solution with better properties or IMCs with low brittleness. In macrostructure perspective, it also acts as a macro interlock between materials. Many studies showed that copper, nickel, zinc, vanadium, niobium, silver, nanoparticles, and composites could be used as intermediate interlayers that effectively impede the formation of IMC[48].

The positive impact of application of interlayer material in dissimilar RSW of Al to steel has been approved by many researchers. An example of inserting a AlMg interlayer in the RSW Al alloy A6061-T6 and austenitic stainless-steel type 304 sheets, and an example of graphene interlayer in RSW between AISI-1008 steel/Al-1100 alloy will be discussed and compared to see how the addition of interlayer changed the microstructure of weld joint and helped with the weld joint strength improvement.

2.4.2 Interlayer Application Examples

Ibrahim et al. used AlMg alloy interlayer in the welding of aluminum alloy and stainless steel as shown in Figure 22[31]. After the weld has been formed, the fusion zone was identified in Figure 23, and two distinct zones were defined, the one on the Al side is connected to the interface and the one on the stainless-steel side is not exposed to the interface. During the welding process, it was investigated in the line scan shown in Figure 24 that the AlMg interlayer material got melted and filled the gaps caused by roughness between two metal sheets due to the lower melting point, which effectively established joining resulting in higher mechanical strength.

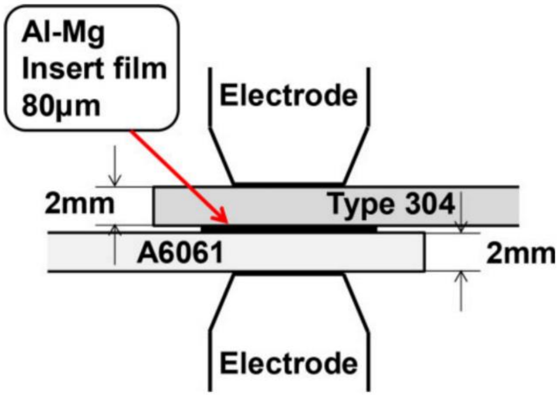

Figure 22 Illustration of insert AlMg Film

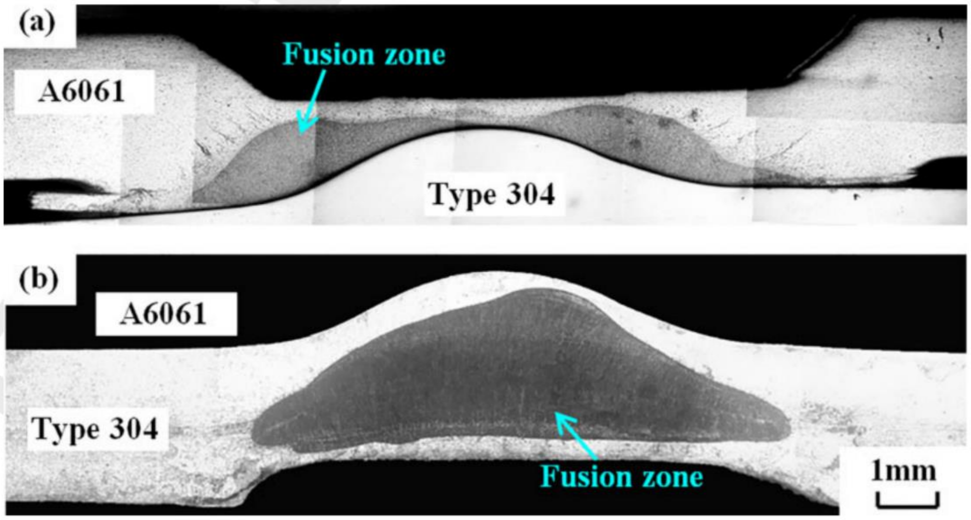

Figure 23 Fusion Zone Formation During RSW

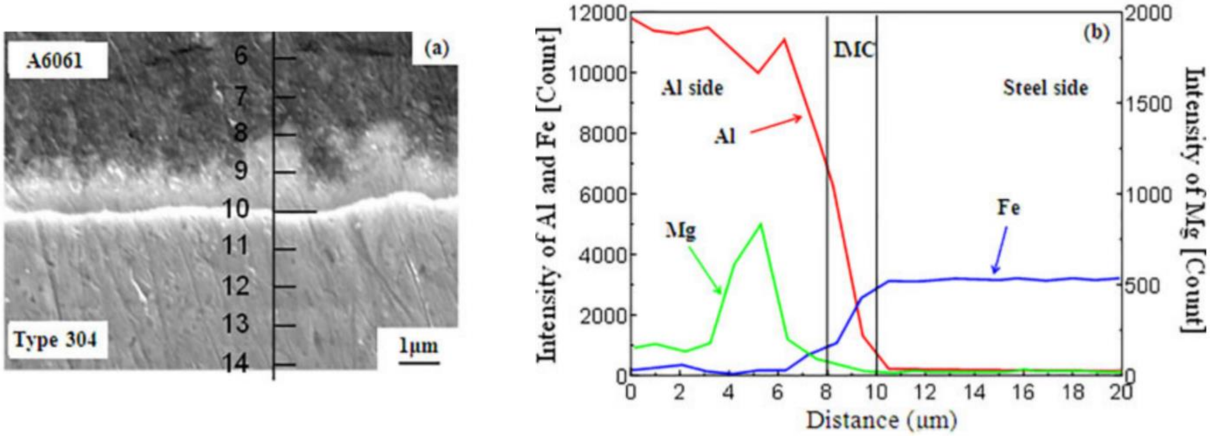

Figure 24 a) image (SEM) at interface near centre of nugget; b) EPMA line analysis along line in a)

Das et al. used graphene nanoplatelets as interlayer material, the graphene was mixed in a polyvinyl alcohol (PVA) solution and then drop-casted on the steel portion as shown in Figure 25[49]. Lap tensile shear results in Figure 26 shows that the mechanical strength increased for almost all the operating parameters. Looking at the interface where IMC forms, it can be seen from Figure 27 that after the application of graphene the IMC thickness gets reduced significantly. This is because the presence of graphene interlayer inhibits the direct contact between two metal sheets. Futhermore, the presence of graphene particles also has been observed to resist crack propagation in steel side and the shear deformation in the Al sheet side. Besides the reduction in IMC thickness, there also existing other weld strengthening mechanisms including grain refinement, work hardening, Orowan strengthening and load transfer. Under Orowan strengthening mechanism, the presence of graphene particles hinders the movement of dislocation, and as the nanoparticles move in, the looping tendency also increases resulting in increased dislocation density and thus improved the strength.

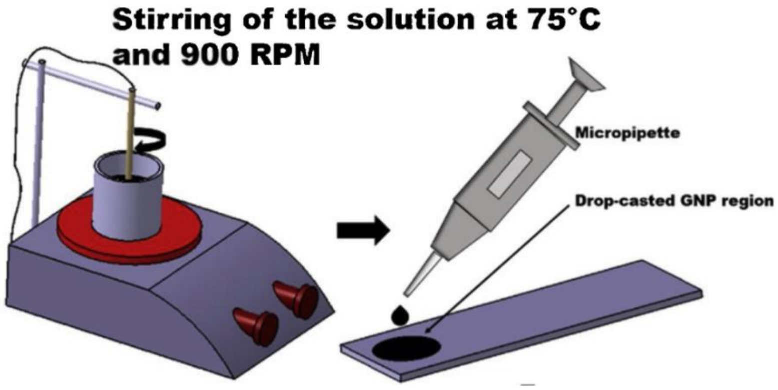

Figure 25 Preparation and Insertion Method of Graphene Interlayer

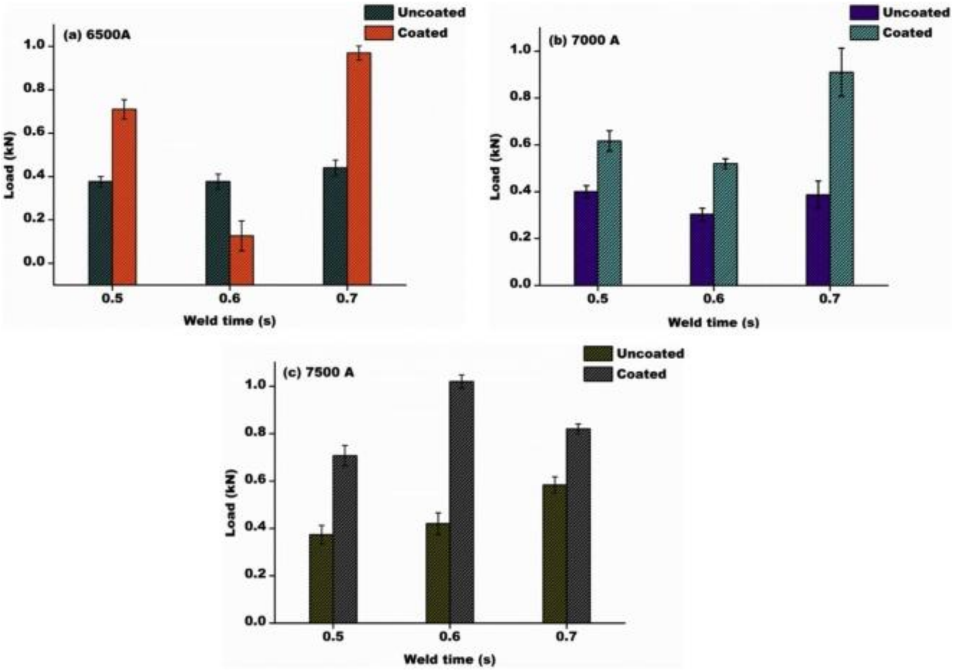

Figure 26 Mechanical Performance of Samples Welded with and without Graphene Interlayer under Different Parameters

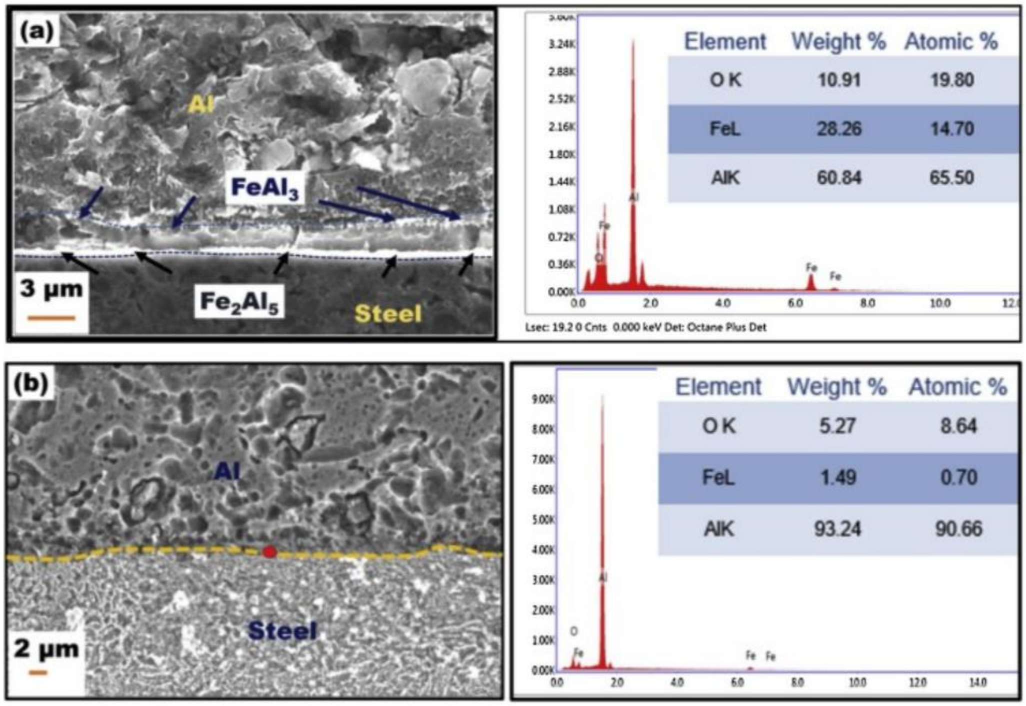

Element	Weight %	Atomic %
O K	10.91	19.80
FeL	28.26	14.70
AlK	60.84	65.50

Element	Weight %	Atomic %
O K	5.27	8.64
FeL	1.49	0.70
AlK	93.24	90.66

Figure 27 Microstructure Observed along the Interface of Sample Welded a)without interlayer; and b)with interlayer

2.4.3 Interlayer Selection

The use of interlayers have been shown to improve the weld performance, however selection of the best possible interlayer can still be a challenge. Many factors are related to interlayer selection, which are interlayer types, insertion methods, thickness, and so on.

Among several criteria on selecting the material type of interlayer the first is the melting point. The melting point of interlayer material should not be too high, because if incomplete melting of interlayer happens during the process, it will remain in the FZ and become a weak spot for the weld joint. Another point is that the thermal property of interlayer should be similar to the substrates because it is supposed to act as a bridge to minimize the mismatch, otherwise it will result in the production of even larger residual stresses and larger temperature gradients. The interlayer material should also be able to mix or react with the substrates to form preferred microstructure such as solid solution or IMCs with lower brittleness. Deng et al. performed dissimilar welding of Ti and Fe with the insertion of Cu foil, in this case Cu-Ti IMC was formed on the Ti side instead of Fe-Ti IMC, which results in lower brittleness[50]. In a system with more than two components with low mutual solubility, the preference in the formation of IMCs can be predicted by formation enthalpy. And the order of reactions happening in this system can be predicted by Gibb's energy of formation. Once the possible formation of IMCs has been predicted, a way to determine which IMC has lower brittleness is important in the interlayer selection process. Taking a cubic crystal class (independent elastic constants are C_{11}, C_{12}, C_{44}) IMC as an example, a way to quantify the brittleness of that IMC is given in Equation 2 and Equation 3.

Equation 2: Shear Modulus

$$G = \frac{1}{5}(C11 - C12 + 3 \times C44)$$

Equation 3: Bulk Modulus

$$B = \frac{C11 + 2 \times C12}{3}$$

in which, G is the shear modulus and B is the bulk modulus. The ratio between G and B is an important index of brittleness of IMCs[51].

Thickness of interlayer is another factor needed to be considered in interlayer selection process, because thickness of interlayer in welding process can greatly alter the material distribution and transfer of energy in the weld, thus influence the microstructure. If the thickness is too thin, reaction of the substrates will not be effectively suppressed, and many brittle IMCs will still form. If the thickness is too thick, interlayer will not be melted completely and left in the weld to become the weak spot for crack propagation.

Different modes of interlayer often refer to the state of interlayer, such as metal foil, metal filler, metal powder, cold spraying, electro-spart deposition, hot dipping interlayer, nanoparticles and so on. This criterion is more closely related to the feasibility during welding process, for example, electro-deposition technique has been widely applied in FSW because it can solve the situation where sometimes the insertion of foil-like interlayer is difficult.

Chapter 3 Materials and Experimental Methods

3.1 Material Selection

3.1.1. RSW Metal Alloys

The base metal sheet alloys selected for this study were GI DP600 with a thickness of 1.2 mm, and AA5052 with a thickness of 2.0 mm. Except for the difference in thickness, they also have significant dissimilarity in both chemical composition and many other properties as shown in Table 1 and Table 3, which makes this RSW process very challenging.

Table 1 Chemical Composition of Base Metals[52,53]

Material	C	Mn	Mo	Si	V	Cr	Ni	Cu	Al	Mg
DP600	0.107	1.497	0.214	0.175	0.044	0.181	0.015	0.057	0.038	-
AA5052	-	-	-	-	-	0.25	-	-	97.2	2.5

Table 2 Mechanical Properties of Base Metals

Material	Yield Strength (MPa)	Tensile Strength (MPa)
DP600	370	630
AA5052	65	170 - 220

Table 3 Thermal and Electrical Properties of Base Metals[54,55]

Material	Melting Temperature	Density	Thermal Conductivity	Electrical Resistivity	Latent Heat of Fusion	Specific Heat Capacity
Unit	[K]	[kg/m^3]	[W/(m×K)]	[ohm×m]	[J/g]	[J/(g×K)]
DP600	1803	7870	54	1.9e-7	247	0.44

AA5052	992	2680	138	4.99e-8	396	0.88

3.1.2. Interlayer Materials

The interlayer materials selected for this study were AA4043, AZ81A, IN625, and Ni99 their corresponding properties were shown in Table 4 and Table 5.

Table 4 Chemical Composition of Interlayer Materials [56]

Interlayer	Mg	Al	Si	Cu	Zn	Ni	Cr	Mo	Nb	Fe
AA4043	-	94.8	5.2	-	-	-	-	-	-	-
AZ81A	92	7	-	-	1	-	-	-	-	-
IN625	-	-	-	-	-	67.2	22.0	7.9	2.4	-
Ni99	0.15	-	0.2	0.25	-	Bal	-	-	-	0.4

Table 5 Thermal and Electrical Properties of Interlayer Materials

Material	Melting Temperature	Density	Thermal Conductivity	Electrical Resistivity	Latent Heat of Fusion	Specific Heat Capacity
Unit	K	kg/ m^3	W/(m×K)	ohm×m	J/g	J/(g×K)
AA4043	905.15	2690	163	4.16 e-8	396	0.85
AZ81A	694.15	1800	51.1	1.5 e-7	370	1.00
IN625	1623.15	8440	9.8	1.29 e-6	290	0.41
Ni99	1728.15	8880	60.7	6.4 e-8	305.6	0.46

3.2 Experimental Equipment

3.2.1. ESD machine

In this study, a Huys Industries ESD machine as illustrated in Figure 28 was used to deposit different interlayer materials onto DP600 metal sheet. Argon gas with a flow rate of 10 L/min was applied in most of the processes as a barrier between air and deposition layer to prevent oxidation from happening.

Figure 28 Schematics of ESD Equipment

3.2.2. RSW machine

In this study, resistance spot welding was conducted by a 60 Hz alternating current (AC) resistance spot welder as illustrated in Figure 29. Copper class II electrodes provided by Huys with a contact diameter of 6 mm were used in all RSW process with various current selection for different interlayer selection. Both electrodes also play an important role in the heat generation and heat transfer of RSW process, its thermal properties are listed in Table 6.

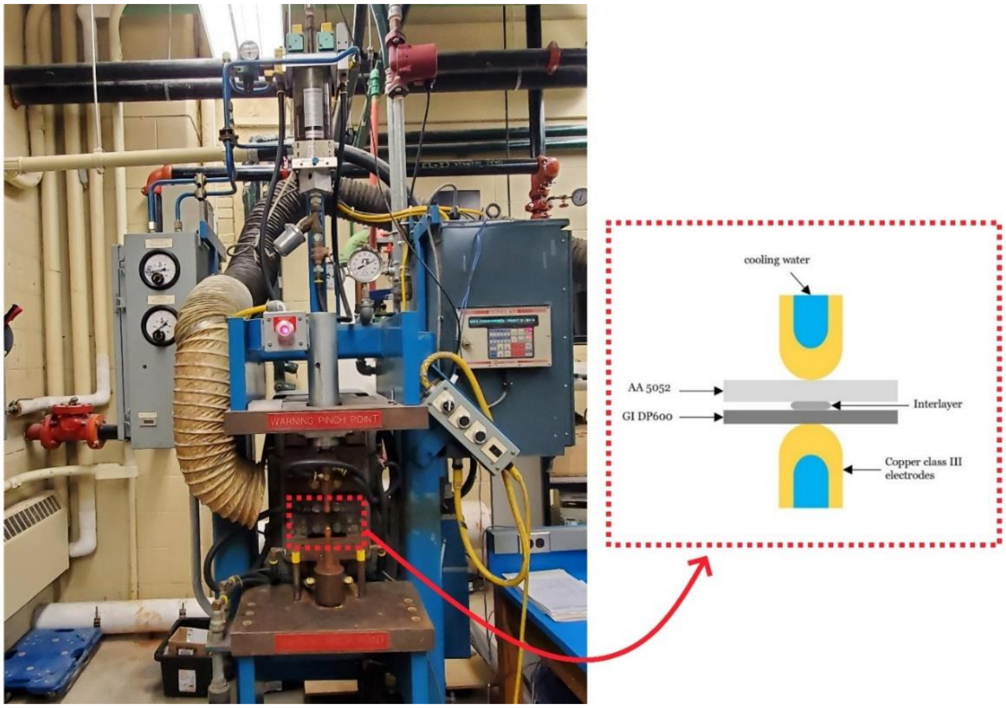

Figure 29 Illustration of AC RSW Equipment

Table 6 Thermal and Chemical Properties of Copper Electrodes

Material	Melting Temperature	Density	Thermal Conductivity	Electrical Resistivity	Specific Heat Capacity
Unit	K	kg/ m^3	W/(m×K)	ohm×m	J/(g×K)
Copper	1803	8890	385	1.7 e-8	0.44*

3.3 Metallographic Characterization

3.3.1. Sample Preparation

For sample preparation, an abrasive cut-off saw, and precision saw were used to cut the samples into ideal dimension along desired direction. Processed samples then were hot mounted by Struers MultiFast resin and PolyFast resin for the purpose of observation under OM and SEM, respectively. Mounted samples were grinded by sanding papers with the grit level of 180, 320, 400, 600, 800 and 1200, and then got diamond or alumina polished to finish for final examination. For more detailed microstructural observation, Keller's etchant was used to etch the aluminum alloy.

3.3.2. Optical Imaging

An Oxford BX51M optical microscope was used as shown in Figure 30 to observe the sample and capture the optical image in this study. This microscope has five different magnification levels, 5x, 10x, 20x, 50x, and 100x.

Figure 30 Optical Microscope

3.3.3. Electron Imaging and Elemental Analysis

Zeiss UltraPlus scanning electron microscope (SEM) with an AMETEK energy-dispersive X-ray spectroscopy (EDX) attachment as shown in Figure 31 was used in this study to get further information about surface topography and elemental analysis of samples.

Figure 31 Scanning Electron Microscopy[57]

3.4 Mechanical Testing

3.4.1. Tensile Lap Shear Test

Tinius Olsen H10KT tensile tester was used in this study to test the overlapped samples to obtain their mechanical strength, a shim pad on each end of weld assembly was used to prevent eccentricity during loading as illustrated in Figure 32. Tensile lap shear strength is an important index for the welding quality.

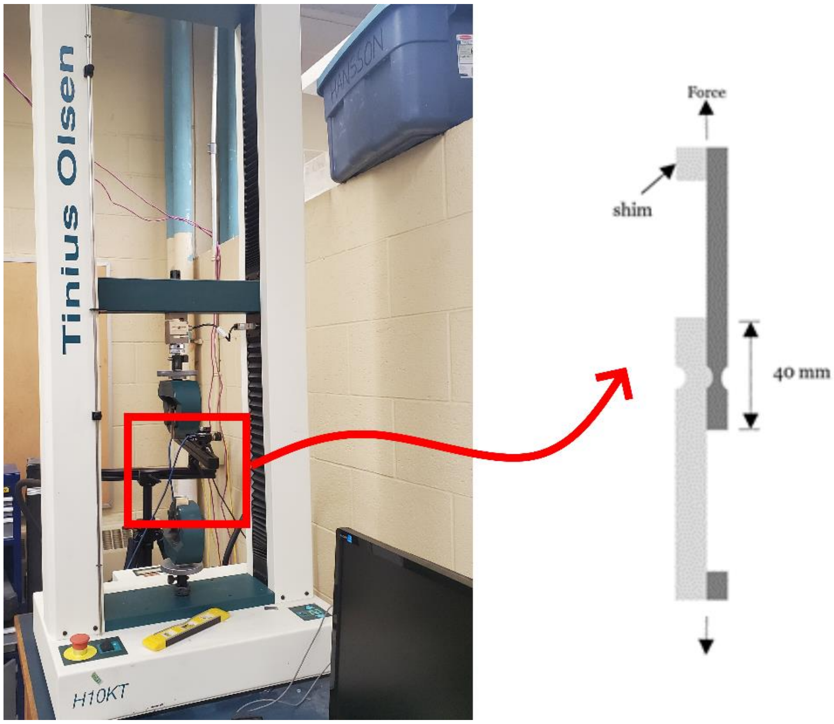

Figure 32 Tensile Testing Machine

3.4.2. Destructive Peel Test

Destructive peel test was performed as shown in Figure 33, with one side of the sample clampled within the bench and other side bended and clampled to allow peel force to be applied. This will allow the clear examination of nugget size, which is an important charateristic for welding sample’s mechanical performance.

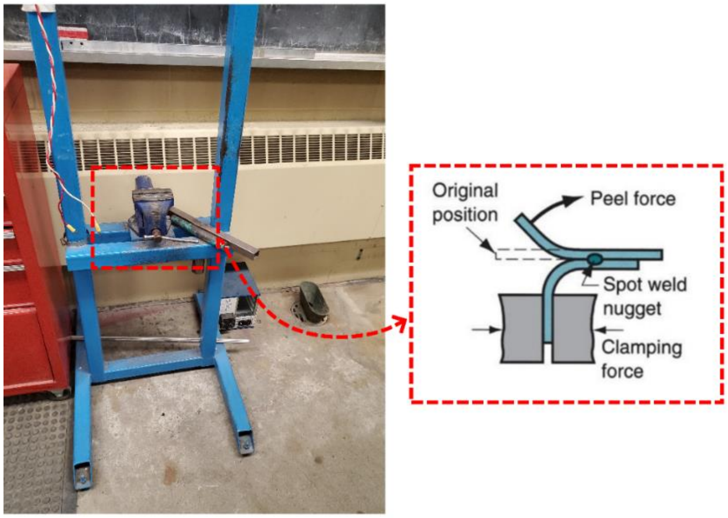

Figure 33 Peel Testing Station[58]

3.4.3. Microhardness

Microhardness tester shown in Figure 34 was used in this study to obtain the hardness of samples, which helps to determine how materials perform in dynamic conditions and how hardness will be affected by the dissimilar welding process. It is often used along with the OM to establish a hardness graph through different locations of the weld sample.

Figure 34 Microhardness Tester[59]

3.5 Experimental Methods and RSW Simulation

In this study, different interlayer materials were first deposited onto DP600 under various ESD operating parameters and taken the cross-section to examine the coating quality to select the optimized parameter set. Once the parameters have been decided for each interlayer material, they will be deposited onto DP600 within a circle of diameter of 1.5 cm and welded with AA5052 using the same parameters as shown in Table 7 (one cycle = 16.67 ms) for all runs under various current conditions.

Table 7 RSW Operating Parameters

Electrode Clamping Force (kN)	Cooling Water Flowrate (L/min)	Total Squeeze Time (Cycles)	Weld Time (Cycles)	Hold Time (Cycles)
3	5	50	20	20

The thermal properties of an interlayer are expected to play a significant role in the resistance spot welding parameters needed to obtain a joint. To assist with the selection of process parameters, a 2D simulation of heat generation and heat diffusion during resistance welding was performed. The geometry was chosen (Figure 35) to represent the joining of an AA5052 sheet to a DP600 sheet with three different interlayer materials pre-applied to the DP600 sheet: an aluminum alloy (AA4043), a magnesium alloy (AZ81A) and a nickel alloy (IN625). The zinc coating on both sides of the galvanized DP600 sheet are assumed to be negligible and the interlayer thickness – which varies depending on the material – is obtained from experimental measurements.

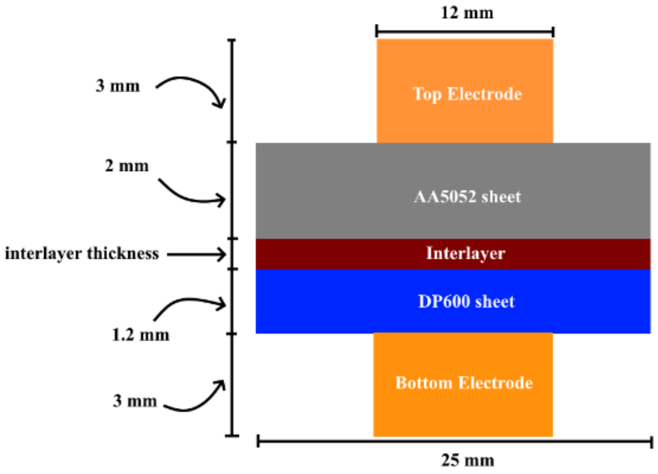

Figure 35 Graphical Demonstration of Weld Assembly

According to the heat diffusion equation, the change in temperature can be expressed in terms of the change in coordinates (x,y) and the change in time (t) as shown in Equation 4:

Equation 4: Change in Temperature

$$\frac{\partial T}{\partial t} = \alpha\left(\frac{\partial^2 T}{\partial x^2} + \frac{\partial^2 T}{\partial y^2} + \frac{\dot{g}}{k}\right)$$

in which α is the thermal diffusivity, $\dot{g}$ is the volumetric rate of heat generation, and k is the thermal conductivity. To determine the temperature distribution over time, the spatial dimensions in Equation 4 were discretized and solved with the use of a central finite difference method. The welding time during which a current is applied is held at 20 cycles, and assumptions are made to simplify the model: bulk heat generation is allowed to occur within both electrodes, the DP600 sheet, the interlayer, and the AA5052 sheet, while the only unbonded interface that is assumed to generate heat is the AA5052/interlayer interface. The amount of heat generated both in the bulk and at the AA5052/interlayer interface can be expressed as shown in Equation 5:

Equation 5: Heat generation

$$\dot{g} = I^2 \frac{R}{V}$$

in which I is the current running through the assembly, R is the resistance, and V is the volume of the assembly. The bulk resistance uses a definition of R shown in Equation 6, while the contact resistance uses a different definition for R shown in Equation 7:

Equation 6: Bulk resistance

$$R = \frac{\rho \Delta x}{A}$$

Equation 7: Contact resistance

$$R = 0.89\rho \left(\frac{\xi H}{\eta F}\right)^{\frac{1}{2}}$$

in which ρ is the electrical resistivity, Δx is the distance along the current path, A is the cross-sectional area, H is the material's Brinell hardness, F is the applied force exerted by the top and bottom electrode onto the weld assembly during the RSW process, ξ is a pressure factor, and η is the contact spots factor [60,61]. A constant stream of cooling water flowing through the interior of the electrodes was used to prevent overheating and degradation of the electrodes with repeated use. For this reason, the Dirichlet boundary condition in Equation 8 is used to fix the electrode/water boundary temperature. All other boundaries are assumed to be in contact with the surrounding air and are modelled under the assumption that the surrounding air acts as an insulator. This is done with the use of Neumann boundary conditions shown in Equation 9, while the temperature of the surrounding air was kept at 298.15 K.

Equation 8: Dirichlet boundary condition

$$T(x) = 283.15$$

Equation 9: Neumann boundary conditions

$$\frac{\partial T}{\partial y} = 0, \qquad \frac{\partial T}{\partial x} = 0$$

Of the three main process parameters in RSW – force, time, and current – both force (3 kN) and time (335 ms) are selected according to previous publications on the joining of aluminum to steel [62,63] and current is allowed to vary. As the interlayer material reaches the melting point, the additional energy requirement to cause a change in state from solid to liquid is also considered by incorporating the material's heat of fusion. This is then used to identify the current required during welding to achieve melting in the interlayer. Additional material properties used for the simulation are included in Table 8.

Table 8 Hardness Values of Materials used in Experiments

	Hardness
Units	kgf/m^2
AA4043	7.7E7
AZ81A	5.5E7
IN625	2.0E8
AA5052	6.0E7
DP600	-
Cu	-

The simulation results are presented in Figure 36. The peak temperature at the joining interface is recorded at each current until the melting point is reached. IN625 has the lowest thermal conductivity and highest electrical resistivity, such that reaching the melting point in the interlayer requires the lowest current (3 kA) of the three investigated interlayers even though the melting temperature is the highest. The AZ81A interlayer is expected to require greater than 5.5

kA before melting occurs, while the AA4043 interlayer is expected to require greater than 7.5 kA.

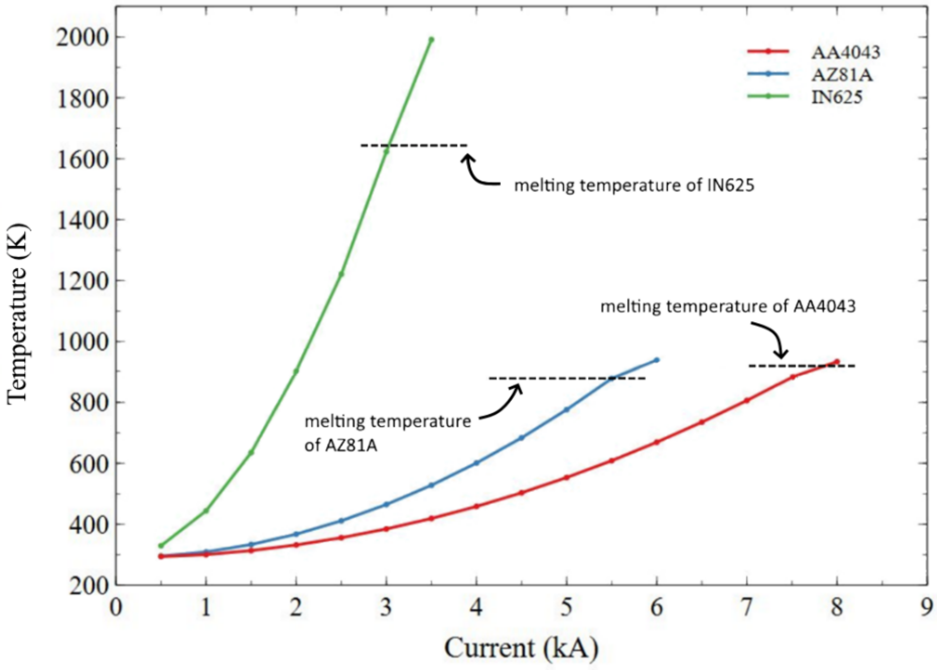

Figure 36 Simulated Temperature Profile for Different Interlayer Materials

Differences in interlayer properties are found to have a significant influence on the temperature distribution during welding as shown in Figure 37. The high thermal conductivity of the AA4043 interlayer can rapidly remove heat from the AA5052/AA4043 interface where heat generation occurs. Instead, peak heat buildup occurs within the DP600 sheet near the AA4043/DP600 interface. The similar thermal conductivity and electrical resistivity of AZ81A compared to DP600 results in peak temperatures at the AA5052/AZ81A interface, since the interlayer acts as an extension of the DP600 sheet from a thermal point of view. However, the low thermal conductivity and high electrical resistivity of IN625 when compared to the DP600 sheet contribute to the peak temperature occurring within the IN625 interlayer.

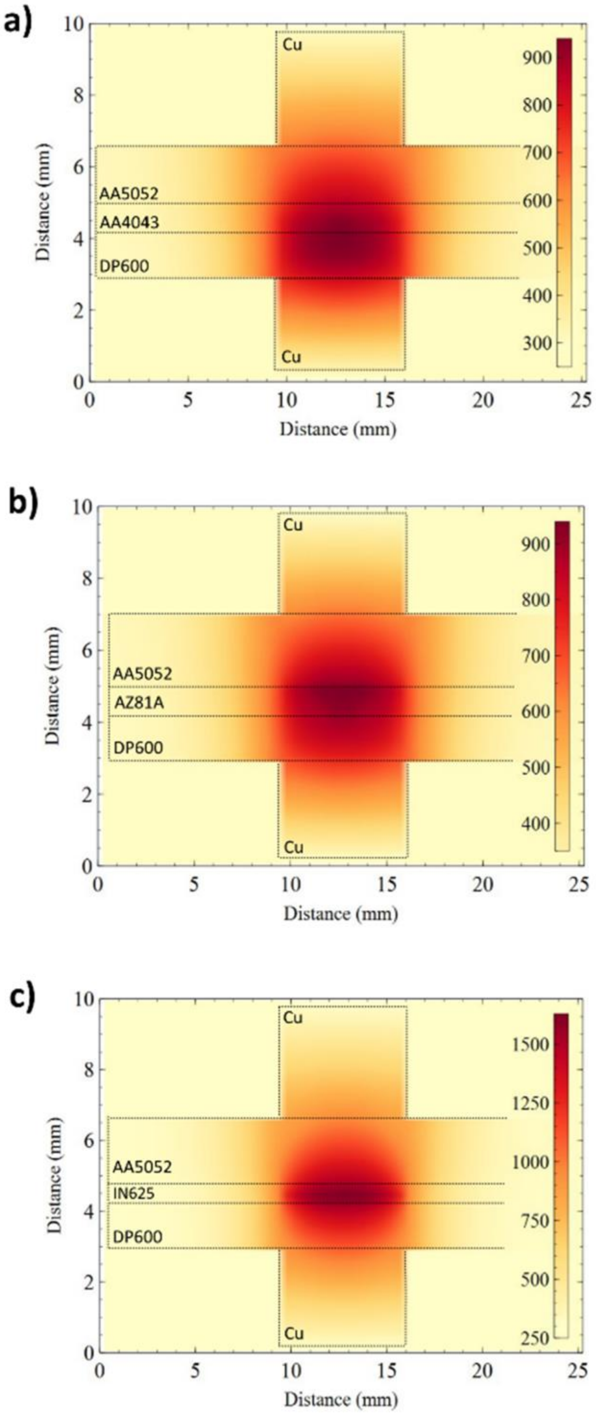

Figure 37 Simulated 2D Temperature Heat Map of Different Interlayer Materials

Chapter 4 ESD Interlayer

4.1 Interlayer Material Selection

Prior to this study, a preliminary test was performed by previous researcher, two interlayer materials AA4043 and IN718 were roughly tested to see how the application of interlayer might cause change in microstructure of weld. With the application of AA4043 onto DP600 as shown in Figure 38a, a layer of Fe-Al IMC was formed, which was expected to happen as described in previous literature review section. For the application of IN718 as shown in Figure 38b, interfacial cracks appear along the AA 5052 side and comparing to the composition of IMC formation is also more complicated. A closer look was then taken at the faying interface, by electron mapping shown in Figure 39, two different kinds of IMC were formed, which are Fe-Al and Ni-Al, Fe-Al located near the top of the interlayer region, which is closer to DP600 metal sheet, and Ni-Al located at the bottom. Both materials proved their ability to be used as interlayer, however, further details such as optimum ESD operating parameters to deposit the materials, and other possible interlayer material options will be discussed in the next section.

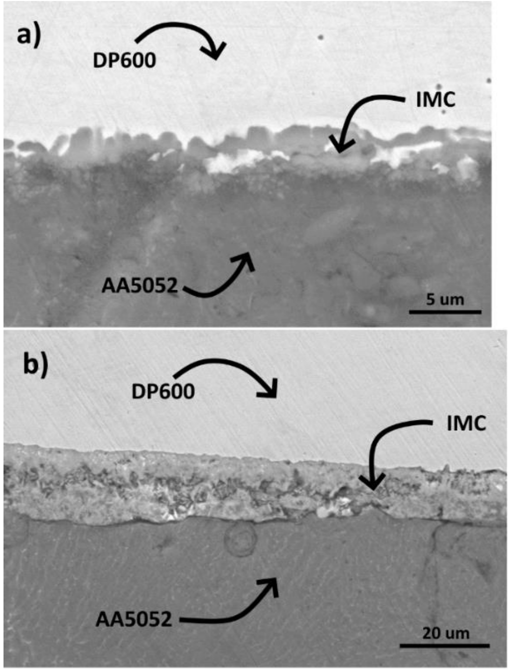

Figure 38 Welded Faying Interface of AA5052 to DP600 with interlayer of a)AA4043; b)IN718

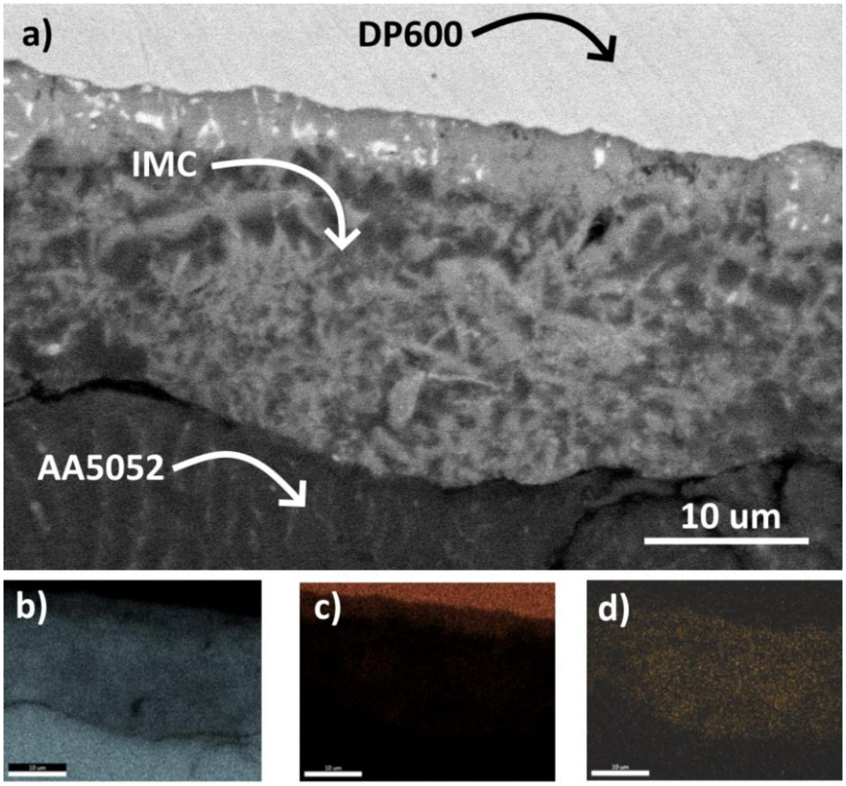

Figure 39 Samples welded with IN718 at a) faying interface and EDX of b) Al, c) Fe, and d) Ni

In this study, four different interlayer materials were selected to investigate their impact on the dissimilar RSW of AA5052 and DP600 steel, which are AA4043, AZ81A, IN625, and Ni99.

AA4043 and AZ81A both have low melting point, when depositing on DP600 steel, this thermal property will allow them to be deposited with enough thickness under shorter time period, thus becomes ideal in manufacturing environment. More importantly, they both have similar material properties as one of the base metals, AA5052, depositing them onto DP600 and then welding with AA5052 will avoid the direct contact between two dissimilar materials.

Unlike the two interlayer materials mentioned above, IN625 has a higher melting point than DP600 steel, and do not share many commonalities with AA5052 but with DP600 instead, which means during the welding process, the dissolution of solid metal will still happen at the solid/liquid interface and form IMCs. However, after depositing IN625 on DP600 steel, the direct contact between AA5052 and DP600 was replaced by that between AA5052 and IN625, it is reasonable to assume that the formation of Al-Fe IMCs will also be replaced by the formation of Al-Ni IMCs. The original aluminum-rich IMCs Al_5Fe_2 and $Al_{13}Fe_4$ are brittle, but the proposed aluminum-rich IMCs Al_3Ni are ductile, which has the potential to improve the mechanical strength by reducing the weak spot caused by brittleness.

4.2 Effect of ESD Operating Parameters on Different Properties of ESD Coating

For the four different interlayer materials mentioned above, multiple sets of operating parameters were chosen as attached in appendix to test how they will affect the properties of the deposited interlayer, mainly focus on the depositing rate and deposition quality.

4.2.1 Interlayer Deposition Rate

In manufacturing operation, deposition rate plays a significant role with respect to budgeting, the faster material can be deposited, the less operational cost will be generated. Deposition rate at different operating parameters were obtained by depositing coatings in 1 cm^2 areas on a GI DP600 sheet, measuring the thickness of coating after cross sectioning, and using the deposition time for each set of parameters to calculate. At least three measurements were taken for each sample to find the coating thickness, with images taken on OM and measurements made using ImageJ software.

The deposition rate for AA4043 is significantly affected by the ESD operating parameters as shown in Figure 40. The fastest deposition rate was obtained at 310 µF, 140 V, and 150 Hz, which is the highest tested energy input level.

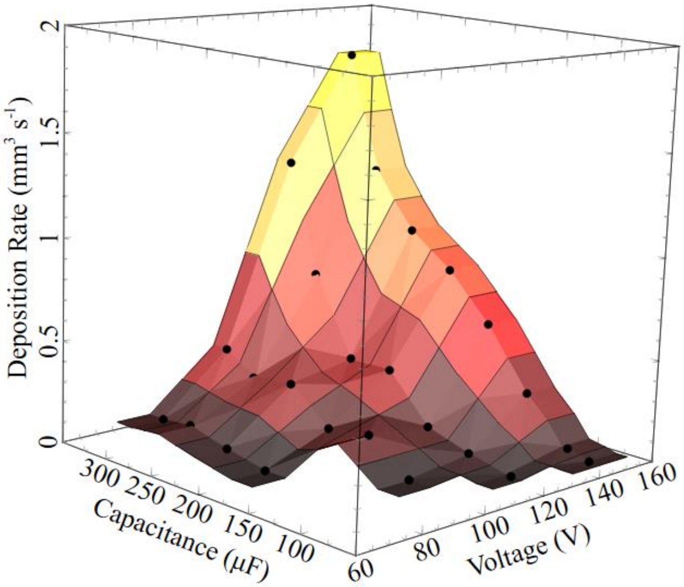

Figure 40 Deposition Rate of AA4043

For AZ81A, it also illustrated a positive trend in deposition rate as the energy level increases as shown in Figure 41. Comparing to AA4043, it even has a larger coefficient between the deposition rate and energy level, which reaches the fastest deposition rate at 250 µF, 140 V, and 150 Hz.

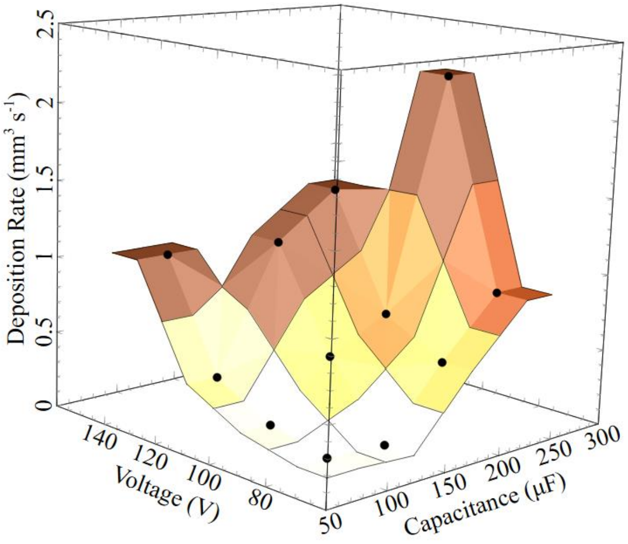

Figure 41 Deposition Rate of AZ81A

For IN625, the deposition rate was significantly lower than other interlayer materials at the same energy input level as shown in Figure 42, this might be caused by the high melting point of Ni. Its fastest deposition rate was obtained at 220 µF, 140 V, and 150 Hz.

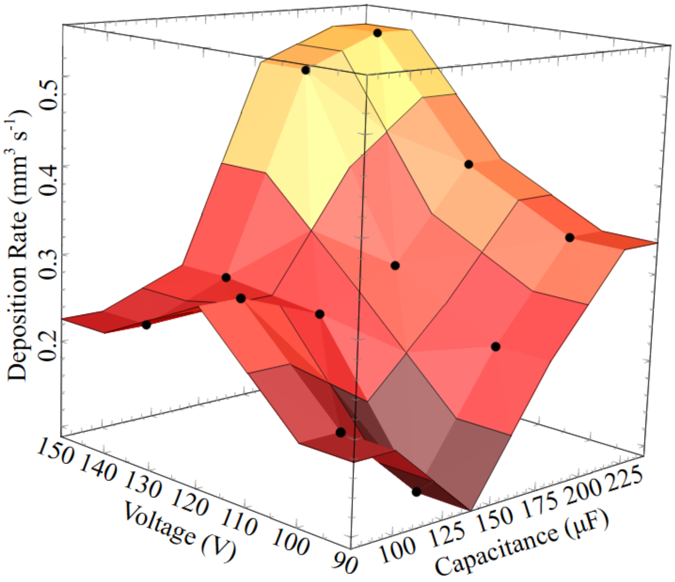

Figure 42 Deposition Rate of IN625

For Ni99, the deposition rate is significantly lower than any other interlayer materials as shown in Figure 43, the maximum deposition rate achieved is under the parameters of 240 μF, 100 V, and 150 Hz. This phenomenon mainly contributes to the high atomic content (larger than 99 %) of Ni, the high melting point of this element causes not enough amount of the electrodes to be liquefied and form the interlayer deposition, which might also cause hot-cracking due to the shrinkage strains.

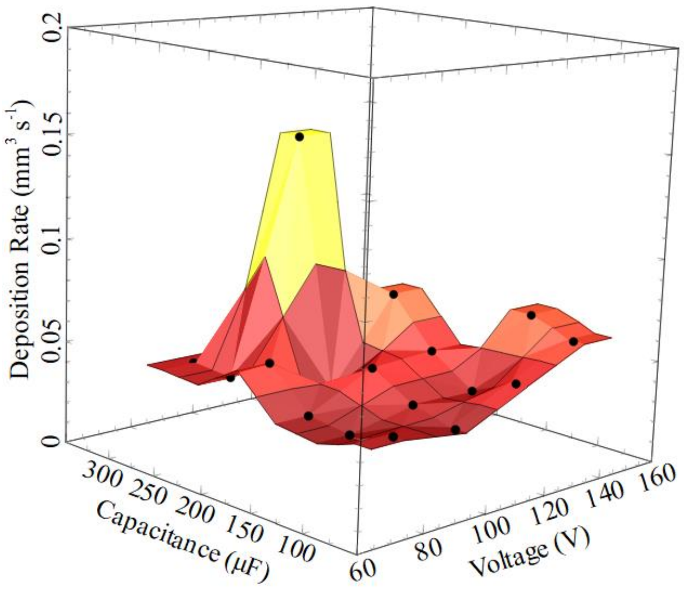

Figure 43 Deposition Rate of Ni99

This trend shown in the deposition rate for all materials can be explained by the fact that as capacitance and voltage of ESD increases, more energy (E) is being stored in a capacitor as shown in Equation 10, which transfers greater amounts of material to the substrate.

Equation 10: Capacitor energy

$$E = \frac{1}{2}CV^2$$

4.2.2 Interlayer Quality and Operating Parameter Selection

Based on the discussion in previous section, interlayer materials AA4043, AZ81A, and IN625 have desirable deposition rate performance, thus will be considered for further selection. Besides of deposition rate, the quality of the interlayer gets deposited is equally important in production. The general objective is to get deposition with consistent coverage through the DP600 steel surface to ensure uniform heat distribution during RSW, as well as less defects (porosity, cracks) and less roughness, and variations in quality requirements might be defined for different materials. In this sub-chapter, the interlayer quality for each material under certain operating conditions will be investigated and combined with deposition rate to be used as important index for ESD process parameter selection.

4.2.2.1. AA4043

As shown in previous section, the fastest deposition rate for AA4043 interlayer was achieved at the highest tested energy level of 310 µF and 140V. It can be seen from Figure 44 that the coating even though has some porosities present, it still forms a uniform distribution with large number of materials deposited. For AA4043, which has similar properties as AA5052 alloy sheet, the important criteria are to establish enough coating in a short time period and act as a good barrier of direct contact between two base metals. This set of operating parameters satisfies both requirements, thus it was chosen to be the deposition parameter for AA4043.

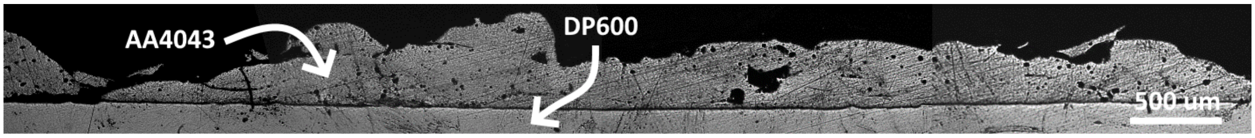

Figure 44 AA4043 deposition at 310 µF, 140 V, 150 Hz

4.2.2.2. AZ81A

When depositing AZ81A interlayer at its highest tested energy level of 250 µF, 140 V, and 150 Hz, even though the deposition rate reaches the maximum, from an operator point of view, the deposition process is too vigorous and uneven accumulation of materials often happens. Thus, a focus was given for parameters with lower energy level and when looking at the deposition quality at both 200 µF, 80 V, 150 Hz and 250 µF, 80 V, 150 Hz as shown in Figure 45a and b respectively, defects exist under both operating parameters, with the fact that their deposition rate is close, the one gives less porosity, 200 µF, 80 V, 150 Hz, was chosen to be the deposition parameters for AZ81A.

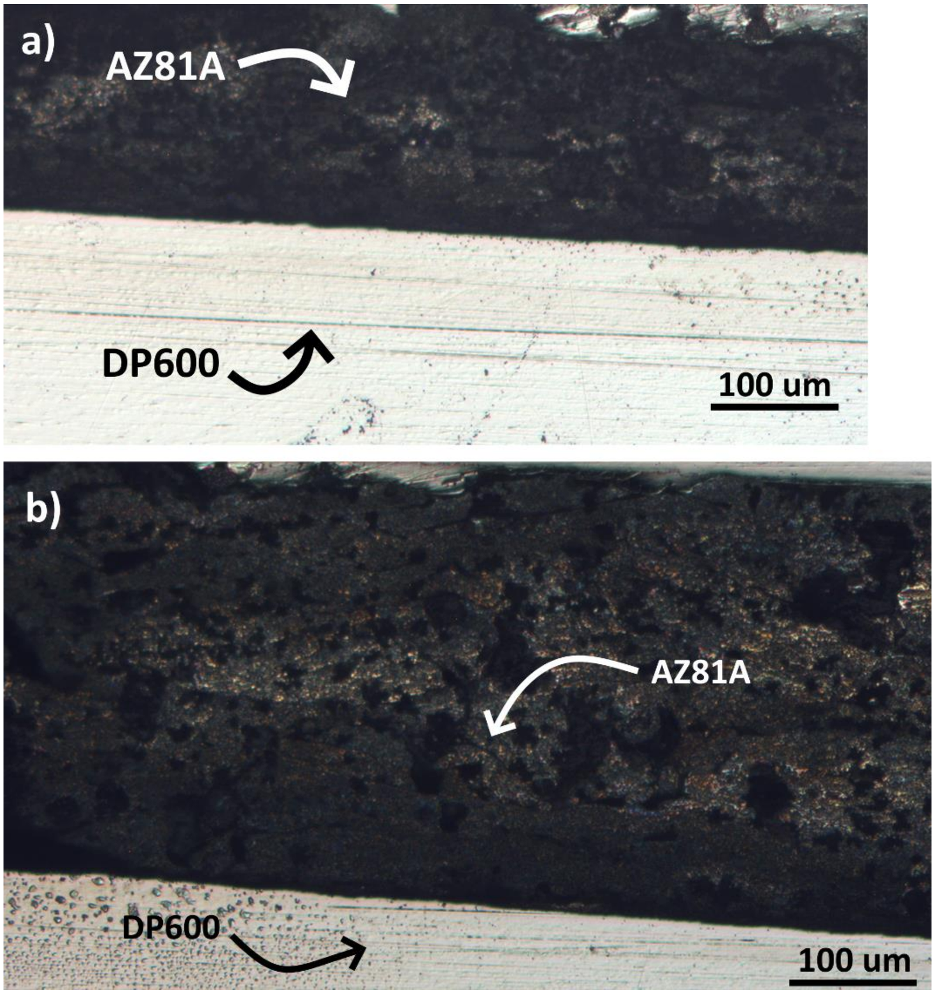

Figure 45 AZ81A deposition at a)200 µF, 80 V, 150 Hz, and b)250 µF, 80 V, 150 Hz

4.2.2.3. IN625

For IN625, the high melting point and low thermal conductivity makes it relatively harder to get electro-spark deposited, thus longer deposition time was applied, and lower energy input was also applied to avoid too much formation of defects. The deposition quality at 100 µF, 100V, 150 Hz and 140 µF, 100V, 150 Hz was observed in Figure 46a and b respectively. The energy level for these two sets of parameters do not have significant difference, however, the one deposited with a little higher energy level shows more consistent coating coverage with similar degree of defects, thus 140 µF, 120V, 150 Hz was chosen to be the operating parameters for IN625.

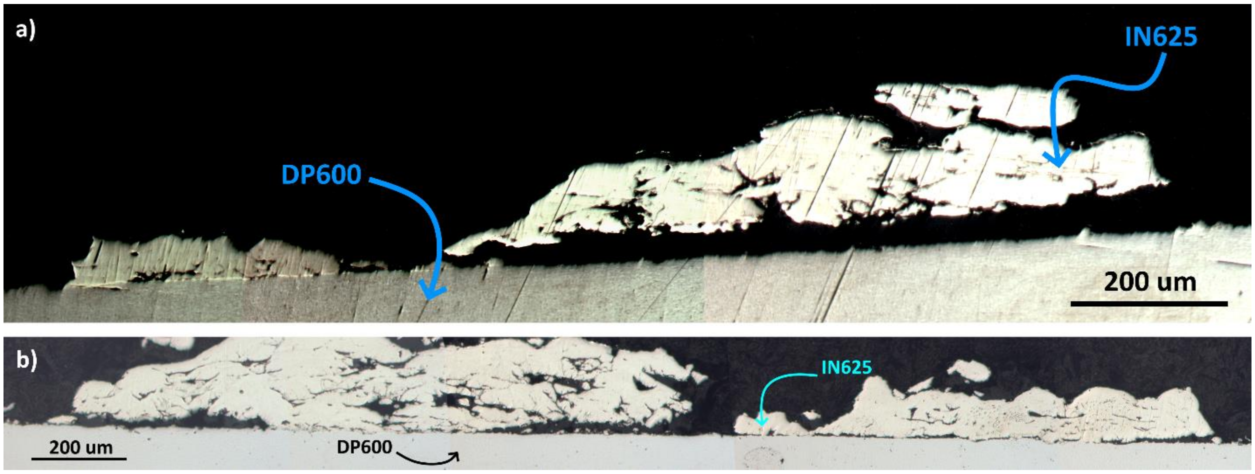

Figure 46 IN625 Deposition Quality at a)100 µF, 100V, 150 Hz; and b) 140 µF, 120V, 150 Hz

4.3 Pre-examination of IMC formation during ESD Process

Even though the fact that ESD process can generate high pulse energy with short duration will not significantly change the nature of base metal, it is still possible that brittle IMC could be formed during the ESD process, so further examination at the interlayer/DP600 interface will needed to be done.

For samples deposited with AA4043, from the SEM image shown in Figure 47, a uniform thin layer of IMC (approximately 5 µm) is formed at the interface between the base metal and the coating. This agrees with the previous finding in the preliminary study, and how this formation of IMCs will impact the mechanical performance will be investigated in the Chapter 5.

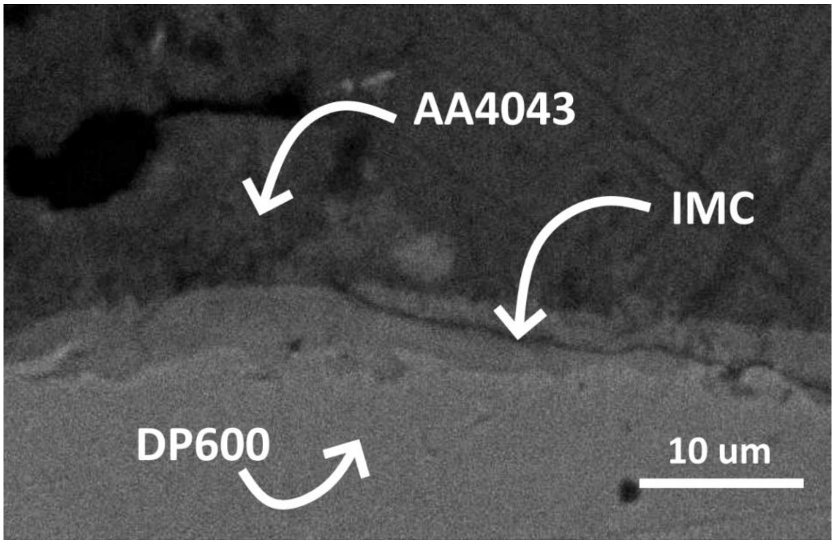

Figure 47 Interface between AA4043 interlayer and DP600 before welding

Even though the thickness of those IMCs was thinner than direct welding between AA5052 and DP600, the formation of brittle Fe-Al IMCs during ESD still leaves a questionable turnout on the application of AA4043 in the improvement of weld assembly, it is always ideal to gain a IMC-free in the early ESD stage.

Looking at the interface between AZ81A/IN625 interlayer and the DP600 metal sheet after ESD shown in Figure 48a and b respectively, they are both possible without the formation of an intermetallic, which means further improvements could be expected.

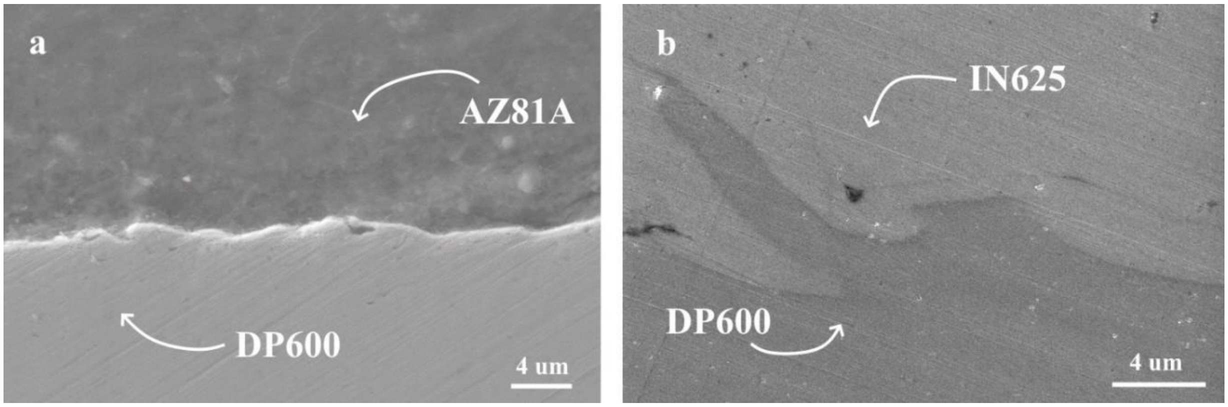

Figure 48 Interface observation before RSW between DP600 and a)AZ81A, and b)IN625

4.4 Summary

After investigation in this section, it is known that the interlayer deposition quality and deposition rate both have close relationship with the amount of energy input during ESD process. Under careful observation, 310 µF, 140 V, 150 Hz was chosen for AA4043, 200 µF, 80 V, 150 Hz was chosen for AZ81A, and 140 µF, 120 V, 150 Hz was chosen for IN625 for further experiments involving RSW of Al to steel.

Chapter 5 Effect of Different Interlayer Materials on the Performance of Dissimilar RSW of Al to Steel

5.1 Experiments with Al Interlayer

5.1.1 Mechanical Testing

As illustrated in Figure 49, the mechanical strength after the application of AA4043 interlayer is improved under all tested current conditions, with a minimum average increase of 30%. The lowest current of 9 kA is insufficient to form a weld in the samples without an interlayer, attributed to insufficient heat generation for both melting of the zinc coating and melting of the aluminum. This finding confirms previous studies in which welding was attempted but not successful at 9 kA on zinc coated steel[62]. With the application of an AA4043 interlayer, 9 kA is sufficient for some joining to occur and an average failure load above 5 kN is obtained with a weld current as low as 11 kA. Without the use of an interlayer, the failure load remains consistently lower, reaching an average of 4.3 kN at a weld current of 15 kA. Interfacial failure occurs in all samples regardless of the weld current or whether an interlayer was used. It is very likely that the difference in strength is attributed to differences in the thickness of the intermetallic that forms during welding, which will be investigated and discussed further in the next section.

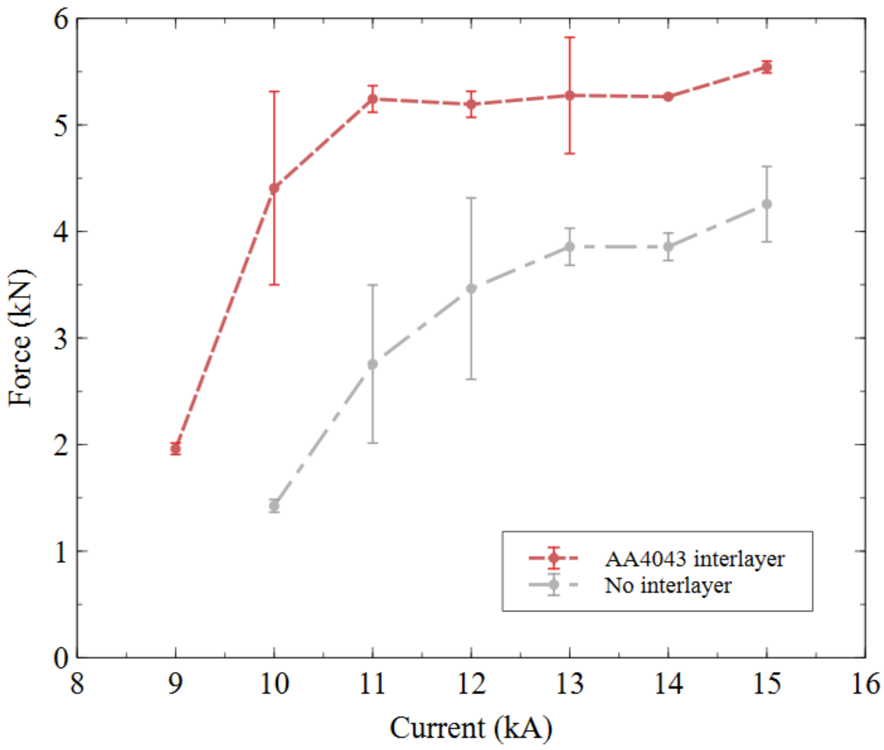

Figure 49 Comparison between the mechanical strength of samples welded with AA4043 interlayer and without interlayer

5.1.2 Microstructural Analysis

The aluminum alloy to steel interface has a noticeably thinner iron aluminide intermetallic when resistance spot welded with the AA4043 interlayer. At the highest welding current of 15 kA, a sub-micrometer thick intermetallic Figure 50a is present that matches the intermetallic thickness formed during the deposition of the interlayer Figure 50b. This suggests that growth of this intermetallic during resistance spot welding is limited. A comparison to the intermetallic that forms after welding without an interlayer is shown in Figure 50c, which ranges from 1 to 9 µm thick. Due to the larger thickness, a more reliable EDX measure of this intermetallic can be obtained, which indicates an average composition of approximately 63 wt% Al and 37 wt% Fe.

Based on the EDX linescans indicated by the dashed arrows in Figure 50a, the AA4043 interlayer fully melts during the resistance welding process. Although AA4043 contains silicon – which can be detected in the interlayer prior to RSW (Figure 50b) – none is detected in the aluminum adjacent to the intermetallic after RSW (Figure 50a). Instead, EDX reveals magnesium (Figure 50a) which can be attributed to AA5052. Therefore, the following is proposed to explain the difference in iron aluminide intermetallic thickness between sheets with and without an interlayer: heat generated during welding due to the contact resistance between AA5052 and AA4043 is firstly used to melt the contact asperities between the two interfaces and then used to melt the AA4043 interlayer. These two energy sinks act as a barrier to the energy required for iron aluminide intermetallic growth at the aluminum alloy to steel interface. Instead, the intermetallic identified at that interface is unchanged from that formed during ESD interlayer application, as can be seen by comparing Figure 50a and Figure 50b.

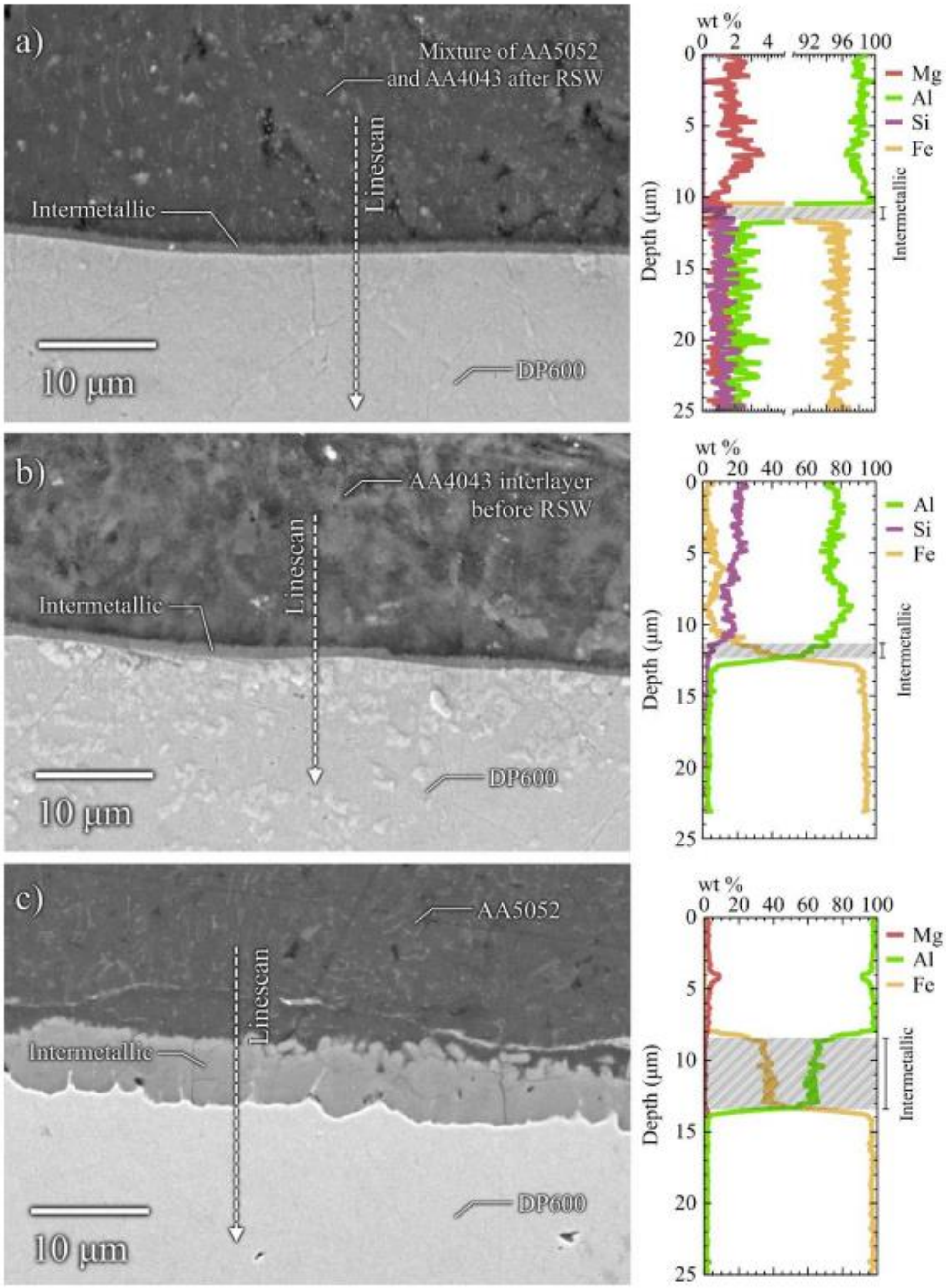

Figure 50 SEM images of a) AA5052 welded to AA4043 coated GI DP600 at 15 kA b) ESD of AA4043 on GI DP600 before RSW and c) AA5052 welded to GI DP600 without an interlayer at 15 kA. Results of the EDX linescan as indicated in each image are shown adjacent to the image.

Interestingly, when looking at the welding current of 13 kA, the amount of iron aluminide intermetallic formed at aluminum alloy to steel interface for both samples welded with AA4043 interlayer and without interlayer does not have significant difference either as shown in Figure 51. However, it is still evident that the mechanical performance has been improved for both previously 15 kA and 13 kA, which means except for the depression of IMC growth, there existing other positive impact caused by the application of AA4043 interlayer.

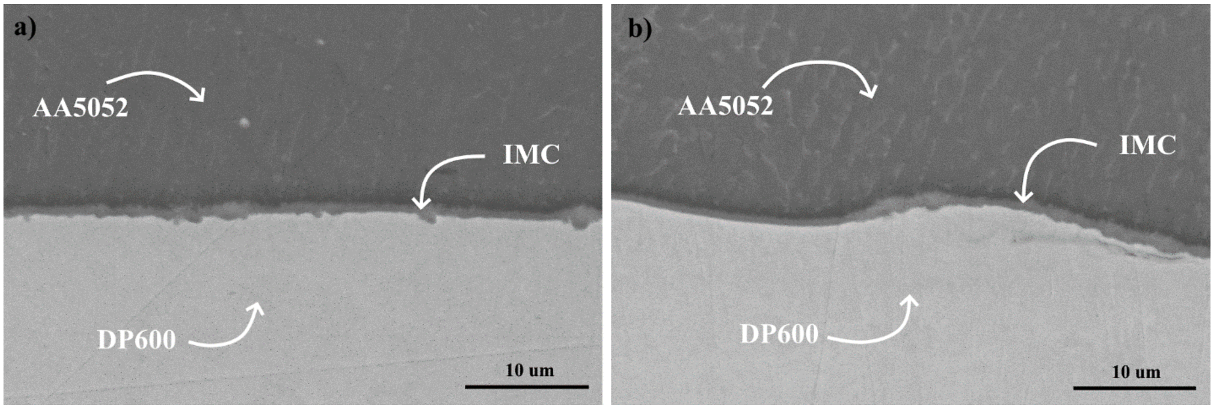

Figure 51 IMC formation near the center of weld for samples welded a)with AA4043 and b) without AA4043

Moving along the faying surface of the samples welded without interlayer, it is noticed that there is a giant cavity with max diameter of approximately 340 µm on the AA5052 side, this cavity has not been observed in any of the samples made with AA4043 interlayer. During mechanical testing, this cavity becomes the weak spot and thus deteriorates the performance of weld. Investigating the formation mechanism of this cavity will understand how the application of AA4043 interlayer helps eliminate this defect development.

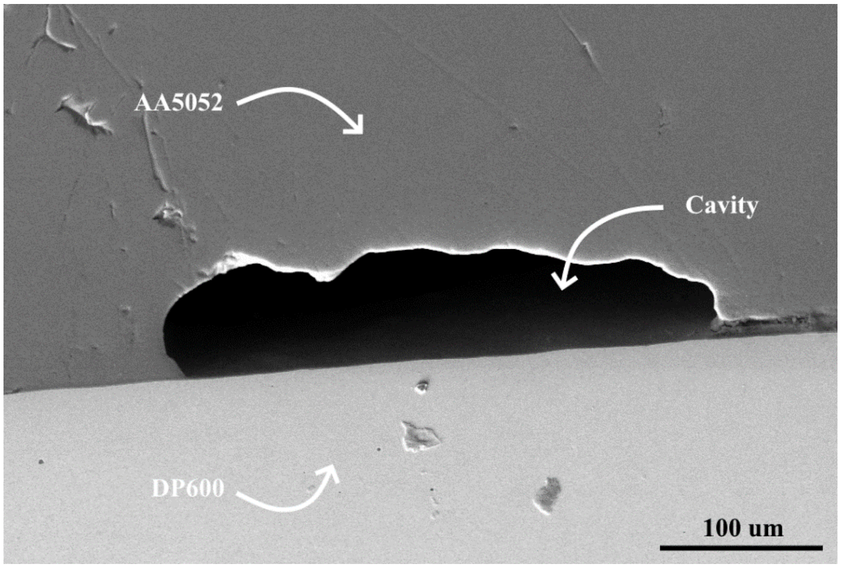

Figure 52 Samples welded without interlayer

The elemental analysis for the edge area of the welded sample (Figure 53a) is shown in Figure 53b, it indicates that the material accumulated at the gap between two deformed metal sheets is mainly Zn. This is because GI DP600 metal sheet was originally covered by a thin layer of Zn coating to prevent corrosion, and for those samples welded without interlayer, zinc remains on the DP600 sheet during resistance welding. As heat is generated at the faying interface the following physical changes occurs zinc firstly got melted at around 419 °C, followed by the melting of AA5052 at 607 °C, and lastly the zinc boiling happens at 907 °C. Heat generated during welding is first used to melt the zinc coating, which decreases the contact resistance and reduces the amount of additional heat generated. This limits the amount of heat available to melt the AA5052, which limits the size of the weld nugget. To overcome this issue, higher welding currents must be used. However, too much heat generation results in boiling of the zinc coating. This leads to the formation of gas porosities that remain trapped within the AA5052 sheet after welding, similar phenomenon was also observed by Dong et al. as shown in Figure 54. However, even though the insertion of filler materials effectively hinders the IMC growth, it could not eliminate the pores produced by Zn vaporization. In the contrast, for those samples welded with ESD interlayers, Zn already gets evaporated by the heat input from ESD process.

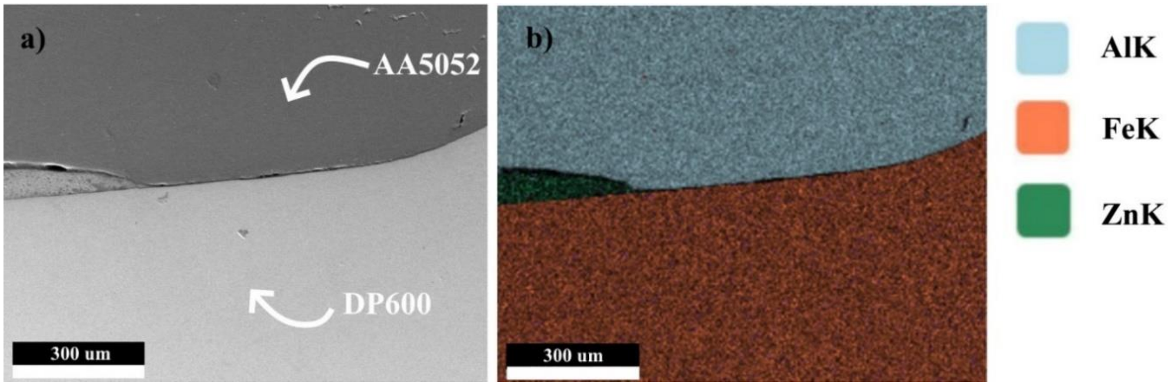

Figure 53 a) edge of the welded sample without interlayer b)elemental analysis of this area

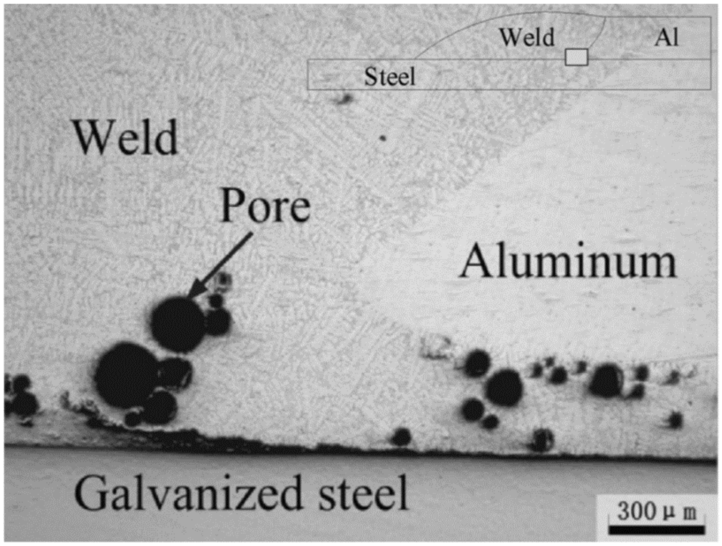

Figure 54 Gas porosity formation during the RSW of Al and GI steel with insertion of filler material

The presence of Zn coating on DP600 even though keeps the metal sheet in good condition, but also at the mean time, deteriorates the mechanical performance after welding by forming interface defects. A new approach is then proposed to improve the weld quality, which is to eliminate the Zn coating prior to welding process and observe how that will affect the mechanical performance. NaOH solution was used to remove the Zn coating without changing the nature of DP600 base metal, and no interlayer was used in this test to solely discover the effect of Zn coating on mechanical strength of weld.

The mechanical performance of samples welded with Zn coating removed outstands that of samples welded with no interlayer but Zn coating present under all tested current as shown in Figure 55. Even though the improvement is not as significant as the welds with the application of AA4043 interlayer, still on an industrial production point of view, this removal of Zn coating method could be more time-saving, cost-effective since no innovative equipment is needed, and better adaptability is achieved under various manufacturing environment.

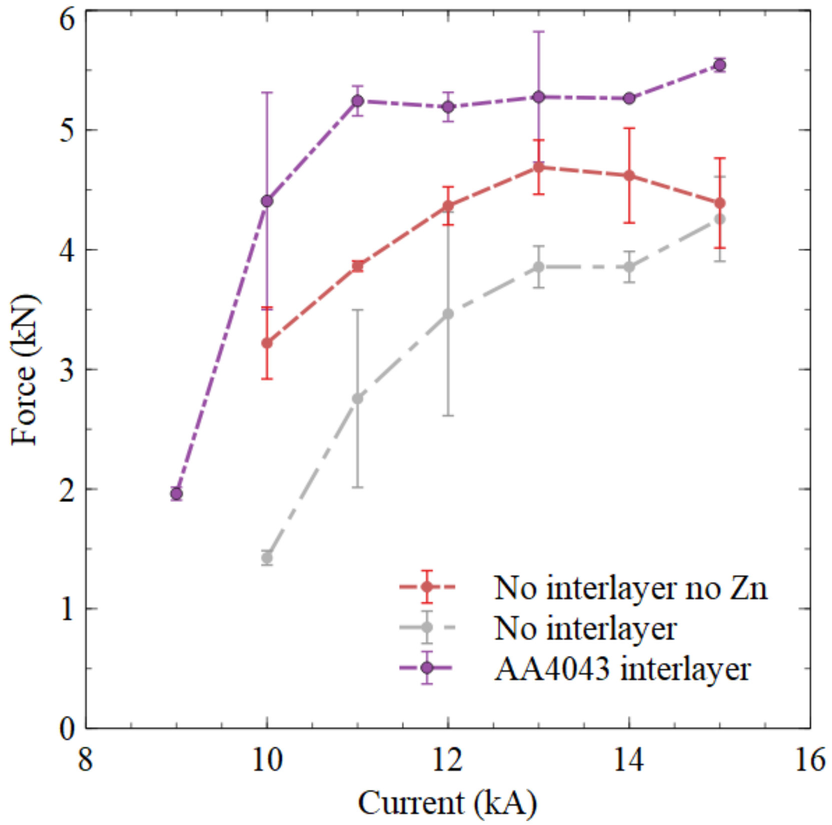

Figure 55 Comparison between the mechanical strength of samples welded with no interlayer and Zn coating removed, with AA4043 interlayer, and without interlayer

5.2 Experiments with Ni Interlayer

5.2.1 Mechanical Testing

For an IN625 interlayer, successful welds were created at 6 kA (Figure 56) while melting in the interlayer was predicted at 3.5 kA (Figure 36). Since the melting temperature of the Ni interlayer is significantly higher than that of the AA5052 sheet, the AA5052 is expected to melt prior to the interlayer. As the aluminum alloy melts and is pushed to the periphery of the weld, it cools the faying interface and requires that higher currents be used to generate sufficient heat for welding to occur. This mechanism is not accounted for using a purely thermal model.

Comparing to samples welded with AA4043 interlayer, the minimum required current to initiate a solid weld was decreased by 3 kA, this might be caused by the fact that the heat generated was used solely for the melting of AA5052 metal sheet, additional heat is no longer required to melt the interlayer. However, it does not offer much significant improvement in load-bearing capacity when compared to the interlayer-free samples due to the reasons explained in the next section.

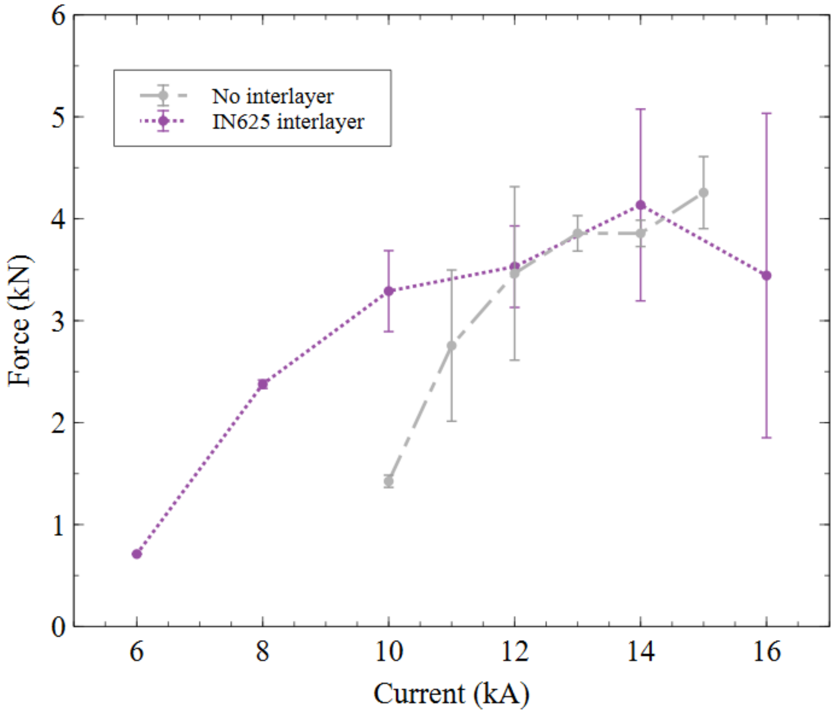

Figure 56 Comparison between the mechanical strength of samples welded with IN625 interlayer and without interlayer

5.2.2 Microstructural Analysis

The failure mechanism for samples welded with IN625 interlayer can be observed from Figure 57. The interlayer remains above critical value after the RSW process and a Ni-Al intermetallic forms along the IN625/AA5052 interface. Fracture during lap shear loading occurs along this NiAl intermetallic. The brittle nature of Ni-Al IMC and the failure location observed in this sample explained why the mechanical performance after the application of IN625 interlayer has not been improved much.

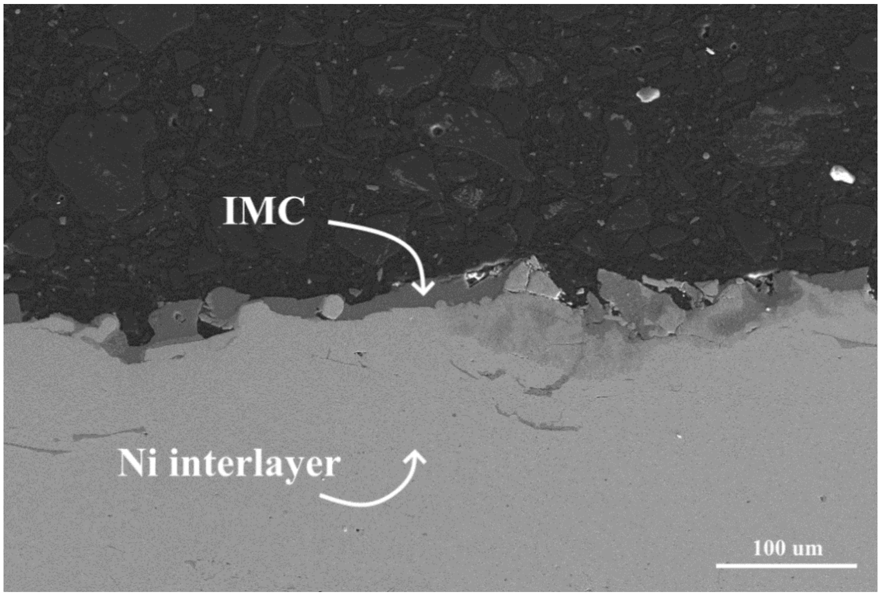

Figure 57 Fracture Location for Samples Welded with IN625

5.3 Experiments with Mg Interlayer

5.3.1 Mechanical Testing

Welds created with an AZ81A interlayer require higher currents than samples with IN625 or AA4043 interlayers, and a similar effect was observed for the AZ81A interlayer, with successful welds created at 11 kA (Figure 58) while melting in the interlayer was predicted at 5.5 kA (Figure 36). The maximum loading observed using an AZ81A interlayer is significantly higher than that of the interlayer-free joints, IN625, and AA4043 interlayer samples, showing increases in the peak loading of 84%, 90%, and 42%, respectively.

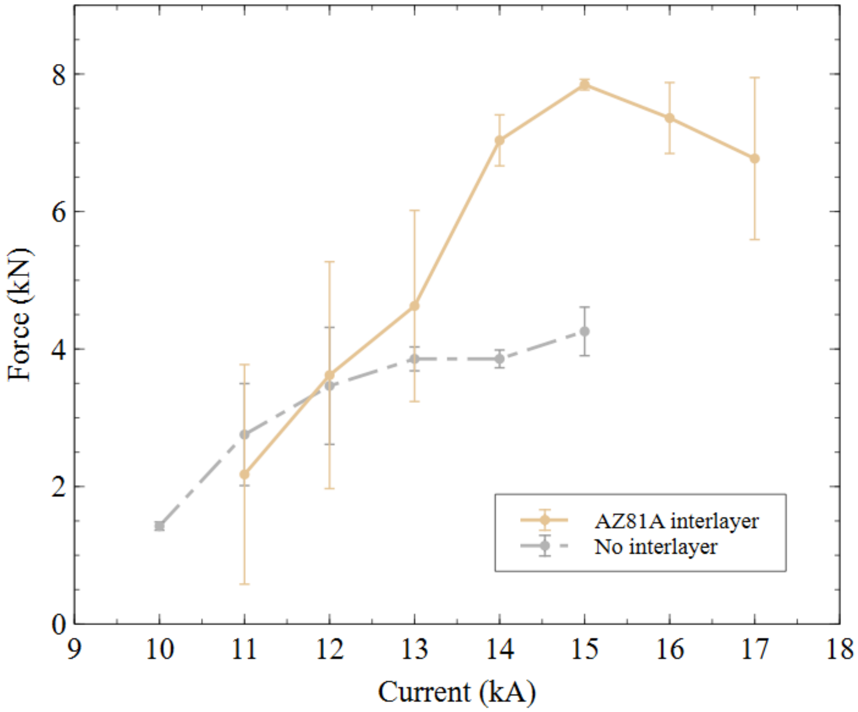

Figure 58 Comparison between the mechanical strength of samples welded with AZ81A interlayer and without interlayer

5.3.2 Microstructural Analysis

In this case, the AZ81A interlayer has a lower melting point, and should melt prior to the AA5052. As the AZ81A melts and is pushed to the weld periphery, it also cools the fraying interface. At the conclusion of the welding process, no magnesium beyond what is expected in AA5052 is detected along the interface where the AZ81A was located, as shown in Figure 59. The use of a magnesium alloy as an interlayer, rather than an aluminum alloy such as AA4043, is beneficial for two reasons. No brittle intermetallic forms during the initial interlayer deposition, and the fusion zone in the AA5052 sheet can grow without concurrent FeAl intermetallic growth. Intermetallic growth only begins once the magnesium has been squeezed out of the weld area and the aluminum contacts the steel, at which point a large fusion can form.

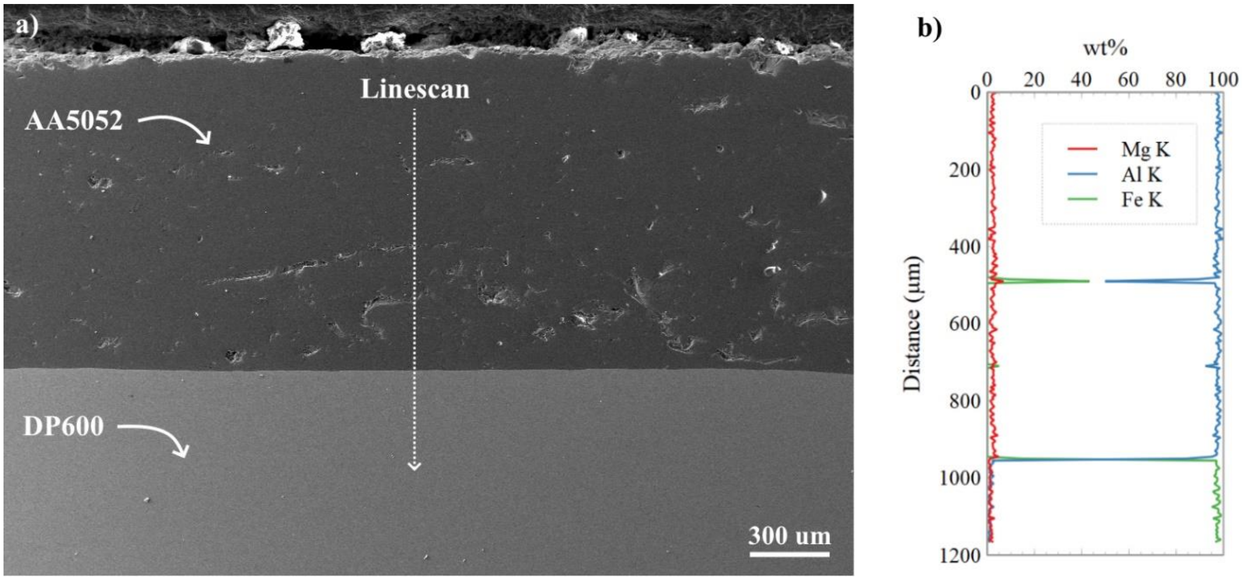

Figure 59 a) Weld created with an AZ81A interlayer and b) linescan corresponding to the dotted arrow included in a).

In the case of an AZ81A interlayer, the interlayer is melted and pushed out of the weld region such that an Fe-Al intermetallic forms between the AA5052 sheet and DP600. However, unlike welds performed with no interlayer or with an AA4043 interlayer which were previously reported to fracture along the brittle Fe-Al intermetallic, welds formed with an AZ81A interlayer do not fail along the intermetallic. The fracture surface cross-section in Figure 60 shows that fracture occurs through the AA5052 and the intermetallic (IMC) remains unbroken.

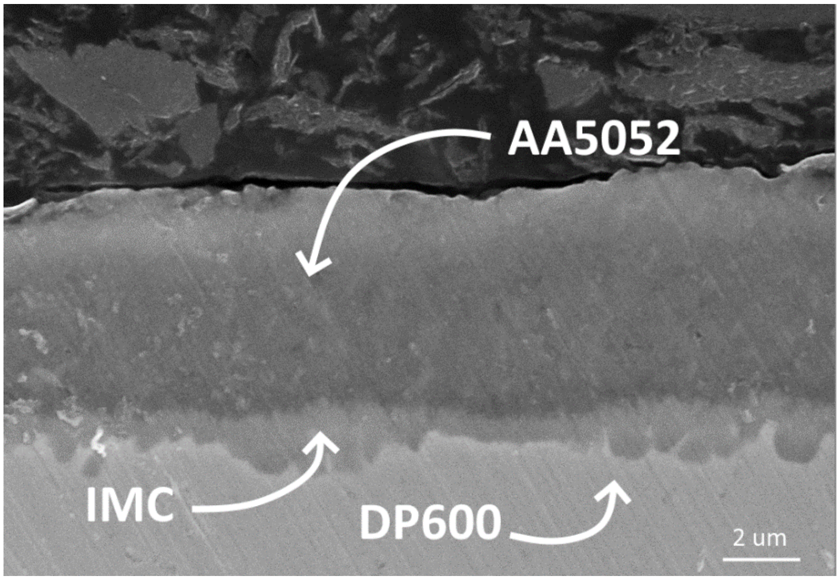

Figure 60 Failure location for AZ81A interlayer samples after spot welding and tensile lap shear testing

5.3.3 Welding Current Effect

The fusion zone size – identified by the solidification microstructure after etching (Figure 61c) – in joints created with an AZ81A interlayer and welded with a current of 13 kA is minimal, although it increases significantly when welding with a current of 14 kA (Figure 61a vs. Figure 61b). This also corresponds to the significant jump in strength between AZ81A interlayer samples welded with 13 kA and those welded with 14 kA. Peel testing was also performed for samples at these two currents to measure the nugget size. The nugget size for the sample welded with 13 kA (Figure 62a) is much smaller than those welded with 14 kA (Figure 62b), which further explains the significant increase in strength.

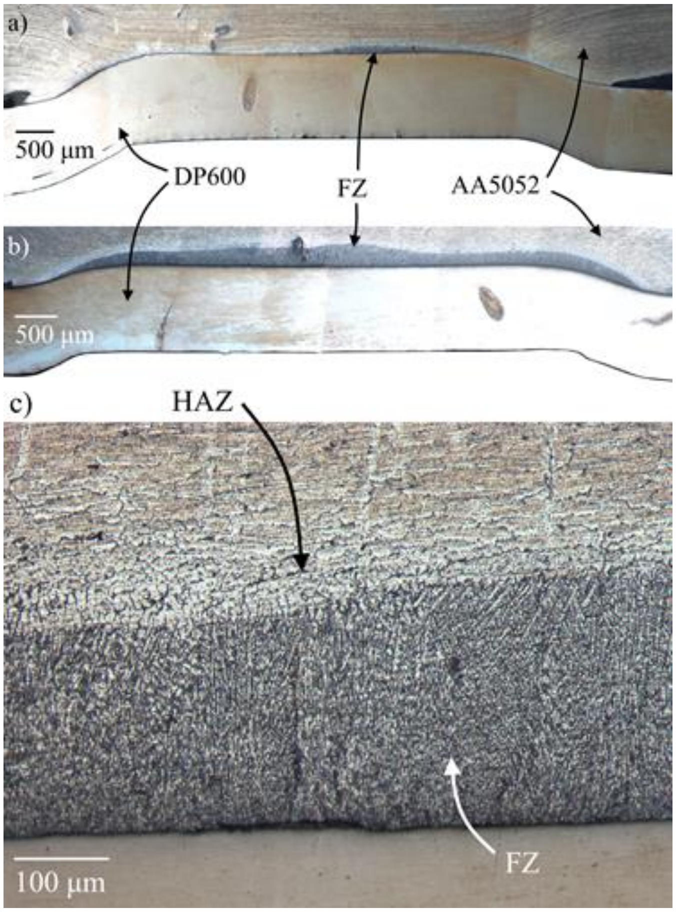

Figure 61 Microstructure of AZ81A coated sample at (a) 13 kA, (b) 14 kA, and (c) annotated at 10x magnification at 14 kA

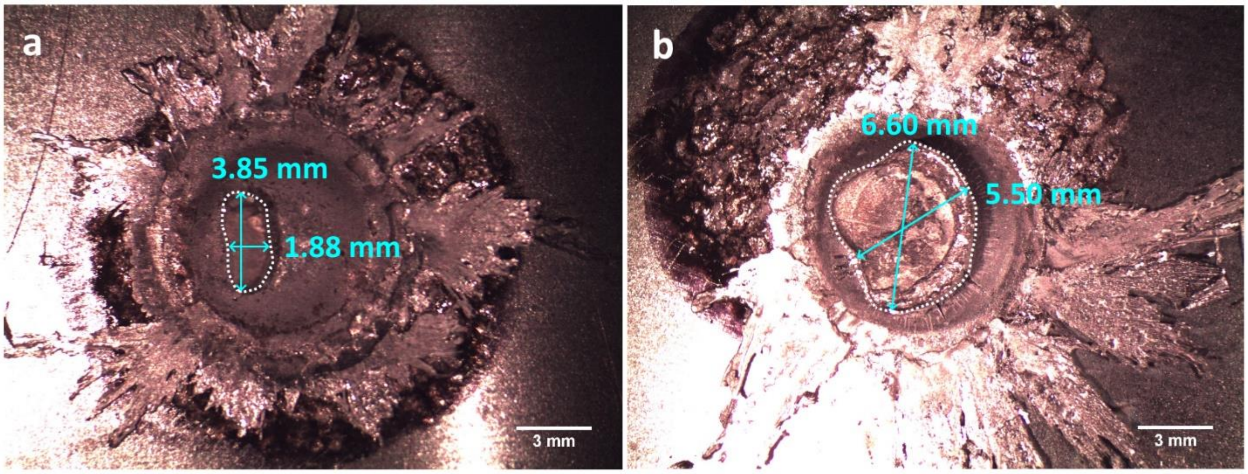

Figure 62 Peel test nugget sizes for samples welded with AZ81A interlayer at a) 13 kA, b) 14 kA

Unlike during peel testing, all AZ81A interlayer samples experienced total dome failure [64] in the AA5052 during lap shear loading except for some samples welded at 17 kA, which experienced a partial dome failure (Figure 63) due to thinning of the AA5052 sheet.

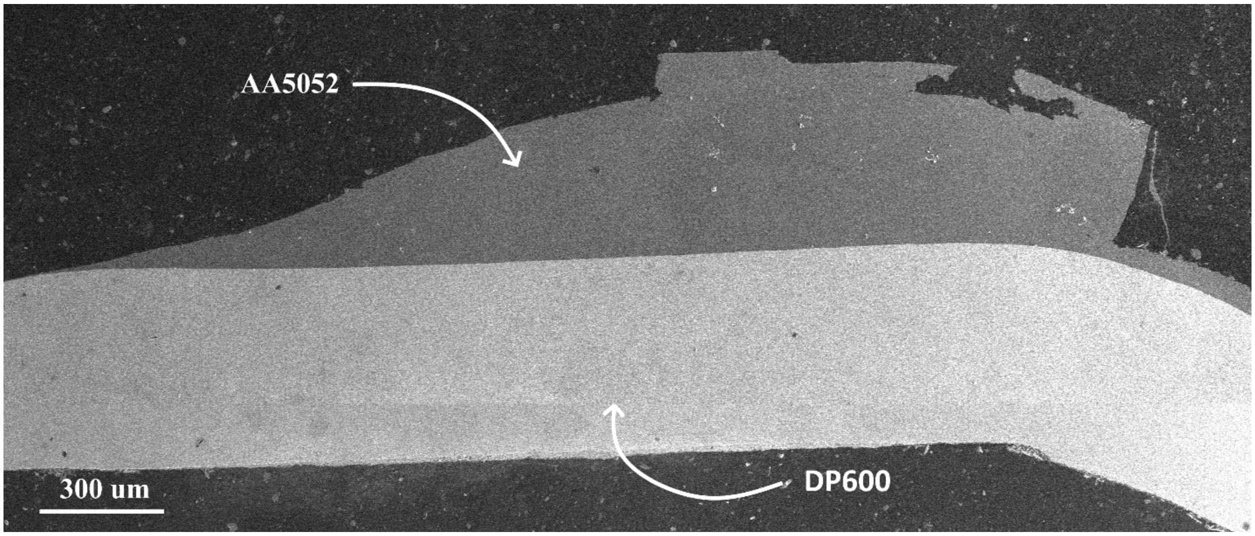

Figure 63 Mix of HAZ failure and pull-out failure in sample with AZ81A welded at 17 kA

5.4 Shielding Gas

In reality, especially within the manufacturing industry, it is very economic unfriendly to apply coatings using ESD with the presence of Argon gas or any inert gas to avoid oxidation from happening, becasue it often requires large amount of constant Argon gas flow or the process being operated in a sealing environment as shown in Figure 64. If the interlayer can be produced under the absence of inert gas, and still improves the mechanical performance of the weld, then it will be a significant milestone regarding of the manufacturing budgeting.

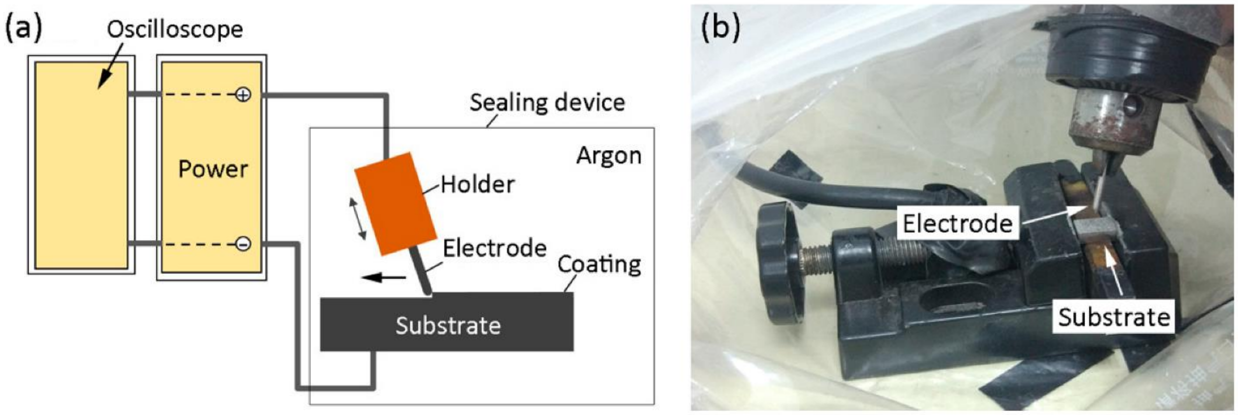

Figure 64 a) Schematic illustration of ESD done in sealed environment, b) assembly of sealed ESD process environment[65]

AZ81A interlayer was chosen to be deposited under the condition where argon gas is not turned on during ESD, and the reason for this selection is that from previous tests, samples welded with AZ81A using the current above 13 kA gives the best mechanical performance so far. Those DP600 metal sheets coated with AZ81A without shielding gas were then welded with AA5052 under currents: 13, 14, and 15 kA and finally brought to tensile testing to gain the mechanical performance data as shown in Figure 65.

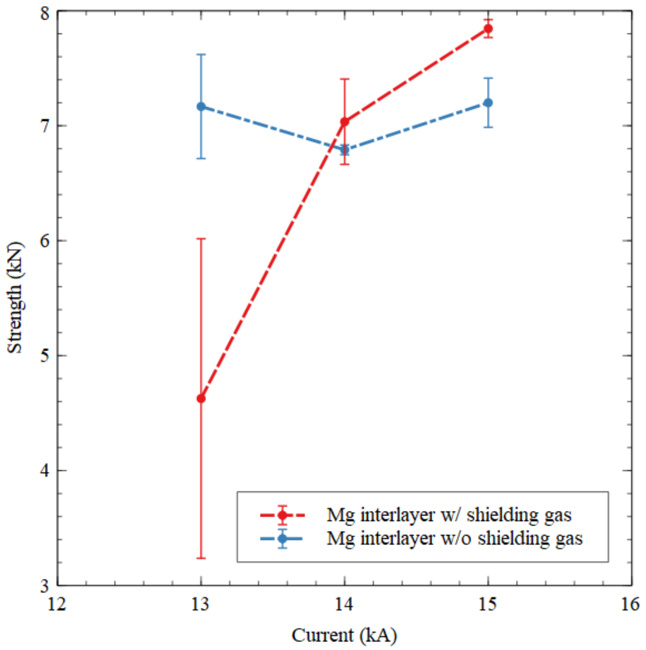

Figure 65 Comparison of mechanical performance for samples welded with interlayer made a) with shielding gas; b) without shielding gas

Surprisingly, the samples welded with AZ81A interlayer without shielding gas does not only maintain the high mechanical strength under 14 and 15 kA, but it also eliminates the “strength gap” observed in samples welded with AZ81A interlayer with shielding gas between 13 and 14 kA by increasing the strength at 13 kA by almost 55%.

Similar as previous section, this improvement in mechanical strength under 13 kA could also be explained by the fusion zone size. The fusion zone size for sample welded with AZ81A interlayer without shielding gas at 13 kA (Figure 66a) is much larger than that with shielding gas under 13 kA (Figure 61a), and when comparing to samples without shielding gas at 14 kA (Figure 66b), they both developed solid fusion zone, and thus both have good mechanical performance.

Figure 66 Microstructure of AZ81A coated sample at (a) 13 kA, (b) 14 kA without shielding gas

5.5 Interlayer Thickness

Except for the application of inert gas, the ESD deposition time is also a key factor in controlling the manufacturing cost. From the previous section, it is found that the AZ81A coating gets melted and mixed with the AA5052 alloy during the welding process, which means based on this mechanism, the thickness should have a critical value to absorb enough heat to produce a large fusion zone without excessive IMC growth. In this case, a study is designed to study if less deposition time resulting in thinner interlayer thickness could ensure similar mechanical performance, with the result is shown in Figure 67. Surprisingly, with the reduction of 50% deposition time, the mechanical strength is kept at the same level, even though with a slightly larger standard deviation, it still gives confidence in the research area of further decreasing the deposition time to achieve better economic efficiency.

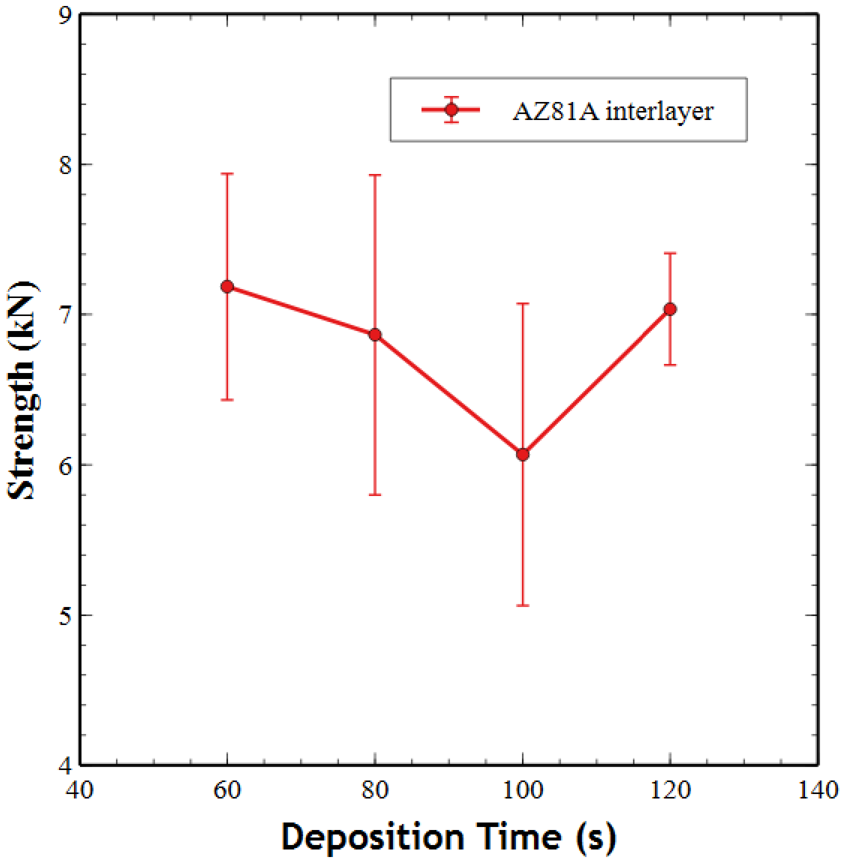

Figure 67 Comparison of tensile shear strength for samples welded with AZ81A interlayer under different deposition time

5.6 Summary

The application of three different interlayer, AA4043, AZ81A, IN625 all show improvement in the tensile-lap shear strength of welded samples.

Aluminum alloy interlayer (AA4043) improves the strength by 30%, for which the failure mode is interfacial failure. It improves the strength by eliminating the Zn coating on DP600 and prevents the formation of gas porosity caused by Zn vaporization.

Magnesium alloy interlayer (AZ81A) improves the strength by 84%, for which the failure happens through AA5052 metal sheet and IMC remains unbroken. The improvement is` made due to the elimination of brittle Fe-Al IMC and the absorption of heat by the melting of AZ81A interlayer. A significant increase in strength is observed for welded sample under 14 kA comparing to that under 13 kA because of the increase in weld nugget size.Nickel alloy interlayer (IN625) does not show significant improvement in the strength, and the failure location is along the NiAl IMC which has a brittle nature.

Most of the samples failed with interfacial failure except for one sample welded with AZ81A interlayer under 17 kA, which has been observed with a pull-out failure mode.

Experiments also showed that for samples welded with AZ81A interlayer, when welding samples with interlayer applied without shielding gas during ESD process, actually gives better mechanical performance for samples welded with AZ81A interlayer deposited under shielding gas for welding current between 13 to 15 kA.

Results also illustrated that for the application of AZ81A interlayer, when reducing the deposition time from 120s to 60s, under the assumption that the deposition rate is consistent through the whole deposition process, with half magnitude of the interlayer thickness, similar mechanical performance can still be achieved.

Chapter 6 Conclusions and Recommendations

This research aims to understand the ESD process, and how the operating parameters could influence the deposition's properties such as deposition quality and deposition rate. With the understanding of ESD process, proper interlayer materials and ESD parameters were selected to apply interlayer in the dissimilar RSW of Al alloy to steel to optimize the weld mechanical performance. As such, the conclusions of this thesis are presented in the following sections, followed by future work recommendations arising from this research.

6.1. Conclusions

The criterion for selecting the ESD operating parameters is to ensure the deposited coating will have less defects and a uniform distribution. 310 µF, 140 V, 150 Hz was chosen for AA4043, 200 µF, 80 V, 150 Hz was chosen for AZ81A, and 140 µF, 120 V, 150 Hz was chosen for IN625 interlayer.

By applying AA4043 and AZ81A alloy interlayers prior to the RSW process, the tensile lap shear strength of the dissimilar welded samples were improved by 30% and 84% respectively. The better performance shown in Mg alloy (AZ81A) interlayer application is because of the melting of the interlayer during the welding process, which acts as a heat absorption sink, and thus ensured larger heat input to generate larger nugget size without producing brittle Fe-Al IMCs. No significant improvement was observed with the application of IN625 interlayer, and almost all welded samples with interlayer application has an interfacial failure mode, except for one sample welded with AZ81A interlayer at 17 kA. However, no matter which interlayer material was used, the ESD process can always eliminate the Zn coating on DP600, which prevents the formation of gas porosity, thus resulting in better mechanical performance.

When using AZ81A as an interlayer deposited without shielding gas, the welded sample tensile lap shear strength does not have significant decrease when comparing to samples welded with interlayer deposited with shielding gas under 14 and 15 kA, and under 13 kA the tensile lap shear strength is even improved. The effect of thickness using this interlayer was also investigated by alternating the deposition time. When reducing the AZ81A interlayer thickness to 50%, the tensile lap shear strength of the welded sample even has a minor increase of 0.2 kN.

6.2. Recommendations

Experiments showed that when applying AZ81A interlayer using ESD process, the presence of shielding gas could be opted out, this will not only extend the feasibility of the ESD process but also save a massive amount of operating cost. Further investigation could be done for more variety of interlayer options.

Experiments have also showed that when applying AZ81A interlayer, different thickness of the interlayer could result in similar mechanical performance under certain current input, study could be extended to wider current range and other interlayer options.

In this study, only the aluminum alloy, magnesium alloy, and nickel alloy interlayer materials were investigated, some other materials could also be studied with ESD process and optimizing the ESD and RSW parameters accordingly. High entropy alloy (HEA) is one of the option, its application as an interlayer in the dissimilar RSW of 6061-T6 aluminum alloy to St-12 carbon steel has been proved by Azhari-Saray et al., they've shown that after the application of HEA Al0·5FeCoCrNi the type of IMC is changed from Fe-Al to a more complex form and the crack formation through IMC is prevented[66]. Zinc can also be considered as a possible alternative material, Arghavani et al. have shown that during RSW of Al-5052, St-12 (DC 01) to low carbon galvanized, Zn interlayer helps improve the mechanical performance of welded samples, similar to AZ81A interlayer, the melting of Zn interlayer also effectively hinders the formation of IMC[62].

From results shown in Chapter 5, a minor change in the welding current could also have a significant change in the weld nugget size and mechanical strength, study could also be done to further optimize the RSW operating parameters for different interlayer options.

Reference

1. Cole GS, Sherman AM. Light weight materials for automotive applications. *Mater Charact*. 1995;35(1):3-9. doi:10.1016/1044-5803(95)00063-1

2. Mathers G. *The Welding of Aluminium and Its Alloys*. Woodhead Publishing; 2002.

3. Mohler JB (James B. *Electroplating and Related Processes*. New York: Chemical Pub. Co.; 1969.

4. Johnson RN. Alternative Coatings for Wear and Corrosion: The Electrospark Deposition Process. *Proc AESF/EPA Conf Environ Excell*. 2002:38-47.

5. Kuroda S, Kawakita J, Watanabe M, Katanoda H. Warm spraying-a novel coating process based on high-velocity impact of solid particles. *Sci Technol Adv Mater*. 2008;9(3):33002.

6. What is electrospark deposition (ESD)? - TWI. https://www.twi-global.com/technical-knowledge/faqs/faq-what-is-electrospark-deposition-esd. Accessed July 11, 2021.

7. Electrospark Deposition • Welding Processes • Huys. https://huysindustries.com/welding-processes/electrospark-deposition/. Accessed July 11, 2021.

8. Tang J. Mechanical and tribological properties of the TiC–TiB2 composite coating deposited on 40Cr-steel by electro spark deposition. *Appl Surf Sci*. 2016;365:202-208.

9. LESNJAK A, TUSEK J. Processes and properties of deposits in electrospark deposition. *Sci Technol Weld Join*. 2002;7(6):391-396.

10. Peterkin S. Electro-spark deposition machine design, physical controls and parameter

effects. *Electro-spark Depos Mach Des Phys Control Param Eff*. 2016.

11. Johnson RN, Sheldon GL. Advances in the electrospark deposition coating process. *J Vac Sci Technol A, Vacuum, surfaces, Film*. 1986;4(6):2740-2746.

12. Reynolds Jr JL, Holdren RL, Brown LE. Electro-Spark Deposition. *Adv Mater Process*. 2003;161(3):35-37.

13. Johnson RN. ElectroSpark Deposition: Principles and Applications. In: *SVC - 45th Annual Technical Conference Proceedings*. Society of Vacuum Coaters; 2002:2-7.

14. Wang P, Pan G, Zhou Y, Ou JX, Shao H. Accelerated Electrospark Deposition and the Wear Behavior of Coatings. 1997:780-784.

15. Ribalko A V, Korkmaz K, Sahin O. Intensification of the anodic erosion in electrospark alloying by the employment of pulse group. 2008;202:3591-3599. doi:10.1016/j.surfcoat.2007.12.037

16. M. Fassler CH and JN. Force Sensing Technologies. *Auton Syst Lab*. 2010.

17. Welding History: Timeline and Information - Weld Guru. https://weldguru.com/welding-history/. Accessed July 11, 2021.

18. Automotive Resistance Spot Welding History. https://www.carolinacollisionequipment.com/automotive-resistance-spot-welding-history. Accessed July 11, 2021.

19. What is Spot Welding? (A Complete Welding Process Guide) - TWI. https://www.twi-global.com/technical-knowledge/faqs/what-is-spot-welding. Accessed July 12, 2021.

20. What is Spot Welding? (Definitive Guide) - Science and Engineering. https://www.science-engineering.co.uk/what-is-spot-welding-a-definitive-guide/. Accessed July 12, 2021.

21. DN Series Pneumatic-AC Spot & Projection Welding Machine_DUROWELDER GROUP. https://en.china-welding-machine.com/product/50.html. Accessed July 12, 2021.

22. Gullino A, Matteis P, Aiuto FD. Review of aluminum-to-steel welding technologies for car-body applications. *Metals (Basel)*. 2019;9(3):1-28. doi:10.3390/met9030315

23. Saleem J, Majid A, Haller S, Bertilsson K. A study of IGBT rupture phenomenon in medium frequency resistance welding machine. *Int Aegean Conf Electr Mach Power Electron ACEMP 2011 Electromotion 2011 Jt Conf*. 2011;(June 2014):236-239. doi:10.1109/ACEMP.2011.6490602

24. Hofman K, Soter M, Orsette C, Villaire S, Prokator M. A Comparison of AC to Inverter DC Resistance Spot Welding and the Effects on Dual-Phase 600. 2004:1-8.

25. Tewari A. A Review Paper on Optimization of Process Parameter of Resistance Spot Welding. *Int J Res Appl Sci Eng Technol*. 2017;V(IV):24-27. doi:10.22214/ijraset.2017.4004

26. Ramazani A, Mukherjee K, Abdurakhmanov A, Abbasi M, Prahl U. Characterization of microstructure and mechanical properties of resistance spot welded DP600 steel. *Metals (Basel)*. 2015;5(3):1704-1716. doi:10.3390/met5031704

27. What is the Heat Affected Zone (HAZ)? - TWI. https://www.twi-global.com/technical-

knowledge/faqs/what-is-the-heat-affected-zone. Accessed July 12, 2021.

28. Gawai BS, Sedani CM. Optimization of Process Parameters for Resistance Spot Welding Process of HR E-34 Using Response Surface Method. *Int J Sci Res*. 2016;5(3):2002-2008. doi:10.21275/v5i3.nov162322

29. Friction Stir Welding - TWI. https://www.twi-global.com/technical-knowledge/job-knowledge/friction-stir-welding-147. Accessed July 12, 2021.

30. Resistance spot welding - Simufact software solutions. https://www.simufact.com/resistance-spot-welding.html. Accessed July 12, 2021.

31. Ibrahim I, Ito R, Kakiuchi T, Uematsu Y, Yun K, Matsuda C. Fatigue behaviour of Al/steel dissimilar resistance spot welds fabricated using Al-Mg interlayer. *Sci Technol Weld Join*. 2016;21(3):223-233.

32. Goede M, Stehlin M, Rafflenbeul L, Kopp G, Beeh E. Super Light Car—lightweight construction thanks to a multi-material design and function integration. *Eur Transp Res Rev*. 2009;1(1):5-10.

33. Springer H, Kostka A, Payton EJ, Raabe D, Kaysser-Pyzalla A, Eggeler G. On the formation and growth of intermetallic phases during interdiffusion between low-carbon steel and aluminum alloys. *Acta Mater*. 2011;59(4):1586-1600. doi:10.1016/j.actamat.2010.11.023

34. Pouranvari M. Critical assessment: dissimilar resistance spot welding of aluminium/steel: challenges and opportunities. *Mater Sci Technol (United Kingdom)*. 2017;33(15):1705-

1712. doi:10.1080/02670836.2017.1334310

35. Simar A, Avettand-Fènoël M-N. State of the art about dissimilar metal friction stir welding. *Sci Technol Weld Join*. 2017;22(5):389-403.

36. Hussein SA, Tahir ASM, Hadzley AB. Characteristics of aluminum-to-steel joint made by friction stir welding: A review. *Mater today Commun*. 2015;5:32-49.

37. Springer H, Szczepaniak A, Raabe D. On the role of zinc on the formation and growth of intermetallic phases during interdiffusion between steel and aluminium alloys. *Acta Mater*. 2015;96:203-211.

38. Richards RW, Jones RD, Clements PD, Clarke H. Metallurgy of continuous hot dip aluminizing. *Int Mater Rev*. 1994;39(5):191-212.

39. Pouranvari M, Marashi SPH. Failure mode transition in AHSS resistance spot welds. Part I. Controlling factors. *Mater Sci Eng A Struct Mater*. 2011;528(29):8337-8343.

40. Pouranvari M, Abedi A, Marashi P, Goodarzi M. Effect of expulsion on peak load and energy absorption of low carbon steel resistance spot welds. *Sci Technol Weld Join*. 2008;13(1):39-43.

41. Qiu R, Iwamoto C, Satonaka S. Interfacial microstructure and strength of steel/aluminum alloy joints welded by resistance spot welding with cover plate. *J Mater Process Technol*. 2009;209(8):4186-4193.

42. Satonaka S, Iwamoto C, Qui R, Fujioka T. Trends and new applications of spot welding for aluminium alloy sheets. *Weld Int*. 2006;20(11):858-864.

43. Qiu R, Iwamoto C, Satonaka S. In situ scanning electron microscopy observation of fracture crack propagation in the welding interface between aluminium alloy and steel. *Mater Sci Technol*. 2009;25(10):1189-1192.

44. Qiu R, Shi H, Zhang K, Tu Y, Iwamoto C, Satonaka S. Interfacial characterization of joint between mild steel and aluminum alloy welded by resistance spot welding. *Mater Charact*. 2010;61(7):684-688.

45. Dong H, Hu W, Duan Y, Wang X, Dong C. Dissimilar metal joining of aluminum alloy to galvanized steel with Al–Si, Al–Cu, Al–Si–Cu and Zn–Al filler wires. *J Mater Process Technol*. 2012;212(2):458-464.

46. Fereiduni E, Movahedi M, Kokabi AH. Dissimilar Al/steel friction stir spot welding: To penetrate into the lower steel sheet or not? *Sci Technol Weld Join*. 2016;21(6):466-472.

47. Merkley B. The effect of zinc on cold rolling textures in cast aluminum. 2016;(April). doi:10.13140/RG.2.2.34493.26087

48. Fang Y, Jiang X, Mo D, Zhu D, Luo Z. A review on dissimilar metals' welding methods and mechanisms with interlayer. *Int J Adv Manuf Technol*. 2019;102(9-12):2845-2863.

49. Das T, Paul J. Resistance Spot Welding of Similar and Dissimilar Metals: The Effect of Graphene Interlayer. *Jom*. 2020;72(8):2863-2874. doi:10.1007/s11837-020-04159-8

50. Yongqiang D, Guangmin S, Lijing Y. Impulse Pressuring Diffusion Bonding of Titanium to Stainless Steel Using a Copper Interlayer. *Rare Met Mater Eng*. 2015;44(5):1041-1045.

51. Zhou D, Xu S, Peng L, Liu J. Laser lap welding quality of steel/aluminum dissimilar

metal joint and its electronic simulations. *Int J Adv Manuf Technol*. 2016;86(5-8):2231-2242. doi:10.1007/s00170-015-8254-0

52. Mccallum B, Mccallum B. Scholarship at UWindsor Characterization of DP600 Steel Subject to Electrohydraulic Forming By. 2014.

53. The Aluminium Association. International Alloy Designations and Chemical Composition Limits for Wrought Aluminum and Wrought Aluminum Alloys With Support for On-line Access From: Aluminum Extruders Council Use of the Information. *Alum Assoc Arlington, Virginia*. 2015;(Enero 2015):31. https://www.aluminum.org/sites/default/files/Teal Sheets.pdf.

54. *Metals Handbook*. Metals Park, Ohio: American Society for Metals; 1985.

55. Metals - Latent Heat of Fusion. https://www.engineeringtoolbox.com/fusion-heat-metals-d_1266.html. Accessed July 13, 2021.

56. Michael B. Title Page. In: *ASM Metals Reference Book*. 3rd Editio. ASM International; 1993:1-2.

57. ZEISS Ultra Plus Scanning Electron Microscope (SEM). https://www.gfz-potsdam.de/en/section/interface-geochemistry/infrastructure/potsdam-imaging-and-spectral-analysis-pisa-facility/zeiss-ultra-plus-scanning-electron-microscope-sem/. Accessed July 13, 2021.

58. Year S. Casting & Welding Engineering. (Ie 203):1-23.

59. Micro Hardness Tester, माइक्रोहार्नेस टेस्टर, माइक्रो हार्डनेस टेस्टर, माइक्रो हार्डनेस परीक्षक in

Karol Bagh, New Delhi , Sumitra Enterprises | ID: 6232530312. https://www.indiamart.com/proddetail/micro-hardness-tester-6232530312.html. Accessed July 13, 2021.

60. Hamedi M, Atashparva M. A review of electrical contact resistance modeling in resistance spot welding. *Weld World*. 2017;61(2):269-290. doi:10.1007/s40194-016-0419-4

61. Holm R. *Electric Contacts*. 4th ed. Berlin, Heidelberg, Heidelberg: Springer Berlin Heidelberg; 1967. doi:10.1007/978-3-662-06688-1

62. Arghavani MR, Movahedi M, Kokabi AH. Role of zinc layer in resistance spot welding of aluminium to steel. *Mater Des*. 2016;102:106-114. doi:10.1016/j.matdes.2016.04.033

63. Enrique PD, Li C, DiGiovanni C, Peterkin S, Zhou NY. Electrospark deposition interlayers for dissimilar resistance welding of steel to aluminum. *Manuf Lett*. 2020;24:123-126. doi:10.1016/j.mfglet.2020.04.009

64. Huin T, Dancette S, Fabrègue D, Dupuy T. Investigation of the Failure of Advanced High Strength Steels Heterogeneous Spot Welds. *Metals (Basel)*. 2016;6(5):111. doi:10.3390/met6050111

65. Wang W, Han C. Microstructure and Wear Resistance of Ti6Al4V Coating Fabricated by Electro-Spark Deposition. *Met (Basel)*. 2018;9(1):23-.

66. Azhari-Saray H, Sarkari-Khorrami M, Nademi-Babahadi A, Kashani-Bozorg SF. Dissimilar resistance spot welding of 6061-T6 aluminum alloy/St-12 carbon steel using a high entropy alloy interlayer. *Intermetallics*. 2020;124(May):106876.

doi:10.1016/j.intermet.2020.106876

Appendix. MatLab Simulation of RSW Process Using Different Interlayer Materials

```
clear all
close all
clc

Lx=0.0099;%[m]
Ly=0.025;%[m]
Lt=1/3; %[s]
%dimensions of metal sheets and weld time

Nx=100;
Ny=51;
Nt=10000;
%Number of grid points

dx=Lx/(Nx-1);
dy=Ly/(Ny-1);
dt=Lt/(Nt-1);
sf=6;
%pixels within current path on either side of the midpoint
my=round((Ny-1)/2+1);
%midpoint of simulation

Tn=zeros(Nt,Ny,Nx)+298.15;
%Initial conditions

%cross sectional area of current flow [m^2]
A=pi*0.003^2;

%Thermal Conductivity [W/(m*K)]
kc=385;
ki=163; %[https://www.efunda.com/materials/alloys/aluminum/show_aluminum.cfm?ID=AA_4043&show_prop=al
l&Page_Title=AA%204043]
ka5=138; %[http://www.matweb.com/search/DataSheet.aspx?MatGUID=b3430ccca1334449b0d59cde9f977b57]
ks=54; %[doi.org/10.13140/RG.2.1.3050.8245]

%Electrical Resistivity (ohm*m)
rhoc=0.000000017;
rhoi=4.1e-8;
rhoa5=4.99e-8;
rhos=1.9e-7;

%Heat capacity
cpa5=0.88;
cpi=0.85;

%Diffusivity calculated by k/(p*Cp)[m^2/s]
alphac=0.000112;
alphai=ki/(2.69e6*cpi);
alphaa5=ka5/(2.68e6*cpa5);
```

```
alphas=ks/(7.87e6*0.444);

%Material Hardness (Brinell)[kgF/m2]
hc=89000000;
hi=39000000;
ha5=60000000;
hs=197000000;

%Melting temperature
ma5=922;
mi=905.15;

%Heat of fusion (kJ/kg/K)
HoFa5=396;
HoFi=390;

%Factors
pf=0.2;%pressure factor
csf1=1;%contact spot factor at electrodes
csf2=1;%contact spot factor at interface

%Operating Parameters
F=305.91;%applied force, [kg force]
I=8000;%current,[A]

%Initial Condition
Tn(1,:,:)=298.15;
stability=(dt/dx^2+dt/dy^2)<1/(2*alphac) %Stability criterion
D=zeros(1,2*sf+1);
D2=zeros(1,2*sf+1,length(Nx*4.2/10+1:Nx*4.5/10-1));
D4=zeros(1,2*sf+1,length(Nx*4.5/10+1:Nx*6.6/10-1));

for n=1:Nt

    %%Interior Bulk
    %Top electrode nodes
    gc=I^2*rhoc/(A)^2/kc;
    x1=round(Nx*6.6/10+2:Nx);    x2=round(Nx*6.6/10+1:Nx-1);    x3=round(Nx*6.6/10:Nx-2);
    y1=round(my-sf:my+sf-2);    y2=round(my-sf+1:my+sf-1);    y3=round(my-sf+2:my+sf);
    Dx=(Tn(n,y2,x1)-2*Tn(n,y2,x2)+Tn(n,y2,x3))/dx^2;
    Dy=(Tn(n,y1,x2)-2*Tn(n,y2,x2)+Tn(n,y3,x2))/dy^2;
    Tn(n+1,y2,x2)=Tn(n,y2,x2)+dt*alphac*(Dx+Dy+gc);

    %Bottom electrode nodes
    x1=round(1:Nx*3/10-2);    x2=round(2:Nx*3/10-1);    x3=round(3:Nx*3/10);
    y1=round(my-sf:my+sf-2);    y2=round(my-sf+1:my+sf-1);    y3=round(my-sf+2:my+sf);
    Dx=(Tn(n,y2,x1)-2*Tn(n,y2,x2)+Tn(n,y2,x3))/dx^2;
    Dy=(Tn(n,y1,x2)-2*Tn(n,y2,x2)+Tn(n,y3,x2))/dy^2;
    Tn(n+1,y2,x2)=Tn(n,y2,x2)+dt*alphac*(Dx+Dy+gc);

    %Steel within current path
    gs=I^2*rhos/(A)^2/ks;
    x1=round(Nx*3/10+2:Nx*4.2/10);    x2=round(Nx*3/10+1:Nx*4.2/10-1);    x3=round(Nx*3/10:Nx*4.2/10-2);
    y1=round(my-sf-1:my+sf-1);    y2=round(my-sf:my+sf);    y3=round(my-sf+1:my+sf+1);
    Dx=(Tn(n,y2,x1)-2*Tn(n,y2,x2)+Tn(n,y2,x3))/dx^2;
    Dy=(Tn(n,y1,x2)-2*Tn(n,y2,x2)+Tn(n,y3,x2))/dy^2;
```

```
    Tn(n+1,y2,x2)=Tn(n,y2,x2)+dt*alphas*(Dx+Dy+gs);

    %Steel left of current path
    y1=round(1:my-sf-2);    y2=round(2:my-sf-1);    y3=round(3:my-sf);
    Dx=(Tn(n,y2,x1)-2*Tn(n,y2,x2)+Tn(n,y2,x3))/dx^2;
    Dy=(Tn(n,y1,x2)-2*Tn(n,y2,x2)+Tn(n,y3,x2))/dy^2;
    Tn(n+1,y2,x2)=Tn(n,y2,x2)+dt*alphas*(Dx+Dy);

    %Steel right of current path
    y1=round(my+sf:Ny-2);    y2=round(my+sf+1:Ny-1);    y3=round(my+sf+2:Ny);
    Dx=(Tn(n,y2,x1)-2*Tn(n,y2,x2)+Tn(n,y2,x3))/dx^2;
    Dy=(Tn(n,y1,x2)-2*Tn(n,y2,x2)+Tn(n,y3,x2))/dy^2;
    Tn(n+1,y2,x2)=Tn(n,y2,x2)+dt*alphas*(Dx+Dy);

    %Interlayer in current path
    gi=I^2*rhoi/(A)^2/ki;
    x1=round(Nx*4.2/10+2:Nx*4.5/10);    x2=round(Nx*4.2/10+1:Nx*4.5/10-1);    x3=round(Nx*4.2/10:Nx*4.5/10-
2);
    y1=round(my-sf-1:my+sf-1);    y2=round(my-sf:my+sf);    y3=round(my-sf+1:my+sf+1);
    Dx=(Tn(n,y2,x1)-2*Tn(n,y2,x2)+Tn(n,y2,x3))/dx^2;
    Dy=(Tn(n,y1,x2)-2*Tn(n,y2,x2)+Tn(n,y3,x2))/dy^2;
    Tn(n+1,y2,x2)=Tn(n,y2,x2)+dt*alphai*(Dx+Dy+gi);

    A2=Tn(n+1,my-sf:my+sf,x2); %New temperatures
    B2=A2>mi; %Elements in A over 900K
    C2=B2.*(A2-mi); %Amount over 900K
    D2=D2+C2; %Add amount over to previous amounts over
    E2=D2<HoFi/cpi; %Elements which have not transitioned from solid to liquid
    Tn(n+1,y2,x2)=Tn(n+1,y2,x2)-(A2-mi).*E2.*B2; %Adjust temperature to consider latent heat of fusion

    %Interlayer left of current path
    y1=round(1:my-sf-2);    y2=round(2:my-sf-1);    y3=round(3:my-sf);
    Dx=(Tn(n,y2,x1)-2*Tn(n,y2,x2)+Tn(n,y2,x3))/dx^2;
    Dy=(Tn(n,y1,x2)-2*Tn(n,y2,x2)+Tn(n,y3,x2))/dy^2;
    Tn(n+1,y2,x2)=Tn(n,y2,x2)+dt*alphai*(Dx+Dy);

    %Interlayer right of current path
    y1=round(my+sf:Ny-2);    y2=round(my+sf+1:Ny-1);    y3=round(my+sf+2:Ny);
    Dx=(Tn(n,y2,x1)-2*Tn(n,y2,x2)+Tn(n,y2,x3))/dx^2;
    Dy=(Tn(n,y1,x2)-2*Tn(n,y2,x2)+Tn(n,y3,x2))/dy^2;
    Tn(n+1,y2,x2)=Tn(n,y2,x2)+dt*alphai*(Dx+Dy);

    %AA5052 in current path
    ga5=I^2*rhoa5/(A)^2/ka5;
    x1=round(Nx*4.5/10+2:Nx*6.6/10);    x2=round(Nx*4.5/10+1:Nx*6.6/10-1);    x3=round(Nx*4.5/10:Nx*6.6/10-
2);
    y1=round(my-sf-1:my+sf-1);    y2=round(my-sf:my+sf);    y3=round(my-sf+1:my+sf+1);
    Dx=(Tn(n,y2,x1)-2*Tn(n,y2,x2)+Tn(n,y2,x3))/dx^2;
    Dy=(Tn(n,y1,x2)-2*Tn(n,y2,x2)+Tn(n,y3,x2))/dy^2;
    Tn(n+1,y2,x2)=Tn(n,y2,x2)+dt*alphaa5*(Dx+Dy+ga5);

    A4=Tn(n+1,my-sf:my+sf,x2); %New temperatures
    B4=A4>ma5; %Elements in A over 900K
    C4=B4.*(A4-ma5); %Amount over 900K
    D4=D4+C4; %Add amount over to previous amounts over
    E4=D4<HoFa5/cpa5; %Elements which have not transitioned from solid to liquid
```

```
    Tn(n+1,y2,x2)=Tn(n+1,y2,x2)-(A4-ma5).*E4.*B4; %Adjust temperature to consider latent heat of fusion

    %AA5052 left of current path
    y1=round(1:my-sf-2);    y2=round(2:my-sf-1);    y3=round(3:my-sf);
    Dx=(Tn(n,y2,x1)-2*Tn(n,y2,x2)+Tn(n,y2,x3))/dx^2;
    Dy=(Tn(n,y1,x2)-2*Tn(n,y2,x2)+Tn(n,y3,x2))/dy^2;
    Tn(n+1,y2,x2)=Tn(n,y2,x2)+dt*alphaa5*(Dx+Dy);

    %AA5052 right of current path
    y1=round(my+sf:Ny-2);    y2=round(my+sf+1:Ny-1);    y3=round(my+sf+2:Ny);
    Dx=(Tn(n,y2,x1)-2*Tn(n,y2,x2)+Tn(n,y2,x3))/dx^2;
    Dy=(Tn(n,y1,x2)-2*Tn(n,y2,x2)+Tn(n,y3,x2))/dy^2;
    Tn(n+1,y2,x2)=Tn(n,y2,x2)+dt*alphaa5*(Dx+Dy);

    %%Edges
    %Top electrode top edge
    Tn(n+1,my-sf:my+sf,Nx)=ones(1,length(my-sf:my+sf))*283.15;

    %Bottom electrode bottom edge
    Tn(n+1,my-sf:my+sf,1)=ones(1,length(my-sf:my+sf))*283.15;

    %Top electrode left edge
    Dx=(Tn(n,my-sf,Nx*6.6/10:Nx-2)+Tn(n,my-sf,Nx*6.6/10+2:Nx)-2*Tn(n,my-sf,Nx*6.6/10+1:Nx-1))/dx^2;
    Dy=(2*Tn(n,my-sf+1,Nx*6.6/10+1:Nx-1)-2*Tn(n,my-sf,Nx*6.6/10+1:Nx-1))/dy^2;
    Tn(n+1,my-sf,Nx*6.6/10+1:Nx-1) = Tn(n,my-sf,Nx*6.6/10+1:Nx-1)+alphac*dt*(Dy+Dx+gc);

    %Top electrode right edge
    Dx=(Tn(n,my+sf,Nx*6.6/10:Nx-2)+Tn(n,my+sf,Nx*6.6/10+2:Nx)-2*Tn(n,my+sf,Nx*6.6/10+1:Nx-1))/dx^2;
    Dy=(2*Tn(n,my+sf-1,Nx*6.6/10+1:Nx-1)-2*Tn(n,my+sf,Nx*6.6/10+1:Nx-1))/dy^2;
    Tn(n+1,my+sf,Nx*6.6/10+1:Nx-1) = Tn(n,my+sf,Nx*6.6/10+1:Nx-1)+alphac*dt*(Dy+Dx+gc);

    %Bottom electrode left edge
    Dx=(Tn(n,my-sf,1:Nx*3/10-2)+Tn(n,my-sf,3:Nx*3/10)-2*Tn(n,my-sf,2:Nx*3/10-1))/dx^2;
    Dy=(2*Tn(n,my-sf+1,2:Nx*3/10-1)-2*Tn(n,my-sf,2:Nx*3/10-1))/dy^2;
    Tn(n+1,my-sf,2:Nx*3/10-1) = Tn(n,my-sf,2:Nx*3/10-1)+alphac*dt*(Dy+Dx+gc);

    %Bottom electrode right edge
    Dx=(Tn(n,my+sf,1:Nx*3/10-2)+Tn(n,my+sf,3:Nx*3/10)-2*Tn(n,my+sf,2:Nx*3/10-1))/dx^2;
    Dy=(2*Tn(n,my+sf-1,2:Nx*3/10-1)-2*Tn(n,my+sf,2:Nx*3/10-1))/dy^2;
    Tn(n+1,my+sf,2:Nx*3/10-1) = Tn(n,my+sf,2:Nx*3/10-1)+alphac*dt*(Dy+Dx+gc);

    %AA5052 top left edge
    Dx=(2*Tn(n,2:my-sf-1,Nx*6.6/10-1)-2*Tn(n,2:my-sf-1,Nx*6.6/10))/dx^2;
    Dy=(Tn(n,1:my-sf-2,Nx*6.6/10)+Tn(n,3:my-sf,Nx*6.6/10)-2*Tn(n,2:my-sf-1,Nx*6.6/10))/dy^2;
    Tn(n+1,2:my-sf-1,Nx*6.6/10) = Tn(n,2:my-sf-1,Nx*6.6/10)+alphaa5*dt*(Dy+Dx);

    %AA5052 top right edge
    Dx=(2*Tn(n,my+sf+1:Ny-1,Nx*6.6/10-1)-2*Tn(n,my+sf+1:Ny-1,Nx*6.6/10))/dx^2;
    Dy=(Tn(n,my+sf:Ny-2,Nx*6.6/10)+Tn(n,my+sf+2:Ny,Nx*6.6/10)-2*Tn(n,my+sf+1:Ny-1,Nx*6.6/10))/dy^2;
    Tn(n+1,my+sf+1:Ny-1,Nx*6.6/10) = Tn(n,my+sf+1:Ny-1,Nx*6.6/10)+alphaa5*dt*(Dy+Dx);

    %AA5052 side left edge
    x1=round(Nx*4.5/10:Nx*6.6/10-2);    x2=round(Nx*4.5/10+1:Nx*6.6/10-1);
x3=round(Nx*4.5/10+2:Nx*6.6/10);
    Dx=(Tn(n,1,x3)+Tn(n,1,x1)-2*Tn(n,1,x2))/dx^2;
    Dy=(2*Tn(n,2,x2)-2*Tn(n,1,x2))/dy^2;
```

```
    Tn(n+1,1,x2) = Tn(n,1,x2)+alphaa5*dt*(Dy+Dx);

    %AA5052 side right edge
    Dx=(Tn(n,Ny,x3)+Tn(n,Ny,x1)-2*Tn(n,Ny,x2))/dx^2;
    Dy=(2*Tn(n,Ny-1,x2)-2*Tn(n,Ny,x2))/dy^2;
    Tn(n+1,Ny,x2) = Tn(n,Ny,x2)+alphaa5*dt*(Dy+Dx);

    %Interlayer side left edge
    x1=round(Nx*4.2/10:Nx*4.5/10-2);    x2=round(Nx*4.2/10+1:Nx*4.5/10-1);
x3=round(Nx*4.2/10+2:Nx*4.5/10);
    Dx=(Tn(n,1,x3)+Tn(n,1,x1)-2*Tn(n,1,x2))/dx^2;
    Dy=(2*Tn(n,2,x2)-2*Tn(n,1,x2))/dy^2;
    Tn(n+1,1,x2) = Tn(n,1,x2)+alphai*dt*(Dy+Dx);

    %Interlayer side right edge
    Dx=(Tn(n,Ny,x3)+Tn(n,Ny,x1)-2*Tn(n,Ny,x2))/dx^2;
    Dy=(2*Tn(n,Ny-1,x2)-2*Tn(n,Ny,x2))/dy^2;
    Tn(n+1,Ny,x2) = Tn(n,Ny,x2)+alphai*dt*(Dy+Dx);

    %Steel side left edge
    Dx=(Tn(n,1,Nx*3/10+2:Nx*4.2/10)+Tn(n,1,Nx*3/10:Nx*4.2/10-2)-2*Tn(n,1,Nx*3/10+1:Nx*4.2/10-1))/dx^2;
    Dy=(2*Tn(n,2,Nx*3/10+1:Nx*4.2/10-1)-2*Tn(n,1,Nx*3/10+1:Nx*4.2/10-1))/dy^2;
    Tn(n+1,1,Nx*3/10+1:Nx*4.2/10-1) = Tn(n,1,Nx*3/10+1:Nx*4.2/10-1)+alphas*dt*(Dy+Dx);

    %Steel side right edge
    Dx=(Tn(n,Ny,Nx*3/10+2:Nx*4.2/10)+Tn(n,Ny,Nx*3/10:Nx*4.2/10-2)-2*Tn(n,Ny,Nx*3/10+1:Nx*4.2/10-
1))/dx^2;
    Dy=(2*Tn(n,Ny-1,Nx*3/10+1:Nx*4.2/10-1)-2*Tn(n,Ny,Nx*3/10+1:Nx*4.2/10-1))/dy^2;
    Tn(n+1,Ny,Nx*3/10+1:Nx*4.2/10-1) = Tn(n,Ny,Nx*3/10+1:Nx*4.2/10-1)+alphas*dt*(Dy+Dx);

    %Steel bottom left edge
    Dx=(2*Tn(n,2:my-sf-1,Nx*3/10+1)-2*Tn(n,2:my-sf-1,Nx*3/10))/dx^2;
    Dy=(Tn(n,1:my-sf-2,Nx*3/10)+Tn(n,3:my-sf,Nx*3/10)-2*Tn(n,2:my-sf-1,Nx*3/10))/dy^2;
    Tn(n+1,2:my-sf-1,Nx*3/10) = Tn(n,2:my-sf-1,Nx*3/10)+alphas*dt*(Dy+Dx);

    %Steel bottom right edge
    Dx=(2*Tn(n,my+sf+1:Ny-1,Nx*3/10+1)-2*Tn(n,my+sf+1:Ny-1,Nx*3/10))/dx^2;
    Dy=(Tn(n,my+sf:Ny-2,Nx*3/10)+Tn(n,my+sf+2:Ny,Nx*3/10)-2*Tn(n,my+sf+1:Ny-1,Nx*3/10))/dy^2;
    Tn(n+1,my+sf+1:Ny-1,Nx*3/10) = Tn(n,my+sf+1:Ny-1,Nx*3/10)+alphas*dt*(Dy+Dx);

    %%Corners
    %AA5052 top left corner
    Dx=(2*Tn(n,1,Nx*6.6/10-1)-2*Tn(n,1,Nx*6.6/10))/dx^2;
    Dy=(2*Tn(n,2,Nx*6.6/10)-2*Tn(n,1,Nx*6.6/10))/dy^2;
    Tn(n+1,1,Nx*6.6/10) = Tn(n,1,Nx*6.6/10)+alphaa5*dt*(Dy+Dx);

    %AA5052 top right corner
    Dx=(2*Tn(n,Ny,Nx*6.6/10-1)-2*Tn(n,Ny,Nx*6.6/10))/dx^2;
    Dy=(2*Tn(n,Ny-1,Nx*6.6/10)-2*Tn(n,Ny,Nx*6.6/10))/dy^2;
    Tn(n+1,Ny,Nx*6.6/10) = Tn(n,Ny,Nx*6.6/10)+alphaa5*dt*(Dy+Dx);

    %Interlayer/AA5052 shared left corner
    x1=round(Nx*4.5/10-1);    x2=round(Nx*4.5/10);    x3=round(Nx*4.5/10+1);
    Dx=(Tn(n,1,x1)+Tn(n,1,x3)-2*Tn(n,1,x2))/dx^2;
    Dy=(2*Tn(n,2,x2)-2*Tn(n,1,x2))/dy^2;
    Tn(n+1,1,x2) = Tn(n,1,x2)+(alphaa5+alphai)/2*dt*(Dy+Dx);
```

```
    %Interlayer/AA5052 shared right corner
    x1=round(Nx*4.5/10-1);    x2=round(Nx*4.5/10);    x3=round(Nx*4.5/10+1);
    Dx=(Tn(n,Ny,x1)+Tn(n,Ny,x3)-2*Tn(n,Ny,x2))/dx^2;
    Dy=(2*Tn(n,Ny-1,x2)-2*Tn(n,Ny,x2))/dy^2;
    Tn(n+1,Ny,x2) = Tn(n,Ny,x2)+(alphaa5+alphai)/2*dt*(Dy+Dx);

    %Steel/interlayer shared left corner
    x1=round(Nx*4.2/10-1);    x2=round(Nx*4.2/10);    x3=round(Nx*4.2/10+1);
    Dx=(Tn(n,1,x1)+Tn(n,1,x3)-2*Tn(n,1,x2))/dx^2;
    Dy=(2*Tn(n,2,x2)-2*Tn(n,1,x2))/dy^2;
    Tn(n+1,1,x2) = Tn(n,1,x2)+(alphai+alphas)/2*dt*(Dy+Dx);

    %Steel/interlayer shared right corner
    Dx=(Tn(n,Ny,Nx*4.2/10-1)+Tn(n,Ny,Nx*4.2/10+1)-2*Tn(n,Ny,Nx*4.2/10))/dx^2;
    Dy=(2*Tn(n,Ny-1,Nx*4.2/10)-2*Tn(n,Ny,Nx*4.2/10))/dy^2;
    Tn(n+1,Ny,Nx*4.2/10) = Tn(n,Ny,Nx*4.2/10)+(alphai+alphas)/2*dt*(Dy+Dx);

    %Steel bottom left corner
    Dx=(2*Tn(n,1,Nx*3/10+1)-2*Tn(n,1,Nx*3/10))/dx^2;
    Dy=(2*Tn(n,2,Nx*3/10)-2*Tn(n,1,Nx*3/10))/dy^2;
    Tn(n+1,1,Nx*3/10) = Tn(n,1,Nx*3/10)+alphas*dt*(Dy+Dx);

    %Steel bottom right corner
    Dx=(2*Tn(n,Ny,Nx*3/10+1)-2*Tn(n,Ny,Nx*3/10))/dx^2;
    Dy=(2*Tn(n,Ny-1,Nx*3/10)-2*Tn(n,Ny,Nx*3/10))/dy^2;
    Tn(n+1,Ny,Nx*3/10) = Tn(n,Ny,Nx*3/10)+alphas*dt*(Dy+Dx);

    %%Interfaces
    %AA5052/copper interface in the current path
    ga5c=I^2*((rhoc+rhoa5)/2)/(A)^2/((kc+ka5)/2); %+
(I^2*0.89*(rhoc+rhoa5)/2*sqrt(pf*(hc+ha5)/2/csf1/F)/(A*dx))/((kc+ka5)/2); %Bulk + Constriction resistance
    Dx=(Tn(n,my-sf:my+sf,Nx*6.6/10-1)-2*Tn(n,my-sf:my+sf,Nx*6.6/10)+Tn(n,my-sf:my+sf,Nx*6.6/10+1))/dx^2;
    Dy=(Tn(n,my-sf-1:my+sf-1,Nx*6.6/10)-2*Tn(n,my-sf:my+sf,Nx*6.6/10)+Tn(n,my-
sf+1:my+sf+1,Nx*6.6/10))/dy^2;
    Tn(n+1,my-sf:my+sf,Nx*6.6/10)=Tn(n,my-sf:my+sf,Nx*6.6/10)+dt*(alphaa5+alphac)/2*(Dx+Dy+ga5c);

    %Interlayer/AA5052 interface in the current path
    gia5=I^2*((rhoa5+rhoi)/2)/(A)^2/((ka5+ki)/2) +
(I^2*0.89*(rhoi+rhoa5)/2*sqrt(pf*(hi+ha5)/2/csf2/F)/(A*dx))/((ki+ka5)/2); %Bulk + Constriction resistance
    x1=round(Nx*4.5/10-1);    x2=round(Nx*4.5/10);    x3=round(Nx*4.5/10+1);
    Dx=(Tn(n,my-sf:my+sf,x1)-2*Tn(n,my-sf:my+sf,x2)+Tn(n,my-sf:my+sf,x3))/dx^2;
    Dy=(Tn(n,my-sf-1:my+sf-1,x2)-2*Tn(n,my-sf:my+sf,x2)+Tn(n,my-sf+1:my+sf+1,x2))/dy^2;
    Tn(n+1,my-sf:my+sf,x2)=Tn(n,my-sf:my+sf,x2)+dt*(alphaa5+alphai)/2*(Dx+Dy+gia5);

    A3=Tn(n+1,my-sf:my+sf,x2); %New temperatures
    B=A3>mi; %Elements in A over 900K
    C=B.*(A3-mi); %Amount over 900K
    D=D+C; %Add amount over to previous amounts over
    E=D<HoFi/cpi; %Elements which have not transitioned from solid to liquid
    Tn(n+1,my-sf:my+sf,x2)=Tn(n+1,my-sf:my+sf,x2)-(A3-mi).*E.*B;

    %Interlayer/AA5052 interface left of the current path
    Dx=(Tn(n,2:my-sf-1,x1)-2*Tn(n,2:my-sf-1,x2)+Tn(n,2:my-sf-1,x3))/dx^2;
    Dy=(Tn(n,1:my-sf-2,x2)-2*Tn(n,2:my-sf-1,x2)+Tn(n,3:my-sf,x2))/dy^2;
    Tn(n+1,2:my-sf-1,x2)=Tn(n,2:my-sf-1,x2)+dt*(alphaa5+alphai)/2*(Dx+Dy);
```

```
    %Interlayer/AA5052 interface right of the current path
    Dx=(Tn(n,my+sf+1:Ny-1,x1)-2*Tn(n,my+sf+1:Ny-1,x2)+Tn(n,my+sf+1:Ny-1,x3))/dx^2;
    Dy=(Tn(n,my+sf:Ny-2,x2)-2*Tn(n,my+sf+1:Ny-1,x2)+Tn(n,my+sf+2:Ny,x2))/dy^2;
    Tn(n+1,my+sf+1:Ny-1,x2)=Tn(n,my+sf+1:Ny-1,x2)+dt*(alphaa5+alphai)/2*(Dx+Dy);

    %Steel/interlayer interface in the current path
    gsi=I^2*((rhos+rhoi)/2)/(A)^2/((ks+ki)/2);
    Dx=(Tn(n,my-sf:my+sf,Nx*4.2/10-1)-2*Tn(n,my-sf:my+sf,Nx*4.2/10)+Tn(n,my-sf:my+sf,Nx*4.2/10+1))/dx^2;
    Dy=(Tn(n,my-sf-1:my+sf-1,Nx*4.2/10)-2*Tn(n,my-sf:my+sf,Nx*4.2/10)+Tn(n,my-sf+1:my+sf+1,Nx*4.2/10))/dy^2;
    Tn(n+1,my-sf:my+sf,Nx*4.2/10)=Tn(n,my-sf:my+sf,Nx*4.2/10)+dt*(alphas+alphai)/2*(Dx+Dy+gsi);

    %Steel/interlayer interface left of the current path
    Dx=(Tn(n,2:my-sf-1,Nx*4.2/10-1)-2*Tn(n,2:my-sf-1,Nx*4.2/10)+Tn(n,2:my-sf-1,Nx*4.2/10+1))/dx^2;
    Dy=(Tn(n,1:my-sf-2,Nx*4.2/10)-2*Tn(n,2:my-sf-1,Nx*4.2/10)+Tn(n,3:my-sf,Nx*4.2/10))/dy^2;
    Tn(n+1,2:my-sf-1,Nx*4.2/10)=Tn(n,2:my-sf-1,Nx*4.2/10)+dt*(alphas+alphai)/2*(Dx+Dy);

    %Steel/interlayer interface right of the current path
    Dx=(Tn(n,my+sf+1:Ny-1,Nx*4.2/10-1)-2*Tn(n,my+sf+1:Ny-1,Nx*4.2/10)+Tn(n,my+sf+1:Ny-1,Nx*4.2/10+1))/dx^2;
    Dy=(Tn(n,my+sf:Ny-2,Nx*4.2/10)-2*Tn(n,my+sf+1:Ny-1,Nx*4.2/10)+Tn(n,my+sf+2:Ny,Nx*4.2/10))/dy^2;
    Tn(n+1,my+sf+1:Ny-1,Nx*4.2/10)=Tn(n,my+sf+1:Ny-1,Nx*4.2/10)+dt*(alphas+alphai)/2*(Dx+Dy);

    %Copper/steel interface in the current path
    gsc=I^2*((rhos+rhoc)/2)/(A)^2/((ks+kc)/2); %+(I^2*0.89*(rhos+rhoc)/2*sqrt(pf*(hs+hc)/2/csf1/F)/(A*dx))/((ks+kc)/2); %Bulk + Constriction resistance
    Dx=(Tn(n,my-sf:my+sf,Nx*3/10-1)-2*Tn(n,my-sf:my+sf,Nx*3/10)+Tn(n,my-sf:my+sf,Nx*3/10+1))/dx^2;
    Dy=(Tn(n,my-sf-1:my+sf-1,Nx*3/10)-2*Tn(n,my-sf:my+sf,Nx*3/10)+Tn(n,my-sf+1:my+sf+1,Nx*3/10))/dy^2;
    Tn(n+1,my-sf:my+sf,Nx*3/10)=Tn(n,my-sf:my+sf,Nx*3/10)+dt*(alphas+alphac)/2*(Dx+Dy+gsc);


end

output=squeeze(Tn(n,:,:))';
csvwrite('Tn_AA4043_8kA_1.csv',output)
```